Matthias Fischer

The Fast Multipole Boundary Element Method and its Application to Structure-Acoustic Field Interaction

Bericht aus dem Institut A für Mechanik 2004/2

The Fast Multipole Boundary Element Method and its Application to Structure-Acoustic Field Interaction

Von der Fakultät Maschinenbau der Universität Stuttgart
zur Erlangung der Würde eines Doktor-Ingenieurs (Dr.-Ing.)
genehmigte Abhandlung

vorgelegt von
Matthias Fischer
aus Stuttgart

Hauptberichter:	Prof. Dr.-Ing. L. Gaul
Mitberichter:	Prof. Dr. B. Wohlmuth
Tag der mündlichen Prüfung:	13. August 2004

Institut A für Mechanik der Universität Stuttgart
2004

D 93

Herausgeber

Universität Stuttgart
Institut A für Mechanik

Prof. Dr.-Ing. habil. L. Gaul
Prof. Dr.-Ing. A. Kistner

ISSN 0946-7157

Acknowledgments

The results presented in this thesis are the outcome of my work at the Institut A für Mechanik at the Universität Stuttgart within the collaborative research center SFB 404 "Multifield Problems in Continuum Mechanics." I am very grateful to the Deutsche Forschungsgemeinschaft for the financial support of the project.

I would like to thank Prof. Dr.-Ing. habil. Lothar Gaul for his mentoring, support and encouragement of my research work. Special thanks I owe to Prof. Dr. Barbara Wohlmuth and Prof. Dr. Olaf Steinbach for their continued mathematical assistance within the collaborative research center. Moreover, it was a great enrichment to win Prof. Wohlmuth for the thesis committee.

During my work at Institut A für Mechanik I greatly enjoyed the inspiring and cooperative atmosphere. In this context, it is my pleasure to thank Prof. Dr.-Ing. Arnold Kistner, Dr.-Ing. Michael Hanss and all the other colleagues for their commitment. I record my distinct appreciation to Dipl.-Ing. Matthias Maess for the profound and stimulating discussions on the physics and numerics of acoustic-structure interaction. Last but not least, I would like to thank Dr.-Ing. Nils Wagner for carefully reviewing this thesis.

Stuttgart, August 2004 Matthias Fischer

Contents

List of symbols and abbreviations

No special notation for vectors is employed throughout the thesis. Column matrices are denoted in bold lower case letters, general matrices in bold capitals.

For a systematic listing, the used symbols and abbreviation are presented according to their field of major application.

Boundary element method

Ω	bounded domain
Ω^{e}	exterior domain
$\Gamma = \partial\Omega$	boundary to Ω
n	unit normal vector, pointing outwards from Ω
x	field point
y	load point
$r = \lvert x - y \rvert$	Euclidean distance between field and load point
$p(x)$	acoustic pressure
$q(x) = \partial p(x)/\partial n_x$	acoustic flux on boundary
$\bar{p}(x), \bar{q}(x)$	prescribed boundary conditions
$P^*(x, y)$	fundamental solution for acoustic pressure
V	single layer potential
K	double layer potential
K'	adjoint double layer potential
I	identity operator
D	hyper-singular operator
$\mathcal{C}$	Calderon projector
p_h	boundary element approximation of acoustic pressure
$\mathbf{p}$	column matrix of nodal pressure values
q_h	boundary element approximation of acoustic flux
$\mathbf{q}$	column matrix of element flux values
$\boldsymbol{\varphi}^p, \boldsymbol{\varphi}^q$	shape functions

Multipole algorithm

D	distance vector between expansion centers
d	distance vector between source/field point and expansion center
s	direction unit vector
$F(s)$	far-field signature
$N(s)$	near-field signature
$M_L(s, D)$	diagonal translation operator with expansion length L

Iterative solvers

$\mathbf{x}_k$	solution at iteration step k
$\mathbf{r}_k$	residual at iteration step k
$\mathbf{A}$	system matrix
$\mathbf{M^{-1}}$	preconditioning matrix
$\mathcal{S}$	smoothing operator
$\mathbf{R}_{(l)}^{(l-1)}$	restriction matrix from grid l to $l-1$
$\mathbf{P}_{(l-1)}^{(l)}$	prolongation matrix from grid $l-1$ to l

Structure-acoustic field interaction

$(\cdot)^s$	item for structure
$(\cdot)^f$	item for acoustic fluid
Γ^{int}	coupling interface
w	out-of-plane plate displacement
f	normal load on plate
λ	Lagrange multiplier

Abstract

The goal of the thesis is to provide an efficient simulation tool for the prediction of sound radiation from vibrating structures. Acoustic simulations are an important step to optimize the properties of a new product early in the design phase rather than curing mistakes afterwards. The boundary element method (BEM) is widely used in acoustics, since it allows the simulation of fields in unbounded domains. Only the surface of the sound radiating structure must be discretized with a very low cost for mesh generation and preprocessing. The limiting factor for the application of the BEM to large-scale simulations is its fully populated system matrix. It implies that computing time and memory requirements increase quadratically with the number of elements which cannot be handled even for moderately sized problems.

The fast multipole BEM allows the computation of the BEM matrix-vector products at a quasi-linear numerical cost. The reduction is achieved by multilevel clustering of the boundary elements and the use of the multipole series expansion for the evaluation of the fundamental solution. In combination with an efficient iterative solver, multipole BEM simulations can be performed on large models consisting of more than 100,000 boundary elements. The generalized minimal residual method (GMRES) and multigrid solvers are most suitable for the solution of the BEM systems of equations. An approximate inverse preconditioner is developed for both approaches that restricts the number of required iterations and thus allows efficient multipole BEM simulations on fine discretizations and high frequencies.

For the simulation of structure-acoustic field interaction problems, the coupled field equations must be solved. The structure is commonly discretized using finite elements, whereas for the acoustic field the BEM is favorable. A mortar FEM-BEM coupling algorithm is developed that allows the combination of non-conforming meshes. The high flexibility for the choice of discretizations offers a high efficiency, since specialized shape functions and adaptive mesh refinement can be used in the subdomains. The mortar coupling algorithm yields a saddle point problem that is solved using an inexact Uzawa algorithm. The iterative solver enables the use of the multipole BEM and thus coupled simulations on large boundary element models.

Kurzfassung

Die akustischen Eigenschaften von Produkten spielen heute eine wichtige Rolle für ihre Qualitätsanmutung. Die Entscheidung für den Kauf eines Staubsaugers wird wesentlich auf Grund der auditiven Wahrnehmung getroffen und auch bei der Beschaffung eines Großraumflugzeugs stellt das Geräuschniveau ein wichtiges Kriterium dar. Durch den Einsatz von Akustik-Simulationen lassen sich viele Lärm-Probleme schon früh im Entwicklungsprozess erkennen und die Klangeigenschaften gezielt beeinflussen. Teure Modifikationen an Prototypen können dadurch auf ein Minimum reduziert werden. Herkömmliche Simulationsverfahren erfordern jedoch einen sehr hohen Rechenaufwand und können nur für stark vereinfachte Modelle verwendet werden. Ziel dieser Arbeit ist die Entwicklung eines effizienten Simulationswerkzeugs, dass die Vorhersage der Schallabstrahlung von komplexen schwingenden Strukturen ermöglicht.

Die Randelementmethode (BEM) ist ein Diskretisierungsverfahren für die näherungsweise Lösung von Randintegralgleichungen. Für die Akustik werden diese über die schwache Form der Helmholtz-Gleichung mit der Fundamentallösung als Wichtungsfunktion hergeleitet. Die Randelementmethode ist besonders geeignet für die Simulation von Akustik-Feldern, da nur die Oberfläche der schallabstrahlenden Struktur diskretisiert werden muss und Außenraumprobleme keinen zusätzlichen Aufwand erfordern. Die Anwendung der Randelementmethode wird jedoch durch die vollbesetzten Systemmatrizen erschwert: die Rechenzeit und der Speicherbedarf steigen quadratisch mit der Anzahl der Randelemente an. Dieser numerische Aufwand kann für komplexe industrielle Anwendungen nicht beherrscht werden. In praktischen Berechnungen wird die Elementgröße der Randelementdiskretisierung nach der Faustregel „sechs bis zehn lineare Elemente pro Wellenlänge“ bestimmt, die einen näherungsweise gleichbleibenden Diskretisierungsfehler gewährleistet. Verfeinert man das Randelementnetz, wie von der Faustregel vorgegeben, werden für eine Simulation bei doppelter Frequenz viermal so viele Randelemente benötigt. Durch den quadratischen Aufwand der Randelementmethode ergeben sich also eine 16 mal höhere Rechenzeit und ein 16 mal höherer Speicherbedarf. Dieses Beispiel zeigt deutlich, dass die herkömmliche Randelementmethode nur für kleine Modelle im niederen Frequenzbereich eingesetzt werden kann.

Der Multipol-Algorithmus ermöglicht die Auswertung der BEM-Matrix-Vektor-Produkte mit einem numerischen Aufwand, der quasi-linear mit der Anzahl der Frei-

heitsgrade ansteigt. Für große Randelementmodelle ergibt sich so eine starke Reduktion der Rechenzeit und des Speicherbedarfs. Die Randintegraloperatoren werden für den Multipol-Algorithmus in einen Nahfeld- und einen Fernfeldanteil aufgespalten. Der Nahfeldanteil wird durch eine herkömmliche Auswertung der Fundamentallösung bestimmt. Für den Fernfeldanteil werden die Randelemente in Cluster eingeteilt und in einer Baumstruktur organisiert. Über die Cluster wird die Interaktion der Randelemente im Fernfeld durch eine Multipol-Darstellung der Fundamentallösung berücksichtigt. Die Verwendung von Fern- und Nahfeldrepräsentanten sowie diagonaler Transferoperatoren stellt sich dabei als besonders vorteilhaft heraus.

Auf jeder Ebene des Clusterbaums wird der Nahbereich (N) definiert, für den der Abstand der Cluster unterhalb einer wählbaren Grenze liegt. Cluster, die nicht im Nahbereich selbst, aber im Nahbereich des übergeordneten Clusters liegen, bilden die Interaktionsliste (I). Diese Einteilung ist in Abbildung 1 für eine zweidimensionale Schematisierung des Clusterbaums dargestellt. Den Beitrag eines Randelements im schraffierten Cluster auf der untersten Ebene wird durch die folgenden Schritte des Multipol-Algorithmus berücksichtigt:

1. Auf der untersten Ebene wird der Fernfeldrepräsentant aller Elemente im schraffierten Cluster berechnet.
2. Der Fernfeldrepräsentant wird in Nahfeldrepräsentanten für die Interaktionsliste umgewandelt.
3. Der Fernfeldrepräsentant wird in das Zentrum des übergeordneten Clusters verschoben.
4. Die beiden vorherigen Schritte werden beim Aufwärtsdurchgang im Clusterbaum wiederholt, bis die Interaktionsliste leer ist.
5. Im Abwärtsdurchgang werden die berechneten Nahfeldrepräsentanten in die untergeordneten Cluster verschoben.
6. Auf der untersten Ebene wird der Nahfeldrepräsentant für jedes Randelement ausgewertet und die Nahfeldbeiträge durch eine direkte Auswertung der Fundamentallösung addiert.

Die benötigte Entwicklungslänge für die Multipol-Repräsentanten hängt sowohl von der Frequenz als auch von den Cluster-Durchmessern ab. Für geeignet gewählte Parameter ist die Rechenzeit und der Speicherbedarf für die Berechnung der Schallabstrahlung von einem L-Gebiet mit neun Elementen pro Wellenlänge in Abbildung 2 dargestellt. Man beobachtet den quasi-linearen Anstieg und die deutliche

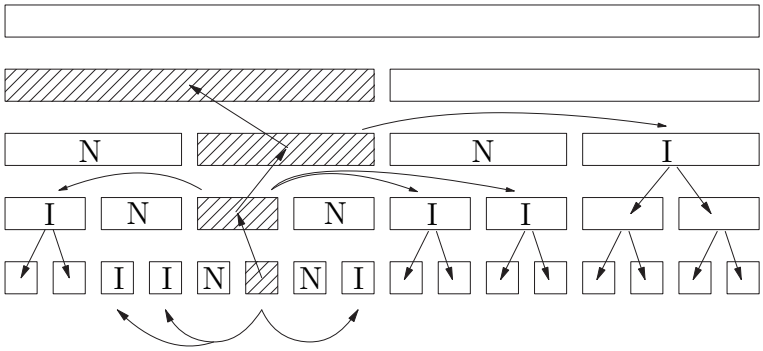

Abbildung 1: Informationsaustausch im Clusterbaum.

Reduktion des numerischen Aufwands bei der Multipol-BEM für Modelle mit vielen Freiheitsgraden. Über das akademische Beispiel des L-Gebiets hinausgehend wird die Multipol-BEM zur Berechnung der Schallabstrahlung von einer schwingenden Bremsscheibe eingesetzt. Die Randbedingungen für das Akustikgebiet werden dabei von einer instabilen Struktureigenform vorgegeben, die maßgeblich für das Bremsenquietschen verantwortlich ist. Die Multipol-BEM führt für diesen praktischen Anwendungsfall zu einer deutlichen Effizienzsteigerung und einer Halbierung der benötigten Rechenzeit im Vergleich zur herkömmlichen Randelementmethode.

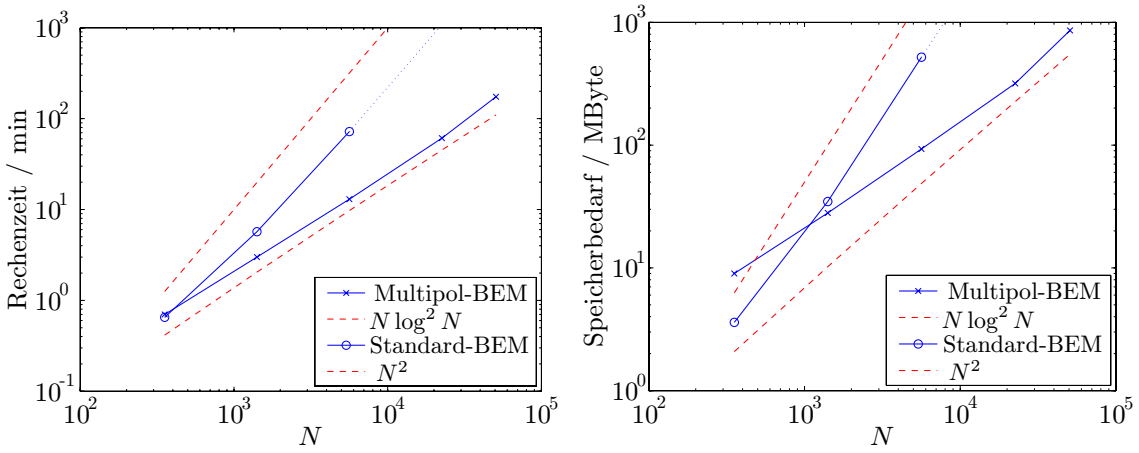

Abbildung 2: Rechenzeit und Speicherbedarf über der Anzahl der Freiheitsgrade N für die Berechnung der Schallabstrahlung von einem L-Gebiet mit neun Elementen pro Wellenlänge.

Für die Berechnung von Randelementmodellen mit vielen Freiheitsgraden müssen iterative Gleichungslöser eingesetzt werden. Die bei der Akustik-BEM entstehenden Gleichungssysteme stellen dabei hohe Anforderungen an die Lösungsverfahren: sie sind nicht symmetrisch und nicht positiv definit. In der vorliegenden Arbeit wird

die Effizienz der vorkonditionierten generalized minimal residual (GMRES) Methode und eines Mehrgitterlösers verglichen. Für die Vorkonditionierung beziehungsweise als Glätter für den Mehrgitterlöser wird ein Approximate-Inverse-Ansatz verwendet. Durch Operator-Splitting wird eine dünn besetzte Näherung des Randintegraloperators berechnet, dessen Inverse direkt approximiert und als Vorkonditionierungsmatrix eingesetzt wird. Durch die Approximate-Inverse-Vorkonditionierung stellen sowohl GMRES als auch der Mehrgitterlöser attraktive Alternativen dar. Für den praktischen Einsatz empfiehlt sich GMRES, da im Gegensatz zum Mehrgitterlöser keine Gitterhierarchie benötigt wird.

In vielen Anwendungen kann die Rückwirkung des akustischen Felds auf die Strukturschwingung vernachlässigt werden. Für sehr dünne, flexible Strukturen ist dies jedoch nicht zulässig, weil die Impedanzunterschiede geringer werden und daher die gekoppelten Feldgleichungen gelöst werden müssen. Zur Simulation der Strukturschwingung wird die Finite-Element-Methode (FEM) für eine Kirchhoff-Platte verwendet. Die Kopplung zwischen der FEM für die Strukturschwingung und der BEM für das Akustik-Feld wird durch einen Mortar-Algorithmus realisiert. Der Druck auf der Plattenoberfläche wird dabei als Lagrange-Multiplikator interpoliert, was die Kopplung von nicht-konformen Diskretisierungen erlaubt. Dadurch können spezielle Ansatz-Funktionen und eine adaptive Netzverfeinerung in den Teilgebieten verwendet werden. Zur Lösung des entstehenden Sattelpunktproblems wird ein Uzawa-Algorithmus eingesetzt. Die reduzierte Gleichung für den Lagrange-Multiplikator wird durch GMRES-Iterationen gelöst, wobei in jedem äußeren Iterationsschritt das innere BEM-System durch eine relaxierte GMRES-Methode mit Vorkonditionierung angenähert wird. Dieses Lösungsverfahren ermöglicht den Einsatz der Multipol-BEM für gekoppelte Berechnungen und damit die Simulation von großen Randelementmodellen.

Die Leistungsfähigkeit des Mortar-Algorithmus wird am Beispiel einer elastischen Platte, die mit einem akustischen Innenraumproblem gekoppelt ist, demonstriert. Für dieses Problem wird eine Reihenlösung entwickelt, die als Referenz für die numerischen Ergebnisse dient. In Abbildung 3 ist der berechnete Frequenzgang für die Plattenverschiebung dargestellt. Man erkennt deutlich die gute Übereinstimmung zwischen numerischer und analytischer Lösung. Das Konvergenzverhalten des FEM-BEM-Verfahrens wird bei einer Frequenz von 180 Hz untersucht. Für eine unabhängige Verfeinerung der FEM- und BEM-Netze werden die Fehler der berechneten Felder diskutiert. Als weiteres Beispiel werden Versuche zur aktiven Akustik-Struktur-Regelung simuliert, die im Hydroakustik-Labor des Instituts A für Mechanik durchgeführt werden.

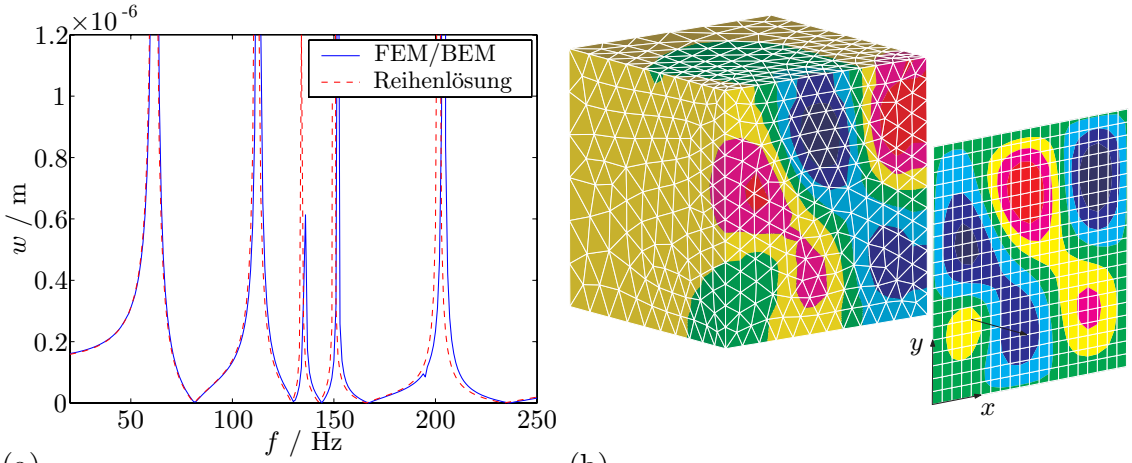

(a) (b)

Abbildung 3: Elastische Platte gekoppelt mit akustischem Innenraum. (a) Plattenverschiebung w in Abhängigkeit der Frequenz f, Anregung der Platte durch Einzelkraft an Position $(0,2; 0,3)$ m. (b) Oberflächenverteilung des akustischen Drucks und davor der Plattenverschiebung bei 180 Hz.

Für eine effiziente Simulation von Akustikfeldern und Akustik-Struktur-Interaktionseffekten müssen hochentwickelte numerische Verfahren eingesetzt werden. In der vorgestellten Arbeit wird die Randelementmethode mit einem Multipol-Algorithmus kombiniert, der eine schnelle Auswertung der Matrix-Vektor-Produkte ermöglicht. In Zusammenspiel mit iterativen Lösungsverfahren und geeigneter Vorkonditionierung können Modelle mit mehr als 100.000 Randelementen berechnet werden. Zur Simulation der Akustik-Struktur-Interaktion wird die Multipol-BEM mit der FEM für Kirchhoff-Platten über einen Mortar-Algorithmus gekoppelt. Die hohe Flexibilität bei der Diskretisierung der Teilgebiete ermöglicht auch hier die Berechnung von komplexen technischen Strukturen auf sehr detaillierten Modellen.

Chapter 1

Introduction

1.1 Motivation

The acoustic behavior is a major concern in product development, since noise level and sound quality strongly influence the customers' buying decision. Structural-acoustic simulations are an important tool to predict the acoustic properties of the new product early in the design phase. The simulation results help to optimize the product, yielding a superior quality and saving time and money.

The acoustic field is computed by the solution of boundary value problems for the Helmholtz equation. At low frequencies, discretization methods provide very accurate simulation results. Most widely used are the finite element method (FEM) (Ihlenburg, 1998) and the boundary element method (BEM) (Gaul et al., 2003). A wast amount of engineering experience is available for the FEM because of its application in structural mechanics. However, the FEM is only applicable to bounded domains. For exterior acoustic problems, special schemes—e.g. artificial absorbing boundary conditions, perfectly matched layers, or infinite elements—must be applied that quickly reduce the efficiency of the method. In contrast, when using the BEM, the Sommerfeld radiation condition is implicitly fulfilled. A further advantage of the BEM is the reduction of the problem dimension: only the boundary of the sound-radiating structure must be discretized. The cost of preprocessing and mesh generation is thus greatly reduced. The main disadvantage of the BEM are its fully populated system matrices and the arising computing cost and memory requirements of order N^2 in the number of unknowns.

With increasing frequency, the mesh used for the FEM or BEM simulations must be refined to resolve the oscillations of the acoustic field. In engineering practice,

six to ten linear elements per wavelength are used as a rule of thumb to yield an accuracy of the approximated solution of a few percent. One notices that the computing cost increases quickly: doubling the frequency for a three-dimensional problem would require eightfold finite elements or fourfold boundary elements. Thus, the application of the two methods is limited to the low frequency range. For high frequencies, statistical methods like the statistical energy analysis (SEA) (Lyon and DeJong, 1995) yield valuable simulation results. In between, i.e. for frequencies of typically a few hundred Hertz, the cost of discretization methods is too high whereas the accuracy of statistical methods is too low. A problem known as the mid-frequency gap.

To close this mid-frequency gap, the BEM offers greater potential than the FEM due to the reduced problem dimension. However, the limiting factor for the application of the BEM are the fully populated system matrices. The numerical cost cannot be handled—even for a moderate number of unknowns—by standard implementations. Significant research effort has been spent in recent years to tackle this disadvantage and to develop a fast BEM. The proposed algorithms can be divided into two major groups: matrix compression algorithms and techniques for the fast evaluation of the matrix-vector products. Wavelet bases (Schneider, 1998), $\mathcal{H}$-matrices (Hackbusch, 1999), and adaptive cross approximation (Bebendorf and Rjasanow, 2003) are the most prominent examples of the first group. Panel clustering and multipole BEM are examples of the second group that are compared in the dissertation of Giebermann (1997).

The application of fast BEM to acoustics is not straight-forward, since the oscillating behavior of the solution poses additional difficulties. In this thesis, the fast multipole BEM is chosen and adapted to the Helmholtz equation. The developed algorithm has a complexity of order $N \log^2 N$ for simulations with a constant number of elements per wavelength. The fast multipole BEM is thus much faster than the traditional BEM for large-scale problems and allows to extend the application limit to higher frequencies. For large-scale computations, the system of equations cannot be solved directly, but iterative methods must be applied. However, high frequencies and fine discretizations yield a poor conditioning and require a large number of iterations. Thus, the construction of a preconditioner that limits the influence of frequency and mesh size h on the iteration count is required.

Very often one can perform structural-acoustic simulations neglecting the influence of the acoustic field on the vibration behavior of the structure. However, this is not acceptable for thin and flexible structures that are easily excited by the acoustic pressure. This situation is encountered e.g. for payloads in aerospace vehicles, partitioning walls, or piping systems. In such applications, the acoustic field must be fully

coupled to the vibrating structure. For the simulation of structural vibrations, the FEM is the method of choice in engineering practice. Thus, a FEM-BEM coupling algorithm is required for the simulation of the structure-acoustic field interaction. The mortar method proposed by Bernardi et al. (1994) can be adapted to FEM-BEM coupling to yield a high flexibility in the choice of discretizations. The coupling algorithm allows the combination of non-conforming meshes what permits the use of specialized ansatz functions and adaptive mesh refinement in the subdomains.

The goal of this thesis is to provide a complete package for efficient structural-acoustic simulations that can be applied to industrial-scale problems. The building blocks are an efficient Galerkin boundary element formulation for the simulation of the acoustic field, a fast evaluation of the BEM matrix-vector products using the multipole algorithm, an efficient solution of the system of equations by preconditioned iterative solvers, and a mortar coupling algorithm for structure-acoustic field interaction problems.

The development and implementation of the presented algorithms could not have succeeded without the close collaboration within the SFB 404 “Multifield Problems in Solid and Fluid Mechanics” and without the help of motivated Master students. I would like to take the opportunity and refer exemplarily to the multipole article by Of et al. (2002) and to the contributions of Gauger (2002), Sidhu (2002), and Perfahl (2003; 2004).

1.2 Literature overview

1.2.1 Boundary element methods in acoustics

Boundary element methods are well established in various fields of engineering. From a wide range of textbooks, it is referred to the books of Gaul et al. (2003) and Steinbach (2003a) for an introduction to the method. Acoustics is a major field of application for the BEM because exterior acoustic problems can be dealt with easily. An up-to-date overview is given in the collections edited by Wu (2000) and von Estorff (2000).

The BEM was first used to predict the sound radiation from a vibrating body in a paper by Chen and Schweikert (1963). Soon the problem of critical frequencies appeared: the boundary integral equation does not allow a unique solution for the exterior domain at resonance frequencies of the associated interior problem. Schenck (1968) proposed the CHIEF method that requires additional collocation points in

the domain. An alternative that proved to perform more reliable was introduced by Burton and Miller (1971).

The Burton-Miller approach uses a linear combination of the standard and the hyper-singular boundary integral equation. For the evaluation of the hyper-singular operator, it is advantageous to use a Galerkin formulation as introduced for the BEM by Sirtori (1979). An overview on Galerkin BEM is compiled by Bonnet et al. (1998) whereas for Galerkin BEM in acoustics, it is referred to Chen et al. (1997). Special attention has to be paid to the numerical integration of singular integrals in the Galerkin BEM. Transformation schemes are derived in the dissertation of Sauter (1992) and a follow-up paper (Sauter and Krapp, 1996) provides a detailed discussion of quadrature errors.

In recent years, the focus of research in boundary element acoustics is on improved efficiency. Some aspects are the choice of ansatz functions (Marburg and Schneider, 2003a), frequency-band analysis (von Estorff and Zaleski, 2003), and the implementation of iterative solvers (Marburg and Schneider, 2003b; Ochmann et al., 2003). These are important improvements for the every-day use of the BEM, however, they cannot remedy the principal limitation of the fully populated matrices.

1.2.2 Fast multipole boundary element method

The fast multipole method (FMM) was originally developed by Greengard and Rokhlin (1987) for the simulation of large particle fields in physics. Since then, it has been applied in many areas of simulation sciences and is considered by some authors as one of the top ten algorithms of the 20th century (Board and Schulten, 2000). The application of the multipole algorithm to accelerate the BEM is triggered by the similarity between the potential in particle simulations and the fundamental solution in the kernels of the boundary integral operators. The key idea is to approximate the fundamental solution at some distance from the source point by a multipole series expansion. A multilevel scheme, then, allows the efficient evaluation of the matrix-vector product. A state of the art review on multipole boundary integral methods for various applications is presented by Nishimura (2002). The development of the multipole BEM for the Helmholtz equation is closely connected to research on the Maxwell equation for electro-magnetic fields. For a detailed survey on the fast solution of integral equations for the Maxwell equation, it is referred to the review article by Chew et al. (2003).

For acoustic simulations at higher frequencies, a large expansion length is required for the multipole method. This leads to a prohibitive computing cost for the stan-

dard multipole expansion which is comparable to the traditional BEM. A diagonal form of the multipole expansion that is developed by Rokhlin (1990) shows a much improved numerical behavior. The theory for diagonal translation operators in three-dimensional acoustics is developed as well by Rokhlin (1993) and presented for "pedestrians" in the paper by Coifman et al. (1993). This paper also includes empirical rules for the choice of the required expansion length that is very critical for the efficiency of the multipole BEM. The error committed when truncating the diagonal expansion is discussed in more detail by Rahola (1996) and Koc et al. (1999) or from a mathematical point of view by Darve (2000). Several groups provide valuable work on some details of the method. Exemplarily the papers by Epton and Dembart (1995) and Gyure and Stalzer (1998) are worth to be mentioned.

The application of the multipole method to engineering BEM simulations in acoustics has emerged lately as documented in the papers by Schneider (2003a) and Fischer et al. (2004).

1.2.3 Structure-acoustic field interaction

The introductory paper by Junger (1997) to a special issue on structure-acoustic field interaction gives an overview on traditional simulation approaches: asymptotic solutions, modal and wavenumber concepts. More lately, discretization methods have become popular for the simulation of coupled structural-acoustic systems. Pure FEM formulations are already widely used. The performance for interior acoustic problems in automotive industry is documented for example in the paper by Kropp and Heiserer (2003). The first FEM–BEM coupling algorithm is developed by Everstine and Henderson (1990). Chen et al. (1998) propose a variational coupling scheme for Galerkin methods. Further developments and application of FEM–BEM methods for structural–acoustic simulations is a broad area of research. Moosrainer (2000) examines several approximation techniques for the BEM in coupling schemes. Gaul and Wenzel (2002) use a hybrid boundary element formulation. Non-linear effects are considered by Czygan and von Estorff (2002) and the important application of sound transmission through windows is covered by Langer and Antes (2003).

In recent years, the mathematical theory for domain decomposition methods has quickly advanced. The extended theoretical insight can give valuable motivation for the engineering application of coupling schemes. In particular the mortar element method that is originally introduced by Bernardi et al. (1994) offers various advantages for the simulation of structure-acoustic field interaction. Stability estimates of the mortar element method for three-dimensional problems are derived by Braess and Dahmen (1998) and a mortar formulation with Lagrange multipliers is

proposed by Ben Belgacem (1999). The efficient choice of the ansatz space for the Lagrange multiplier is discussed by Wohlmuth (2000). The use of boundary integral formulations in hybrid domain decomposition methods is covered in the monograph by Steinbach (2003b).

1.3 Outline of contents

In Chapter 2, a short introduction to the Galerkin boundary element method for acoustics is presented. A symmetric formulation for mixed boundary value problems and a formulation based on the Burton-Miller approach for exterior acoustic Neumann problems are developed. Numerical integration techniques for the evaluation of the singular boundary integrals are derived in Appendix A, a regularization technique for the hyper-singular operator is presented in Appendix B. Chapter 3 focuses on the efficient evaluation of the BEM matrix-vector products using the fast multipole method. The implementation of the diagonal translation operators for the Helmholtz equation in a multilevel scheme is presented and the influence of the expansion length on accuracy and efficiency of the method is discussed. Numerical examples demonstrate the quasi-linear complexity of the fast multipole BEM and the largely reduced computing cost compared to standard boundary element formulations. The iterative solution of the BEM system is covered in Chapter 4. The generalized minimal residual method (GMRES) is compared to a multigrid solver. For both, an approximate inverse approach is employed as preconditioner and smoother, respectively, that restricts the growth of required iterations with mesh refinement and increasing frequencies. In Chapter 5, a mortar FEM-BEM coupling algorithm for the simulation of structure-acoustic field interaction is developed. For the solution of the arising saddle point problem, an inexact Uzawa algorithm is employed. The inner FEM and BEM systems are approximated using conjugate gradient and GMRES iterations, respectively. For the outer iterations on the reduced equation for the Lagrange multiplier, GMRES is applied. The flexibility of the mortar coupling scheme is demonstrated for a plate backed by an acoustic cavity for that a series solution is derived in Appendix C.

Chapter 2

Galerkin BEM for acoustics

2.1 Boundary integral formulation for the Helmholtz equation

For time harmonic behavior $\mathrm{e}^{-\mathrm{i}\omega t}$, the pressure p in an acoustic field is governed by the Helmholtz equation (Fahy, 2001; Cremer and Möser, 2003)

$$\nabla^2 p(x) + \kappa^2 p(x) = 0 \,, \tag{2.1}$$

where $\kappa = \omega/c$ is the acoustic circular wavenumber. The relation to the wavelength λ is given by $\kappa = 2\pi/\lambda$. Here, the Helmholtz equation is solved in an exterior domain Ω^{e} which is the complement to the open set $\Omega \subset \mathbb{R}^3$ with boundary $\partial\Omega = \Gamma = \Gamma^{\mathrm{N}} \cup \Gamma^{\mathrm{D}}$ as depicted in Fig. 2.1. The acoustic flux is defined as $q = \partial p/\partial n$ where the unit normal n to Γ is defined to point outwards from Ω. On the Dirichlet boundary Γ^{D} the acoustic pressure is prescribed as

$$p(x) = \bar{p}(x) \,, \qquad x \in \Gamma^{\mathrm{D}} \,, \tag{2.2}$$

on the Neumann boundary Γ^{N} the acoustic flux is prescribed as

$$\frac{\partial p(x)}{\partial n} = \bar{q}(x) \,, \qquad x \in \Gamma^{\mathrm{N}} \,, \tag{2.3}$$

corresponding to the surface velocity of a vibrating structure. Furthermore, the Sommerfeld radiation condition has to be fulfilled, i.e.,

$$\left| \frac{\partial p}{\partial r} - \mathrm{i}\kappa p \right| \leq \frac{c}{r^2} \quad \text{at } r \to \infty \,. \tag{2.4}$$

A given boundary impedance corresponds to Robin boundary conditions, a linear combination of Dirichlet and Neumann data. Although of practical relevance, impedance boundary conditions are neglected throughout this thesis.

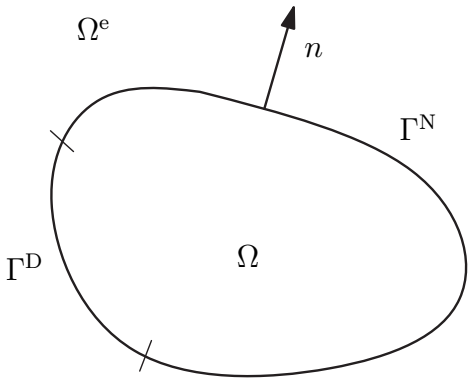

Figure 2.1: Exterior acoustic domain

The derivation of boundary integral formulations starts with the weak form of the Helmholtz equation (2.1) (Gaul et al., 2003)

$$\int_{\Omega^{\mathrm{e}}} P^*(x,y) \left(\nabla^2 p(x) + \kappa^2 p(x)\right) \,\mathrm{d}x = 0\,. \tag{2.5}$$

The fundamental solution $P^*(x,y)$ is chosen as weighting function. For the Helmholtz equation in three-dimensional space, it is given by

$$P^*(x,y) = \frac{1}{4\pi}\,\frac{\mathrm{e}^{\mathrm{i}\kappa r}}{r}\,, \tag{2.6}$$

where $r = \mid x - y \mid$ is the Euclidean distance between the field or receiver point x and the source or load point y. Applying Green's second theorem on (2.5) yields the representation formula

$$p(x) = -\int_\Gamma P^*(x,y)\, q(y) \;\mathrm{d}s_y + \int_\Gamma \frac{\partial P^*(x,y)}{\partial n_y}\, p(y) \;\mathrm{d}s_y\,, \qquad x \in \Omega^{\mathrm{e}}\,. \tag{2.7}$$

Taking the limit of (2.7) on the smooth boundary $\Omega^{\mathrm{e}} \ni x \to \Gamma$, one obtains the boundary integral equation

$$p(x) = \frac{1}{2}p(x) - \underbrace{\int_\Gamma P^*(x,y)\, q(y) \;\mathrm{d}s_y}_{(Vq)(x)} + \underbrace{\int_\Gamma \frac{\partial P^*(x,y)}{\partial n_y}\, p(y) \;\mathrm{d}s_y}_{(Kp)(x)}\,, \quad x \in \Gamma\,, \tag{2.8}$$

where $(Vq)(x)$ and $(Kp)(x)$ are the single and double layer potential, respectively. The hyper-singular boundary integral equation is obtained by taking the normal derivative of (2.7) on the smooth boundary $\Omega^{\mathrm{e}} \ni x \to \Gamma$

$$q(x) = \frac{1}{2}q(x) - \underbrace{\int_\Gamma \frac{\partial P^*(x,y)}{\partial n_x}\, q(y) \;\mathrm{d}s_y}_{(K'q)(x)} + \underbrace{\int_\Gamma \frac{\partial^2 P^*(x,y)}{\partial n_x \partial n_y}\, p(y) \;\mathrm{d}s_y}_{-(Dp)(x)}\,, \quad x \in \Gamma\,, \tag{2.9}$$

where $(K'q)(x)$ and $(Dp)(x)$ are the adjoint double layer potential and the hyper-singular operator, respectively. Combining the two boundary integral equations, one obtains the system

$$\begin{pmatrix} p \\ q \end{pmatrix} = \underbrace{\begin{pmatrix} \frac{1}{2}I + K & -V \\ -D & \frac{1}{2}I - K' \end{pmatrix}}_{\mathcal{C}} \begin{pmatrix} p \\ q \end{pmatrix} , \tag{2.10}$$

which defines the Calderón operator $\mathcal{C}$ that projects the Cauchy data on themselves. A very detailed discussion of the properties of the boundary integral operators for the Helmholtz equation is found in Nédélec (2001).

2.2 Symmetric Galerkin formulation

To obtain a symmetric Galerkin formulation for mixed boundary value problems, the acoustic pressure and flux are decomposed as $p = \tilde{p} + \bar{p}$ and $q = \tilde{q} + \bar{q}$, respectively. For the new fields, it holds $\tilde{p} = 0$ on Γ^{D} and $\tilde{q} = 0$ on Γ^{N}.

On the Dirichlet boundary, the standard boundary integral equation (2.8) is weighted with test functions v^q

$$\begin{aligned} \int_{\Gamma^{\mathrm{D}}} v^q (V\tilde{q})(x)\,\mathrm{d}s_x - \int_{\Gamma^{\mathrm{D}}} v^q (K\tilde{p})(x)\,\mathrm{d}s_x \\ = -\int_{\Gamma^{\mathrm{D}}} v^q (V\bar{q})(x)\,\mathrm{d}s_x + \int_{\Gamma^{\mathrm{D}}} v^q \left(-\frac{1}{2}I + K\right)\bar{p}(x)\,\mathrm{d}s_x \,. \end{aligned} \tag{2.11}$$

On the Neumann boundary, the hyper-singular integral equation (2.9) is weighted with test functions v^p

$$\begin{aligned} \int_{\Gamma^{\mathrm{N}}} v^p (K'\tilde{q})(x)\,\mathrm{d}s_x + \int_{\Gamma^{\mathrm{N}}} v^p (D\tilde{p})(x)\,\mathrm{d}s_x \\ = -\int_{\Gamma^{\mathrm{N}}} v^p (D\bar{p})(x)\,\mathrm{d}s_x + \int_{\Gamma^{\mathrm{N}}} v^p \left(-\frac{1}{2}I - K'\right)\bar{q}(x)\,\mathrm{d}s_x \,. \end{aligned} \tag{2.12}$$

For the approximate solution of (2.11) and (2.12) a triangulation of the boundary is introduced. The acoustic pressure is discretized using linear shape functions $\boldsymbol{\varphi}^p(x)$ on the boundary triangulation

$$\tilde{p}_h = \boldsymbol{\varphi}^p(x)^{\mathrm{T}}\mathbf{p}\,, \tag{2.13}$$

where $\mathbf{p}$ contains the nodal pressure values. For the acoustic flux, constant shape functions $\boldsymbol{\varphi}^q(x)$ are chosen since they allow a discontinuous discretization which

proves to perform more efficiently (Marburg and Schneider, 2003a)

$$\tilde{q}_h = \boldsymbol{\varphi}^q(x)^{\mathrm{T}}\mathbf{q}\,. \tag{2.14}$$

Using an isoparametric concept, i.e. a constant approximation for v^q and a linear approximation for v^p, yields the block skew symmetric BEM system of equations

$$\begin{pmatrix} \mathbf{V} & -\mathbf{K} \\ \mathbf{K}^{\mathrm{T}} & \mathbf{D} \end{pmatrix} \begin{pmatrix} \mathbf{p} \\ \mathbf{q} \end{pmatrix} = \begin{pmatrix} \mathbf{f}^{\mathrm{D}} \\ \mathbf{f}^{\mathrm{N}} \end{pmatrix}\,, \tag{2.15}$$

with the right hand side column matrices

$$\mathbf{f}^{\mathrm{D}} = -\int_{\Gamma^{\mathrm{D}}} \boldsymbol{\varphi}^q(x)(V\bar{q})(x)\,\mathrm{d}s_x + \int_{\Gamma^{\mathrm{D}}} \boldsymbol{\varphi}^q(x)\left(-\frac{1}{2}I + K\right)\bar{p}(x)\,\mathrm{d}s_x\,, \tag{2.16}$$

$$\mathbf{f}^{\mathrm{N}} = -\int_{\Gamma^{\mathrm{N}}} \boldsymbol{\varphi}^p(x)(D\bar{p})(x)\,\mathrm{d}s_x + \int_{\Gamma^{\mathrm{N}}} \boldsymbol{\varphi}^p(x)\left(-\frac{1}{2}I - K'\right)\bar{q}(x)\,\mathrm{d}s_x\,. \tag{2.17}$$

The computation of the boundary element system matrices requires the evaluation of singular integrals for $x \to y$. Transformation rules for the Galerkin BEM are derived in Appendix A that allow an efficient numerical quadrature. The hyper-singular operator exhibits a strong singularity $1/|x-y|^3$ and is thus not an integrable function. Applying Stokes' theorem, the entry τ, σ of matrix $\mathbf{D}$ is computed as

$$\begin{aligned}
\mathbf{D}[\tau,\sigma] =& \sum_{\nu\in\mathcal{E}(\tau)}\int_\nu \sum_{\mu\in\mathcal{E}(\sigma)}\int_\mu \varphi^p_\tau|_\nu(x)\;\varphi^p_\sigma|_\mu(y)\;\frac{\partial^2 P^*(x,y)}{\partial n_x \partial n_y}\;\mathrm{d}s_y\,\mathrm{d}s_x \\
=& \sum_{\nu\in\mathcal{E}(\tau)}\int_\nu \sum_{\mu\in\mathcal{E}(\sigma)}\int_\mu \kappa^2 n_x\cdot n_y\,\varphi^p_\tau|_\nu(x)\;\varphi^p_\sigma|_\mu(y) P^*(x,y)\;\mathrm{d}s_y\,\mathrm{d}s_x \\
& - \sum_{\nu\in\mathcal{E}(\tau)}\int_\nu \sum_{\mu\in\mathcal{E}(\sigma)}\int_\mu \underbrace{(n_x\times\nabla_x\varphi^p_\tau|_\nu(x))}_{\mathrm{curl}_\Gamma(\varphi^p_\tau|_\nu(x))} (n_y\times\nabla_y\varphi^p_\sigma|_\mu(y))\,P^*(x,y)\;\mathrm{d}s_y\,\mathrm{d}s_x\,,
\end{aligned} \tag{2.18}$$

where $\nu \in \mathcal{E}(\tau)$ denotes all elements ν connected to node τ and $\varphi^p_\tau|_\nu(x)$ is the linear shape function corresponding to node τ restricted to element ν. The expressions are defined analogous for the element μ and node σ. $\mathrm{curl}_\Gamma(\varphi^p_\tau|_\nu(x))$ is constant on linear elements, thus, computing the hyper-singular operator requires the evaluation of the single layer potential for linear and constant shape functions. More details on the regularization—in particular for the situation using the multipole BEM—are presented in Appendix B.

2.3 Burton-Miller formulation

For exterior acoustic simulations of Neumann problems, critical frequencies occur due to the properties of the boundary integral formulation. The operator $(-\frac{1}{2}I +$

$K)p(x)$ is not invertible when κ corresponds to an eigenfrequency of the associated interior Dirichlet problem for the Laplacian, whereas $(Dp)(x)$ is not invertible when κ corresponds to an eigenfrequency of the associated interior Neumann problem. A linear combination of (2.8) and (2.9)—the Burton-Miller approach—has a unique solution for all frequencies. This procedure can be traced back to the work by Brakhage and Werner (1965) and is applied to the BEM by Burton and Miller (1971). The coupling parameter for the two integral equations is chosen to yield a favorable condition number for the combined operator. Motivated by the behavior of the eigenvalues for the Helmholtz equation on a unit sphere, Kress (1985) shows the quasi-optimality of the factor i/κ by numerical studies. Multiplying (2.9) by i/κ and inserting the given Neumann boundary conditions $\bar{q}$, one obtains the combined equation

$$(-\frac{1}{2}I + K)p(x) + \frac{\mathrm{i}}{\kappa}(Dp)(x) = (V\bar{q})(x) - \frac{\mathrm{i}}{\kappa}(\frac{1}{2}I + K')\bar{q}(x)\,. \tag{2.19}$$

A Galerkin formulation is obtained by weighting (2.19) with test functions v

$$\begin{aligned}\int_\Gamma v(x)(-\frac{1}{2}I + K)p(x)\,\mathrm{d}s_x + \frac{\mathrm{i}}{\kappa}\int_\Gamma v(x)(Dp)(x)\,\mathrm{d}s_x \\ = \int_\Gamma v(x)(V\bar{q})(x)\,\mathrm{d}s_x - \frac{\mathrm{i}}{\kappa}\int_\Gamma v(x)(\frac{1}{2}I + K')\bar{q}(x)\,\mathrm{d}s_x\,.\end{aligned} \tag{2.20}$$

Triangulation of the boundary Γ yields an approximate solution p_h on the boundary element space of piecewise linear shape functions $\boldsymbol{\varphi}^p(x)$. The Neumann data is interpolated using constant shape functions $\boldsymbol{\varphi}^q(x)$.

$$p_h(x) = \boldsymbol{\varphi}^p(x)^{\mathrm{T}}\mathbf{p}\,, \qquad \bar{q}_h(x) = \boldsymbol{\varphi}^q(x)^{\mathrm{T}}\bar{\mathbf{q}}\,. \tag{2.21}$$

Testing with isoparametric, linear shape functions yields the system of equations

$$\left(-\frac{1}{2}\mathbf{I} + \mathbf{K} + \frac{\mathrm{i}}{\kappa}\mathbf{D}\right)\mathbf{p} = \left(\mathbf{V} - \frac{\mathrm{i}}{2\kappa}\mathbf{I}' - \frac{\mathrm{i}}{\kappa}\mathbf{K}'\right)\bar{\mathbf{q}}\,. \tag{2.22}$$

2.4 Numerical examples

Two different geometries are employed for testing the BEM formulations for exterior acoustic Neumann problems: an L-shaped domain and a brake disk. The examples are scattered throughout the thesis to demonstrate the properties of the developed algorithms. In Chapter 5 on structure-acoustic field interaction, different examples are employed that are presented on the spot.

The algorithms are implemented in C++ using the Microsoft Visual C++ compiler. The GNU scientific library is employed for the evaluation of special functions, whereas the BLAS is provided by the Intel Math Kernel library. Floating point operations are performed in double precision. For the development of the algorithms, two side conditions are set: first, large-scale structural-acoustic computations should be possible "over night", and second, they should run on common hardware. The first requirement is important for the engineering application of the methods in product development, the second allows the parallel computation of a frequency response function if a PC cluster is available. All simulations presented in the thesis run on a Pentium 4 personal computer at 2.4 GHz with a memory of 1.5 GBytes. Computing times and memory requirements are taken from the system log files. It is well understood that computing time measured in this way scatters significantly. The presented numbers are an average of several simulation runs and it was paid attention that no other jobs run on the machine concurrently.

The choice of a suitable quadrature scheme has a dominating influence on the computing time. For the set up of the BEM matrices, the boundary integral operators must be evaluated by a double integration over all elements. For the singular integrals, i.e. if the pair of elements is identical or adjacent, the transformations presented in Appendix A are employed that provide an efficient evaluation at a high accuracy. For the regular integrals, special Gauss quadrature rules for triangles are used. In a two-step scheme, seven Gauss points are chosen if the two elements are at a close distance, three Gauss points are chosen if their distance is larger than five element diameters. The applied quadrature rule gives a very precise evaluation of the boundary integrals and integration errors can be neglected throughout the numerical examples. In engineering practice, one would typically allow a quadrature error in the same order of magnitude as the discretization error, i.e. a few per cent, which cuts the computing time typically by a factor of three. One Gauss point per element is sufficient for the majority of element pairs which means that the double surface integration in the Galerkin BEM is performed at the same cost as the simple surface integration and collocation in the collocation BEM.

2.4.1 Sound radiation from an L-shaped domain

An L-shaped geometry with an edge length of $a = 1\,\mathrm{m}$ is chosen as a standard test case. Corners and edges of the L-shape make high demands on the numerical methods, thus, allowing to transfer the findings to practical applications. The Neumann boundary conditions on the L-shape are generated by applying monopole sources inside and computing the acoustic flux $\bar{q}$ on the surface. The advantage of this

Table 2.1: BEM discretizations of L-shape.

	nodes	elements	$f_{\max}$	$\kappa_{\max} a$
L4	90	176	150 Hz	2.77
L8	354	704	300 Hz	5.54
L16	1410	2816	600 Hz	11.09
L32	5634	11264	1200 Hz	22.18
L64	22530	45056	2400 Hz	44.35
L96	50690	101376	3600 Hz	66.53

procedure is that the exact boundary pressure p^Γ is known and can be used as a reference for the BEM solution p^Γ_{BEM}. For the L_2 Dirichlet error on the surface of the L-shape, the pressure fields are evaluated on the nodes of the boundary element discretization

$$e_2^\Gamma = \frac{\|\mathbf{p}^\Gamma_{\mathrm{BEM}} - \mathbf{p}^\Gamma\|_2}{\|\mathbf{p}^\Gamma\|_2} \,. \tag{2.23}$$

A family of BEM meshes is generated for the L-shape that allows the study of the convergence behavior of the proposed methods. In Tab. 2.1, the number of boundary nodes and elements of the discretizations are listed. The finest model consists of more than $100,000$ triangular boundary elements. The naming convention of the models corresponds to the number of elements per meter that is essential for the engineering rule of thumb of simulations with six to ten elements per wavelength. For orientation, the frequency $f_{\max}$ gives a ratio of $\lambda/h = 9$ for computations in air ($c = 340\,\mathrm{m/s}$; $\rho = 1.225\,\mathrm{kg/m^3}$) that result in typical precisions of a few per cent. The dimensionless factor $\kappa_{\max} a$ is listed for classification of the frequency range covered by the example.

The symmetric approach and the Burton-Miller approach are compared for the L8 model in the frequency range $150\,\mathrm{Hz} \leq f \leq 300\,\mathrm{Hz}$ which is the typical frequency range covered by that model. Fig. 2.2 shows the BEM discretization with applied Neumann boundary conditions at a frequency of 300 Hz due to a monopole source located at $(0.2,\, 0.3,\, 0.3)\,\mathrm{m}$. The error e_2^Γ of the simulations is plotted in Fig. 2.3. For the symmetric approach, one notices clearly the non-uniqueness problem at the critical frequencies. The error for the simulations using the Burton-Miller approach increases evenly with frequency as expected. The BEM systems are solved iteratively using the GMRES algorithm (Saad, 2003) and the required iterations are also plotted in Fig. 2.3. The Burton-Miller approach yields a significant better condi-

tioning of the system and requires less iterations. Due to the two advantages—no critical frequencies and good conditioning—it is recommended to use the Burton-Miller approach for exterior Neumann problems. A drawback of the Burton-Miller approach is that symmetry cannot be exploited, thus taking twice the memory for handling the system matrix. Using the fast multipole BEM, this disadvantage will prove not to be too costly.

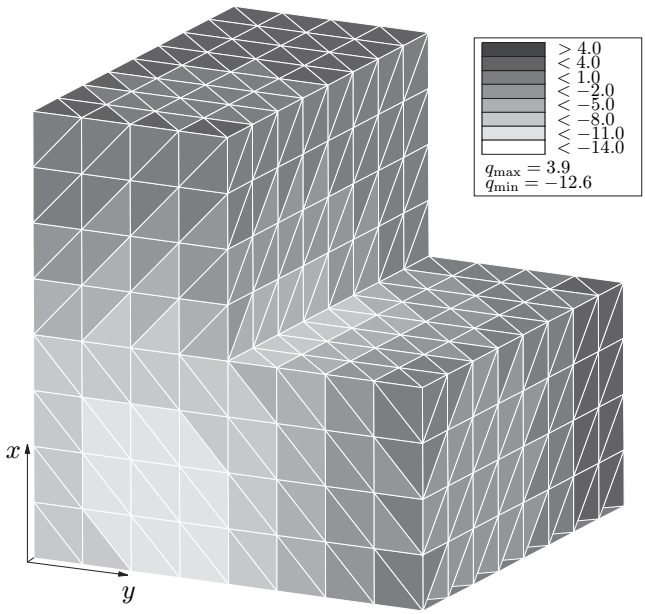

Figure 2.2: Neumann boundary conditons on L8 model. Displayed is the real part of the acoustic flux at 300 Hz.

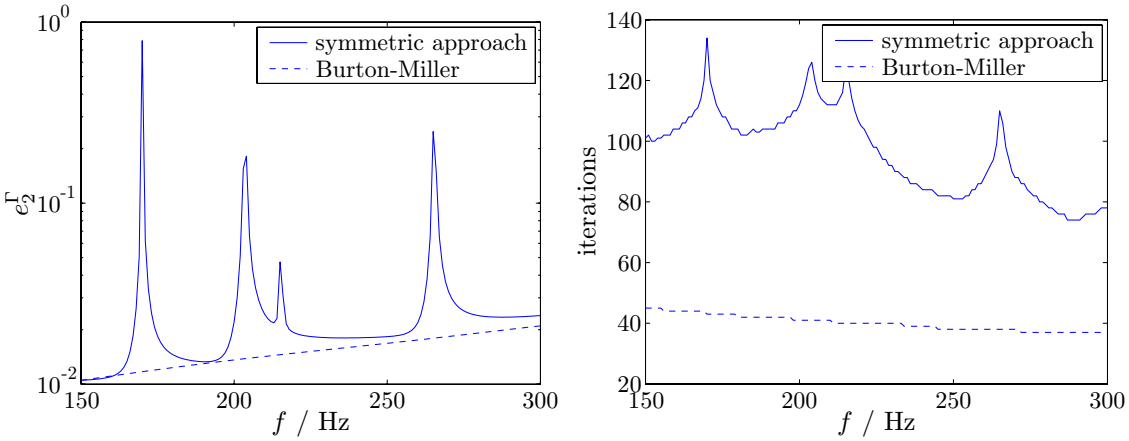

Figure 2.3: Influence of critical frequencies for exterior acoustic problems. Dirichlet error e_2^Γ and required iterations plotted against frequency f.

Table 2.2: BEM simulations for L-shape at $\kappa h = \text{const.}$

	f	memory	t_{matrix}	iterations	t_{solve}	e_2^Γ
L8	300 Hz	3.6 MB	39 sec	37	<<1 sec	0.0210
L16	600 Hz	34.7 MB	339 sec	35	1.0 sec	0.0142
L32	1200 Hz	519.4 MB	4310 sec	34	13.6 sec	0.0121

The computing cost and results of Burton-Miller simulations on the L-shape at $\kappa h = \text{const.}$ are documented in Tab. 2.2. For the models L8 to L32 at frequencies between 300 Hz and 1200 Hz, the error of the computed Dirichlet data is 1% to 2% as expected for acoustic simulations at nine elements per wavelength. The memory requirements and computing time for the set up of the system matrix t_{matrix} and the solution using GMRES t_{solve} increase somewhat below quadratic, since the cost for the administration of the BEM model and the evaluation of singular integrals contributes linearly.

2.4.2 Sound radiation from a vibrating brake disk

The second example is the sound radiation from a vibrating brake disk. This real-life application is motivated by brake squealing analysis. Brake squealing causes major warranty costs for automotive companies and is thus in the focus of industrial research. After identifying unstable eigenmodes of the brake disk that are excited by the friction conditions between brake pad and brake disk, a boundary element simulation allows the evaluation of the acoustic field.

The FEM brake disk model and the mode shape at 3720 Hz as depicted in Fig. 2.4 are provided by the Robert Bosch GmbH, Corporate Research and Development, Applied Physics. For the acoustic BEM simulation, a boundary triangulation with 4422 degrees of freedom is employed with the normal surface velocity of the displayed structural eigenmode applied as Neumann boundary condition. The computed “squealing” sound pressure field is plotted in Fig. 2.5.

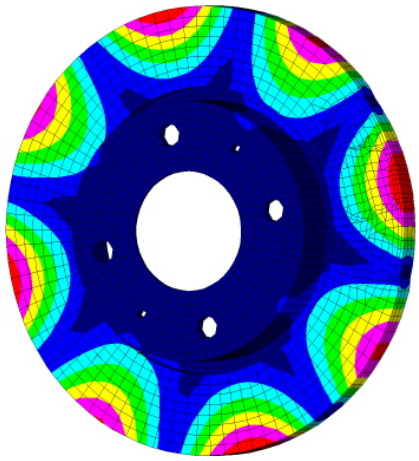

Figure 2.4: Mode shape of brake disk at 3720 Hz.

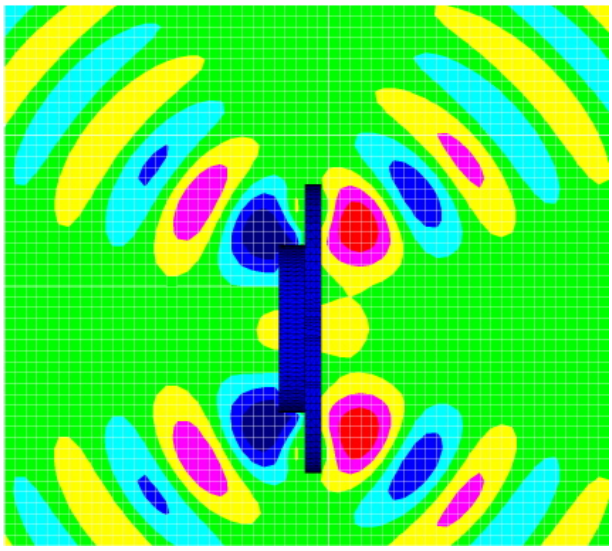

Figure 2.5: Sound field of vibrating brake disk. Displayed is the real part of the acoustic pressure computed from the mass normalized structural eigenmode at 3720 Hz.

Chapter 3

Fast multipole BEM

3.1 Preliminaries

The fully populated system matrices arising from the boundary integral operators are the major limitation of the BEM that bar the method from its application for large-scale simulations. Computing and storing the matrices involves a numerical cost of order $\mathcal{O}(N^2)$ that cannot be handled on current hardware. The multipole BEM is one example of fast BEM that reduce the asymptotic complexity of the method. The key idea of the multipole algorithm is to combine the effect of sources far away from a field point in a far-field term using the multipole expansion whereas for nearby sources standard BEM evaluations are used. In this way, the fast multilevel multipole (FMM) algorithm realizes the matrix-vector products of the BEM with a numerical cost that depends quasi-linearly on the number of unknowns.

The post office scenario is a popular example to explain the basics of the multipole algorithm. Instead of transporting letters directly from the sender to the receiver, they are dropped in a mailbox. From there they pass through a level hierarchy—post office, distribution center, post office, postman—to finally arrive at their destination in a much more efficient way.

The advantages of a series expansion approach become clear by a look at the principal computing task of the BEM. In the BEM for the Helmholtz equation, one must evaluate potentials of the type

$$\Phi(x_b) = \sum_{a=1}^{A} \frac{\mathrm{e}^{\mathrm{i}\kappa|x_b - y_a|}}{|x_b - y_a|}\, q_a\,, \qquad b = 1, 2, ..., B\,. \tag{3.1}$$

The conventional evaluation of (3.1) clearly involves a numerical cost of order

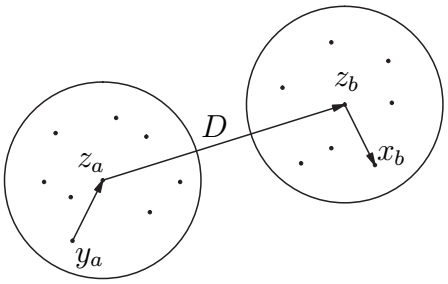

Figure 3.1: Computation of BEM potential with translation operator.

$\mathcal{O}(AB)$. If the source points y_a and field points x_b are well separated as depicted in Fig. 3.1, the multipole approach computes the action of the sources on the expansion center z_a, translates it to the center z_b, and evaluates the potential at the field points x_b. The numerical cost is of order $\mathcal{O}(A+B)$ and thus much cheaper for large A and B.

The multipole representation of the sources with respect to the expansion center is obtained by the solution of the Helmholtz equation in spherical coordinates. The field of the sources q_a can be expressed at some distance from z_a as

$$\Phi(x-z_a) = \sum_{l=0}^{\infty} \sum_{m=-l}^{l} F_{lm} h_l^{(1)}\left(\kappa|x-z_a|\right) Y_l^m\left(\frac{x-z_a}{|x-z_a|}\right), \tag{3.2}$$

where $Y_l^m(\cdot)$ are the spherical harmonics and $h_l^{(1)}(\cdot)$ are the Hankel functions of first kind that fulfill the Sommerfeld radiation condition at infinity. The expansion (3.2) is referred to as exterior or h-expansion. The solution can be expressed close to the center z_b by the interior or j-expansion

$$\Phi(x-z_b) = \sum_{l=0}^{\infty} \sum_{m=-l}^{l} N_{lm} j_l\left(\kappa|x-z_b|\right) Y_l^m\left(\frac{x-z_b}{|x-z_b|}\right), \tag{3.3}$$

where $j_l^{(1)}(\cdot)$ are the spherical Bessel functions. The translation of the coefficients F_{lm} of the far-field representation to the coefficients N_{lm} of the near-field representation is the key to an efficient multipole method.

3.2 Multipole expansion for the fundamental solution of the Helmholtz equation

The series expansions (3.2) and (3.3) are not yet usable in an efficient numerical scheme, since each N_{lm} depends on all F_{lm} when translating the coefficients. This convolution implies a quadratic numerical cost in the number of series terms which is too expensive for practical computations. Rokhlin (1993) develops a diagonal form of the translation operators that allows the translation of each coefficient independently of the others. Starting point for the derivation of the diagonal form is Gegenbauer's addition theorem (Abramowitz and Stegun, 1974) that allows the combination of (3.2) and (3.3) in a more compact form. The fundamental solution of the Helmholtz equation is expressed as a function of the vectors $d = x - z_b + z_a - y$ and $D = z_b - z_a$.

$$\begin{aligned}\frac{\mathrm{e}^{\mathrm{i}\kappa|x-y|}}{|x-y|} = \frac{\mathrm{e}^{\mathrm{i}\kappa|D+d|}}{|D+d|} &= 4\pi\mathrm{i}\kappa \sum_{l=0}^{\infty}\sum_{m=-l}^{l} (-1)^l\, j_l(\kappa|d|)\, h_l^{(1)}(\kappa|D|)\, Y_l^{m*}(\hat{D}) Y_l^m(\hat{d}) \\ &= \mathrm{i}\kappa \sum_{l=0}^{\infty} (2l+1)(-1)^l j_l(\kappa|d|)\, h_l^{(1)}(\kappa|D|)\, P_l(\hat{D}\cdot\hat{d}), \quad |D| > |d|\,. \end{aligned} \tag{3.4}$$

$j_l(\cdot)$ again denotes spherical Bessel functions, $h_l(\cdot)$ Hankel functions and $P_l(\cdot)$ the Legendre polynomials. Normalized vectors are indicated by $\hat{(\cdot)} = (\cdot)/|\cdot|$.

The separation of D and d succeeds by using the orthonormality of the Legendre polynomials on the unit sphere $\mathbb{S}^2$ and the expansion of spherical waves. Using

$$4\pi\mathrm{i}^l j_l(\kappa|d|) P_l(\hat{D}\cdot\hat{d}) = \int_{\mathbb{S}^2} \mathrm{e}^{\mathrm{i}\kappa d\cdot s} P_l(s\cdot\hat{D})\,\mathrm{d}s\,, \tag{3.5}$$

one obtains a diagonal form of the multipole expansion

$$\frac{\mathrm{e}^{\mathrm{i}\kappa|D+d|}}{|D+d|} = \frac{\mathrm{i}\kappa}{4\pi}\sum_{l=0}^{\infty}(2l+1)\mathrm{i}^l h_l^{(1)}(\kappa|D|) \int_{\mathbb{S}^2} \mathrm{e}^{\mathrm{i}\kappa d\cdot s} P_l(s\cdot\hat{D})\,\mathrm{d}s\,. \tag{3.6}$$

In a numerical implementation, the sum over l is truncated at $l = L$. The choice of L depends on the required precision of the multipole expansion and other parameters that are discussed in Section 3.5. It must be pointed out that L cannot be chosen arbitrarily large, since the series diverges for $l \to \infty$.

The integration on the unit sphere $\mathbb{S}^2$ is approximated by Gauss point quadrature with discrete values of the far field directions s. According to Rokhlin (1993) the integral of a function $f(s)$ on the unit sphere is evaluated by the quadrature rule

$$\int_{\mathbb{S}^2} f(s)\,\mathrm{d}s = \sum_{i=0}^{2p-1}\sum_{j=0}^{p-1} \omega_j \frac{\pi}{p} f(s_{i,j})\,, \tag{3.7}$$

with $s_{i,j} = (\cos\varphi_i \cos\theta_j, \sin\varphi_i \sin\theta_j, \cos\theta_j)^{\mathrm{T}}$ and $\varphi_i = (i\pi)/p$, $\cos\theta_j = x_j$. x_j and ω_j are abscissae and weights of the p point Gauss-Legendre rule, respectively. The error committed by the numerical quadrature must be restricted depending on the expansion length L. Rahola (1996) shows that the choice $p = L$, i.e. $2L^2$ quadrature points, is suitable.

For the truncated series, summation $l = 0, \ldots, L$ and integration can be interchanged and one defines the diagonal translation operators M_L

$$M_L(s, D) = \sum_{l=0}^{L} (2l+1)\mathrm{i}^l h_l^{(1)}(\kappa|D|) P_l(s \cdot \hat{D}) \,. \tag{3.8}$$

For the actual implementation of the multipole scheme, the vector d is decomposed to the original contributions $x_b - z_b$ and $z_a - y_a$. Using the translation operators M_L, the wave function at a point x_b induced by sources q_a ($a = 1, \ldots, A$) at y_a inside the sphere around z_a can be computed as

$$\Phi(x_b) = \frac{\mathrm{i}\kappa}{4\pi} \int_{\mathbb{S}^2} \mathrm{e}^{\mathrm{i}\kappa(x_b - z_b)\cdot s} M_L(s, z_b - z_a) \sum_{a=1}^{A} \mathrm{e}^{\mathrm{i}\kappa(z_a - y_a)\cdot s} q_a \, \mathrm{d}s \,. \tag{3.9}$$

The field of the sources q_a is represented in z_b by the translation operators $M_L(s, z_b - z_a)$ and translated to the field point x_b close to z_b by simple multiplication with $e^{\mathrm{i}\kappa(x_b - z_b)\cdot s}$. The translation operators do not depend on the location of the single sources, but only on the distance vector between the expansion centers of the clusters. Thus, leading to favorable numerical complexity for the FMM BEM as discussed in Section 3.7.

For simplicity of later references, the far-field signature $F(s)$ and near-field signature $N(s)$ are defined as follows

$$F(s) = \sum_{a=1}^{A} \mathrm{e}^{\mathrm{i}\kappa(z_a - y_a)\cdot s} q_a \,, \tag{3.10}$$

$$N(s) = M_L(s, z_b - z_a) F(s) \,. \tag{3.11}$$

3.3 Multilevel multipole algorithm

When adapting the multipole scheme to the BEM, a source refers to an integration point of a boundary element. To take advantage of the fast evaluation of the fundamental solution by the translation operators M_L, it is required to cluster the boundary elements in groups. This can either be done on one level resulting in a

single-level computational scheme or, as in the present algorithm, on several levels of clusters resulting in a multi-level scheme. A hierarchic tree with levels $\ell = 0, \ldots, \ell_{\max}$ containing clusters of elements is introduced. The first cluster on the highest level $\ell = 0$ is a parallelepiped containing all elements. Child clusters are created by bisection of the parent cluster's parallelepiped and elements as a whole are assigned to a child. Clusters that contain no elements are deleted from the cluster tree. The clusters are split until the number of elements in the respective cluster falls below a set maximum. As a consequence, the cluster tree has a variable depth and is adapted to refinement of the boundary element mesh.

In contrast to many publications on multipole algorithms where oct-trees (one cluster is split into eight child clusters) are employed, binary trees (one cluster is split into two child clusters) are chosen for the level hierarchy. This approach yields a higher efficiency for domains where the original parallelepiped does not represent a cube as often encountered in practical applications. Both methods—binary and oct trees—use regular dissection of the clusters, i.e. the distance of cluster centers D is equal for many pairs. This offers the advantage that translation operators—that depend only on the distance D—can be reused, saving considerably computing time and memory requirements when setting up the multipole BEM.

Due to the variable depth of the cluster tree, the final leaves—the "lowest level" of the cluster tree—are found on different levels ℓ. As illustration, the lowest level of a cluster tree for a two-dimensional boundary element discretization is shown in Fig. 3.2. The clusters are denoted by C_ℓ^γ where $1 \leq \gamma \leq 2^\ell$ and the center of each element that controls the cluster affiliation is represented by a dot in the figure. The original rectangular root cluster is split until at most three elements are located in each cluster on the lowest level. For the numerical examples in Section 3.8, the three-dimensional cluster tree is refined until at most 12 triangular elements are located in each cluster.

Attributes of a cluster are its center z_ℓ^γ and diameter d_ℓ^γ which is the maximum distance between two boundary element nodes in the cluster C_ℓ^γ. The cluster diameter d_ℓ on level ℓ is chosen as the largest of the cluster diameters d_ℓ^γ. Furthermore, a cluster possesses a list of clusters in the near-field and clusters in the interaction set. The clusters in the near-field (N) are all those clusters whose distance D between their centers fulfills the condition

$$D < c\frac{d_\ell}{2}\,, \tag{3.12}$$

where c is a suitable constant. The choice $c \geq 3$ guarantees a near-field buffer of at least one cluster. For the definition of the near-field relations on the lowest level of the cluster tree, each pair of leaves is checked for the near-field condition (3.12) with

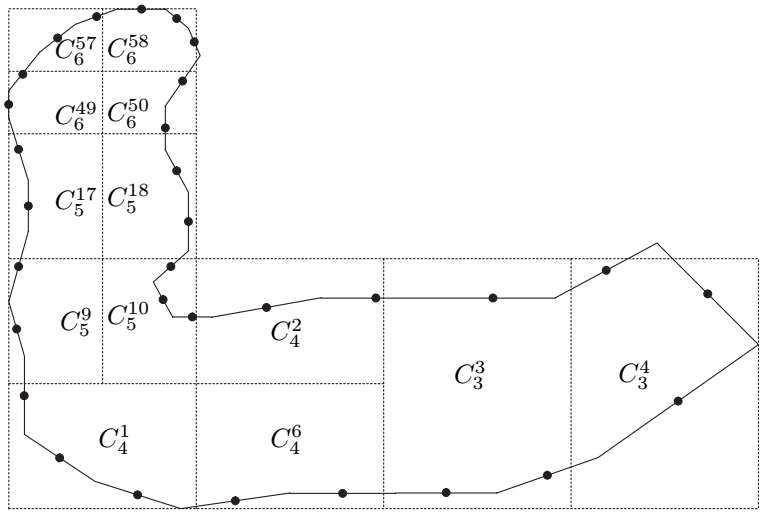

Figure 3.2: Two-dimensional boundary element discretization with lowest level of cluster tree.

the larger of the two cluster diameters to preserve the symmetry of the multipole algorithm. For boundary element models with a varying element size as e.g. in Fig. 3.2, this procedure yields varying near-field diameters. However, the increased efficiency of the adaptive multipole algorithm makes up for the increased memory requirements.

Clusters, whose parent clusters fulfill the near-field condition, but themselves are not in each others near-field, form the interaction list (I). The information transfer in the multilevel scheme is displayed in Fig. 3.3. The contribution of a source in the hatched cluster on the lowest level is distributed in the multilevel multipole algorithm by the following steps:

(i) Compute the far-field signature on the lowest level.

(ii) Translate the far-field signature to the interaction list.

(iii) Shift the far-field signature to the center of the parent cluster.

(iv) Repeat the last two steps upwards until the interaction list is empty.

(v) In the downward pass, shift the near-field signatures to the child clusters.

(vi) Recover solution and evaluate near-field on the lowest level.

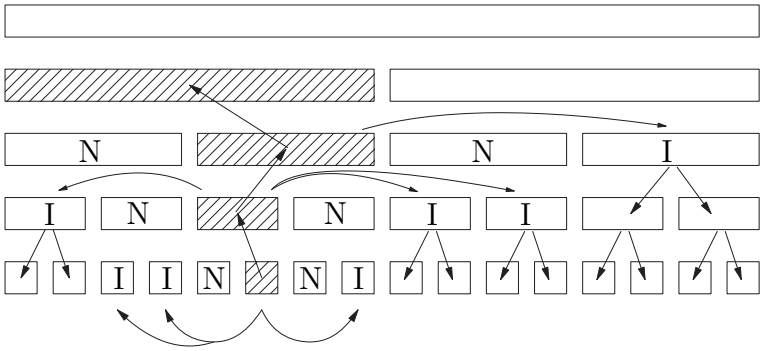

Figure 3.3: Information transfer in cluster tree.

3.4 Evaluation of boundary integral operators

The FMM BEM algorithm does not assemble the complete BEM matrices, but performs a fast evaluation of the matrix-vector products. That allows the solution using an iterative solver for the linear system of equations as discussed in Chapter 4. In the following sections, the FMM evaluation for the matrix-vector products of the discrete single layer potential and the hyper-singular operator is discussed. The single layer potential is evaluated for constant shape functions, the hyper-singular operator for linear shape functions. The transfer of the FMM to the other boundary integral operators of the symmetric Galerkin BEM and the Burton-Miller approach is straight forward.

Single layer potential

The multipole algorithm is formulated for the ν-th component of the matrix-vector product $v_\nu = (\mathbf{Vu})_\nu$ of the single layer potential evaluated for constant shape functions. For convenience, μ and ν are used as indices for the element vectors as well as to denote the elements μ and ν, respectively. The near-field part of the boundary integral operator is evaluated directly—i.e. the matrix entries are computed and stored when field and load point are close to each other—whereas for the far-field part, the multipole method is applied. The double surface integral is substituted by

Gauss quadrature on the elements

$$v_\nu = (\mathbf{V}_{\text{nearfield}}\mathbf{u})_\nu + \int_\nu \sum_{\mu\in\text{farfield}} u_\mu \int_\mu P^*(x,y)\,\mathrm{d}s_y\,\mathrm{d}s_x$$
$$\approx (\mathbf{V}_{\text{nearfield}}\mathbf{u})_\nu + \sum_{j=1}^{G_\nu}\omega_{\nu,j}\Delta_\nu \sum_{\mu\in\text{farfield}} u_\mu \sum_{i=1}^{G_\mu}\omega_{\mu,i}\Delta_\mu P^*(x_{\nu,j},y_{\mu,i})\,, \quad (3.13)$$

where Δ_μ, $\omega_{\mu,i}$, and $y_{\mu,i}$ are the Jacobi determinant, Gauss weight, and integration point for element μ, respectively. The terms are defined analogous for the element ν. The expression

$$\Phi(x_{\nu,j}) = \sum_{\mu\in\text{farfield}} u_\mu \sum_{i=1}^{G_\mu}\omega_{\mu,i}\Delta_\mu P^*(x_{\nu,j},y_{\mu,i}) \quad (3.14)$$

can be evaluated efficiently using the multipole method, whereas the remaining operations in (3.13) are local at element ν. The multipole algorithm consists of the following steps:

(i) Compute the far-field signature $F_\ell^\gamma(s)$ for all clusters on the lowest level

$$F_\ell^\gamma(s) = \sum_{\mu\in C_\ell^\gamma} u_\mu\Delta_\mu \sum_{i=1}^{G_\mu}\omega_{\mu,i}\,\mathrm{e}^{\mathrm{i}\kappa(y_{\mu,i}-z_\ell^\gamma)\cdot s}\,. \quad (3.15)$$

(ii) Translate $F_\ell^\gamma(s)$ to the interaction list using the translation operators M_L

$$N_\ell^\gamma(s) = \sum_{\text{interaction list}} M_L(s,D)\;F_\ell^\gamma(s)\,, \quad (3.16)$$

where D is the distance between z_ℓ^γ and the center of the respective interaction list cluster.

(iii) Shift $F_\ell^\gamma(s)$ to the center of the parent cluster.

(iv) Repeat last two steps upwards until the interaction list is empty.

(v) In the downward pass, shift the near-field signatures $N_\ell^\gamma(s)$ in interaction lists to the child clusters.

(vi) On the lowest level, recover solution in the integration points $x_{\nu,j}$

$$\Phi(x_{\nu,j}) = \frac{\mathrm{i}\kappa}{4\pi}\int_{\mathbb{S}^2}\mathrm{e}^{\mathrm{i}\kappa(z_\ell^\gamma-x_{\nu,j})\cdot s}N_\ell^\gamma(s)\,\mathrm{d}s\,. \quad (3.17)$$

Finally, the matrix-vector product (3.13) is evaluated by summation of the element contributions $\Phi(x_{\nu,j})$ and addition of the near-field contribution which is calculated directly using the standard BEM.

Hyper-singular operator

Similarly to the single layer potential, the multipole algorithm is formulated for the τ-th component of the matrix-vector product $v_\tau = (\mathbf{Du})_\tau$ of the hyper-singular operator evaluated for linear shape functions. For convenience, σ and τ are used as indices of the nodal vectors as well as to denote the nodes σ and τ, respectively. In the near-field, regularization techniques must be employed to compute the hyper-singular operator. However, in the far-field, i.e. in the multipole share, the direct computation proves more efficient since it requires only one call of the multipole algorithm. Even better for the Burton-Miller approach, where the direct evaluation of the hyper-singular operator and the double layer potential can be performed simultaneously except for the recovering of the solution. In contrast, a multipole evaluation of the regularized hyper-singular operator according to (2.18) would require six calls of the multipole algorithm with different source strengths. The reduced number of multipole cycles when combining regularization in the near-field and direct evaluation in the far-field makes up for the special attention that must be paid to the cluster edges and near-field edges as presented in Appendix B.

For the linear shape functions, $\varphi^p_\tau|_\nu(x)$ denotes the nodal basis function of node τ constricted to the element ν. The set $\mathcal{E}(\tau)$ contains all elements attached to node τ, whereas $\mathcal{N}(\nu)$ contains all incident nodes of element ν. Using these expressions the matrix-vector product for the hyper-singular operator is expressed as

$$\begin{aligned} v_\tau &= (\mathbf{D}_{\text{nearfield}}\mathbf{u})_\tau + \\ &\quad \sum_{\nu\in\mathcal{E}(\tau)} \int_\nu \sum_{\mu\in\text{farfield}} \sum_{\sigma\in\mathcal{N}(\mu)} u_\sigma \int_\mu \varphi^p_\tau|_\nu(x)\ \varphi^p_\sigma|_\mu(y)\ \frac{\partial^2 P^*(x,y)}{\partial n_x \partial n_y}\ \mathrm{d}s_y\,\mathrm{d}s_x \\ &\approx (\mathbf{D}_{\text{nearfield}}\mathbf{u})_\tau + \sum_{\nu\in\mathcal{E}(\tau)} \sum_{j=1}^{G_\nu} \omega_{\nu,j}\Delta_\nu\varphi^p_\tau|_\nu(x_{\nu,j})\ n_{x_{\nu,j}}\cdot\nabla_{x_{\nu,j}} \\ &\quad \left\{ \sum_{\mu\in\text{farfield}} \sum_{\sigma\in\mathcal{N}(\mu)} u_\sigma \sum_{i=1}^{G_\mu} \omega_{\mu,i}\Delta_\mu\varphi^p_\sigma|_\mu(y_{\mu,i})\ n_{y_{\mu,i}}\cdot\nabla_{y_{\mu,i}}\ P^*(x_{\nu,j},y_{\mu,i}) \right\}. \end{aligned} \tag{3.18}$$

As for the single layer potential, the expression in curly brackets can be evaluated efficiently using the multipole method, whereas the remaining operations in (3.18) are local at node τ. The multipole algorithm for the hyper-singular operator consists of the following steps:

(i) Compute the far-field signature $F'^{\gamma}_\ell(s)$ for all clusters on the lowest level. The normal derivative at the source point must be considered when computing the

far-field signature. Thus, Eq. (3.10) is replaced by its normal derivative

$$F_\ell^{'\gamma}(s) = \mathrm{i}\kappa \sum_{\mu \in C_\ell^\gamma} \sum_{\sigma \in \mathcal{N}(\mu)} u_\sigma \sum_{i=1}^{G_\mu} \omega_{\mu,i} \Delta_\mu \varphi_\sigma^p|_\mu(y_{\mu,i})\; n_{y_{\mu,i}} \cdot s\; \mathrm{e}^{\mathrm{i}\kappa(y_{\mu,i} - z_\ell^\gamma)\cdot s}\,. \quad (3.19)$$

(ii) Translate $F_\ell^{'\gamma}(s)$ to the interaction list using the translation operators M_L

$$N_\ell^{'\gamma}(s) = \sum_{\text{interaction list}} M_L(s, D)\; F_\ell^{'\gamma}(s)\,, \quad (3.20)$$

where D is the distance between z_ℓ^γ and the center of the respective interaction list cluster.

(iii) Shift $F_\ell^{'\gamma}(s)$ to the center of the parent cluster.

(iv) Repeat last two steps upwards until the interaction list is empty.

(v) In the downward pass, shift the near-field signatures $N_\ell^{'\gamma}(s)$ in interaction lists to the child clusters.

(vi) On the lowest level, the normal derivative is evaluated when recovering the solution in the integration points $x_{\nu,j}$

$$n_{x_{\nu,j}} \cdot \nabla_{x_{\nu,j}} \Phi'(x_{\nu,j}) = \frac{\kappa^2}{4\pi} \int_{\mathbb{S}^2} n_{x_{\nu,j}} \cdot s\; \mathrm{e}^{\mathrm{i}\kappa(z_\ell^\gamma - x_{\nu,j})\cdot s} N_\ell^{'\gamma}(s)\, \mathrm{d}s\,. \quad (3.21)$$

Finally, the matrix-vector product (3.18) is evaluated by summation of the element contributions $n_{x_{\nu,j}} \cdot \nabla_{x_{\nu,j}} \Phi'(x_{\nu,j})$ and addition of the near-field contribution which is calculated directly using the standard BEM.

3.5 Truncation error

Convergence of the truncated multipole expansion

$$\mathrm{i}\kappa \sum_{l=0}^{L} (2l+1)\, j_l(\kappa|d|)\, h_l^{(1)}(\kappa|D|)\, P_l(\hat{D}\cdot\hat{d}) \quad (3.22)$$

to the partial wave equation is guaranteed for an expansion length of $L > \kappa|d|$. However, the exact choice of the expansion length L is crucial for the multipole algorithm: L must chosen large enough to yield the required accuracy and short enough for a favorable computing cost. Increasing the expansion length, a problem

arises besides the increased computing cost, since the Hankel function $h_l^{(1)}(\kappa|D|)$ grows to infinity for large l. For exact arithmetic, this growth is balanced out by the decay of $j_l(\kappa|d|)\, P_l(\hat{D}\cdot\hat{d})$ which is not true for a numerical implementation due to the machine precision.

When truncating the multipole expansion of the fundamental solution (3.4) at $l = L$, the truncation error is defined by

$$\epsilon^L = \mathrm{i}\kappa \sum_{l=L+1}^{\infty} (2l+1)\, j_l(\kappa|d|)\, h_l^{(1)}(\kappa|D|)\, P_l(\hat{D}\cdot\hat{d}). \tag{3.23}$$

The classical error analysis for the multipole expansion is motivated by the convergence behavior of the spherical Bessel functions $j_l(\kappa|d|)$. Following the extensive presentation in the paper by Koc et al. (1999), its derivation is briefly discussed. The Legendre polynomials in the error representation (3.23) take their maximum value of one for collinear vectors $\hat{D}$ and $\hat{d}$. Using the large-argument asymptotic form of the Hankel functions for $\kappa|D| \to \infty$, i.e. a sufficiently large near-field, the error can then be approximated

$$|\epsilon^L| \leq \frac{\mathrm{i}\kappa}{\kappa|D|} \sum_{l=L+1}^{\infty} (2l+1)\, |j_l(\kappa|d|)|\,. \tag{3.24}$$

For the spherical Bessel functions, the ascending series expansion

$$j_l(\kappa|d|) = \frac{(\kappa|d|)^l}{1\cdot 3\cdot 5\,...\,(2l+1)} \left\{ 1 - \frac{\frac{1}{2}(\kappa|d|)^2}{1!(2l+3)} + \frac{(\frac{1}{2}(\kappa|d|)^2)^2}{2!(2l+3)(2l+5)} - \;... \right\} \tag{3.25}$$

holds (Abramowitz and Stegun, 1974) which is used to obtain the error bound

$$|\epsilon^L| \leq \frac{\mathrm{i}\kappa}{\kappa|D|} \frac{(\kappa|d|)^{L+1}}{1\cdot 3\cdot 5\,...\,(2L+1)}\,. \tag{3.26}$$

According to (3.26), the truncation error decreases faster than exponential as the expansion length is increased. A drawback of this estimate is that it is only valid when L is large compared to $\kappa|d|$ whereas in practical applications $\kappa|d| \approx L$. Furthermore, (3.26) does not take into account the behavior of the Hankel function $h_l^{(1)}(\kappa|D|)$. A detailed discussion of this aspect is given in the papers by Koc et al. (1999) and Ohnuki and Chew (2003).

A different approach for the error analysis is taken by Darve (2000). Darve shows that the truncation error ϵ^L is bounded by $\bar{\epsilon}$, for the choice

$$L = C_1 + C_2\kappa|d| + C_2' \log(\kappa|d|) + C_3 \log\frac{1}{\bar{\epsilon}}\,, \tag{3.27}$$

where the constants are independent of the distance $\kappa|D|$.

In the presented algorithm, the expansion length is chosen according to the well-established semi-empirical rule that is used by Coifman et al. (1993), Gyure and Stalzer (1998), Schneider (2003b), and many others. The rule is based on the estimate (3.26) and gives the expansion length L depending on the cluster diameter d_ℓ and the wavenumber κ

$$L(\kappa d_\ell) = \kappa d_\ell + p \log(\kappa d_\ell + \pi) \,, \tag{3.28}$$

where p specifies the required precision. The parameter p does not translate directly to the number of accurate digits, since the effects of $\kappa|D|$ are not considered. This influence will be discussed at hand of the numerical examples.

3.6 Interpolation and filtering of the multipole expansion

Since the expansion length depends on the cluster diameter, it changes from level to level. In the upward-cycle the far-field signatures $F(s)$ are shifted to the center of the parent clusters. To retain the accuracy of the expansion for the larger cluster, further terms must be added to the series expansion. Increasing the expansion length for the diagonal form of the multipole expansion means adding far-field directions s on the unit-sphere, from there the name—interpolation. However, correct interpolation can only be performed on the original multipole expansion (3.4), thus, the interpolation algorithm consists of the following steps:

(i) Transform the far-field signature to the original multipole expansion.

(ii) Add zeros for the required expansion length.

(iii) Compute the far-field signature for the new far-field directions.

In the downward-cycle, filtering is defined equivalently. The near-field signatures are transformed to the original expansion, redundant terms for the new cluster diameter are cut, and the new near-field signatures are computed.

A proper handling of interpolating and filtering is mandatory for an efficient implementation of the fast multipole algorithm for the Helmholtz equation. An algorithm based on fast Fourier transforms (FFT) is proposed by Gyure and Stalzer (1998) which is adapted to the current scheme. So far, the transform from the multipole

expansion to the far-field signature and its inverse have not been given explicitly. According to Rokhlin (1993), the pair of far-field transforms is defined by

$$F(s) = \sum_{l=0}^{L} \sum_{m=-l}^{l} \mathrm{i}^l Y_l^m(s) F_{lm} \,, \tag{3.29}$$

$$F_{lm} = \int_{\mathbb{S}^2} \mathrm{i}^{-l} Y_l^{m*}(s) F(s) \,\mathrm{d}s \,, \tag{3.30}$$

where $(\cdot)^*$ denotes the complex conjugate. Using the definition of the normalized Legendre polynomials $\hat{P}_l^{|m|}(\cos\theta)$

$$Y_l^m(s) = \hat{P}_l^{|m|}(\cos\theta)\mathrm{e}^{\mathrm{i}m\varphi} \,, \tag{3.31}$$

the spherical harmonics transform is rewritten

$$\begin{aligned} F_{lm} &= \int_{\mathbb{S}^2} \mathrm{i}^{-l} Y_l^{m*}(s) F(s) \,\mathrm{d}s \\ &= \int_{\theta} \mathrm{i}^{-l} \hat{P}_l^{|m|}(\cos\theta) \left(\int_{\varphi} \mathrm{e}^{-\mathrm{i}m\varphi} F(s) \,\mathrm{d}\varphi \right) \mathrm{d}(\cos\theta) \\ &= \int_{\theta} \mathrm{i}^{-l} \hat{P}_l^{|m|}(\cos\theta) \Phi_m(\cos\theta) \,\mathrm{d}(\cos\theta) \,. \end{aligned} \tag{3.32}$$

The coefficients $\Phi_m(\cos\theta)$ can be efficiently evaluated using the fast Fourier transform. It is recalled that the far-field signature is represented at the equally spaced sampling points $\varphi_i = (i\pi)/L$, $i = 0, \ldots, 2L-1$ and the inner integral in (3.32) can be replaced by

$$\Phi_m(\cos\theta) = \frac{1}{2L} \sum_{i=0}^{2L-1} F(s)\mathrm{e}^{-\mathrm{i}m\varphi_i} = \frac{1}{2L} \sum_{i=0}^{2L-1} F(s)\mathrm{e}^{\frac{-2\pi\mathrm{i}mi}{2L}} \,, \tag{3.33}$$

which has clearly the form of a discrete Fourier transform and, thus, all coefficients $\Phi_m(\cos\theta)$ can be computed by a FFT with a numerical cost of $\mathcal{O}(L\log L)$ if $2L = 2^n$. The outer integration in (3.32) is evaluated using numerical quadrature

$$F_{lm} = \sum_{j=0}^{L-1} \omega_j \mathrm{i}^{-l} \hat{P}_l^{|m|}(x_j) \Phi_m(x_j) \,, \tag{3.34}$$

where x_j and ω_j are sampling points and integration weights of the L point Gauss quadrature rule, respectively. The result are the multipole coefficients of the h-expansion. In this form the series expansion can be extended to the new required expansion length L' by adding $F_{lm} = 0$ for $L < l \leq L'$. The new coefficients of the far-field signature are then computed as

$$F(s') = \sum_{m=-L'}^{L'} \mathrm{i}^l \mathrm{e}^{\mathrm{i}m\varphi(s')} \sum_{l=0}^{L'} F_{lm} \hat{P}_l^{|m|}\left(\cos\theta(s')\right) \,. \tag{3.35}$$

3.7 Estimate of the numerical complexity

For the estimate of the numerical complexity, a cluster tree with branches of equal depth is assumed, i.e. the adaptive clustering as described in Section 3.3 is neglected. The goal of the multilevel multipole scheme is to achieve a numerical complexity of $\mathcal{O}(N \log^2 N)$ in the number of unknowns. Thus, on the lowest level $\ell_{\max}$, the number of elements in the near-field of each cluster can be proportional to $\log^2 N$. This results in $n_{\ell_{\max}} \sim N/\log^2 N$ clusters with diameter $d_{\ell_{\max}} \sim \log N/\sqrt{N}$. On the higher levels, number and diameter of the clusters behave as $n_\ell \sim n_{\ell_{\max}} 4^{\frac{\ell-\ell_{\max}}{3}}$ and $d_\ell \sim d_{\ell_{\max}}/2^{\frac{\ell-\ell_{\max}}{3}}$, respectively. The total number of levels is clearly of the order $\mathcal{O}(\log N)$.

Due to the dependence on the wavenumber, the computational cost of the FMM is discussed for keeping the ratio $\kappa h \sim \kappa/\sqrt{N}$ constant. This situation corresponds to the engineering rule of thumb that a constant number of elements per wavelength results in a constant discretization error. Choosing the expansion length according to (3.28) and assuming $\kappa/\sqrt{N} = \text{const}$ yields the following estimates:

- On the lowest level of the cluster tree, the sources are combined to the far-field signature of the clusters using (3.10). The numerical complexity is $\mathcal{O}(N L_{\ell_{\max}}^2) = \mathcal{O}(N(\kappa d_{\ell_{\max}})^2) = \mathcal{O}(N \log^2 N)$, as each element has to be considered in each of the $2L_{\ell_{\max}}^2$ discrete far-field directions.
- Transformation of far-field signature of each cluster to its interaction list by applying the translation operators M_L.
  $\mathcal{O}(L_\ell^2 n_\ell \log N) = \mathcal{O}((\kappa d_\ell)^2 n_\ell \log N) = \mathcal{O}(\kappa^2 \log N) = \mathcal{O}(N \log N)\,.$
- Translation of the far-field signature to the center of the parent cluster, interpolation if necessary.
  $\mathcal{O}(L_\ell^2 \log L_\ell n_\ell \log N) = \mathcal{O}(N \log^2 N)$
- In the downward cycle, translation and filtering of the near-field signatures.
  $\mathcal{O}(L_\ell^2 \log L_\ell n_\ell \log N) = \mathcal{O}(N \log^2 N)$
- On the lowest level, translation of the near-field signature to each quadrature point and recovering the solution.
  $\mathcal{O}(N L_{\ell_{\max}}^2) = \mathcal{O}(N \log^2 N)$.
- The near-field of a cluster contains at most $\mathcal{O}(\log^2 N)$ elements, so that the evaluation of all near-field entries scales as $\mathcal{O}(N \log^2 N)$.

The FMM algorithm accomplishes the targeted numerical complexity of $\mathcal{O}(N \log^2 N)$ for computations on refined meshes for increasing frequencies.

3.8 Numerical examples

The focus of the presented examples in this section is to demonstrate the accuracy and the favorable numerical complexity of the multipole BEM matrix-vector product. The model problems used in the examples are defined in Section 2.4.

Accuracy of multipole matrix-vector product

First, the accuracy of the truncated multipole expansion is studied. As an example, the matrix-vector product of the Burton-Miller approach (2.22)

$$\mathbf{v} = \left(-\frac{1}{2}\mathbf{I} + \mathbf{K} + \frac{\mathrm{i}}{\kappa}\mathbf{D}\right)\mathbf{1} \tag{3.36}$$

is evaluated on the L16 model for the vector $\mathbf{1}$ containing ones in each coordinate. It is recalled that two parameters must be chosen in the multipole algorithm: the near-field size parameter c according to (3.12) as well as the expansion length parameter p according to (3.28). The sensitivity of the error of the multipole matrix-vector product on these two parameters is plotted in Fig. 3.4. Thereby, the error of the matrix-vector product e_2^{MV} is defined as

$$e_2^{\mathrm{MV}} = \frac{\|\mathbf{v}_{\mathrm{multipole}} - \mathbf{v}_{\mathrm{BEM}}\|_2}{\|\mathbf{v}_{\mathrm{BEM}}\|_2}, \tag{3.37}$$

and relates the result of the multipole matrix-vector product to the matrix-vector product of the full BEM matrix. Both plots in Fig. 3.4, for 300 Hz and 600 Hz,

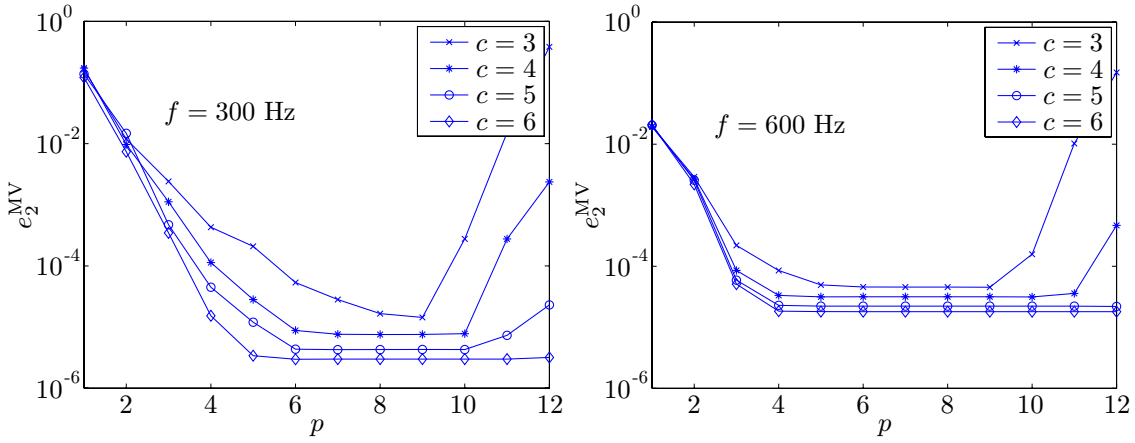

Figure 3.4: Error of multipole matrix-vector product on L16 model plotted against the expansion length parameter p.

show the same behavior. The error e_2^{MV} decreases exponentially with the increase of the expansion length as predicted by (3.26) until the smallest achievable error is obtained. The value of this limit is influenced by factors that are not directly linked to the multipole algorithm. Most dominant in the presented case is the evaluation of the hyper-singular operator by direct evaluation in the far-field for the multipole method whereas it is completely evaluated using the regularization technique for the standard BEM (see Appendix B). Increasing the expansion length further, the error tends to diverge due to the behavior of the Hankel functions for a large expansion length. The influence of the near-field size is negligible for engineering precisions of a few per cent. The smallest possible near-field parameter $c = 3$ that guarantees a one box near-field buffer yields good results. The situation is different when high accuracies are required: the convergence with increasing expansion length is faster for larger near-fields.

The same behavior is found for the brake disk model. In Fig. 3.5 the sensitivity of the error of the matrix-vector product e_2^{MV} is plotted as described before. For the real-life model, too, the small near-field and a very short expansion length yield a sufficient precision for engineering applications.

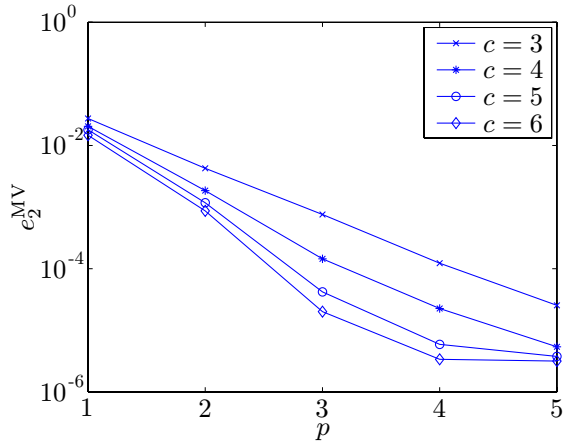

Figure 3.5: Error of multipole matrix-vector product for brake disk model.

Summarizing the results, the choice of the near-field parameter $c = 3$ and the expansion length parameter $p = 2$ is recommended for engineering simulations. This combination is found to yield reliably an error of the matrix-vector product of around 1 % which is sufficient for most applications. So the multipole algorithm can be used as a black-box tool in a software package. The user does not need to choose any parameters in addition to those of a standard BEM simulation. For higher precisions, the suitable choice of near-field and expansion length parameter

can have significant impact on the efficiency of the multipole BEM computation.

Computing cost of multipole matrix-vector product

The critical aspect of computing cost to achieve a required precision is discussed next. The computing time for the matrix-vector product on the L16 model is plotted in Fig. 3.6 against the error e_2^{MV} for the near-field parameters $c = 3$ and $c = 4$ at frequencies of $f = 300$ Hz and $f = 600$ Hz. As expected, the computing time increases logarithmic with the achieved precision over a wide range. Only for very high precisions a deviation from the logarithmic behavior is noticed. The findings support the prediction that fast multipole BEM simulations require a quasi-linear numerical cost.

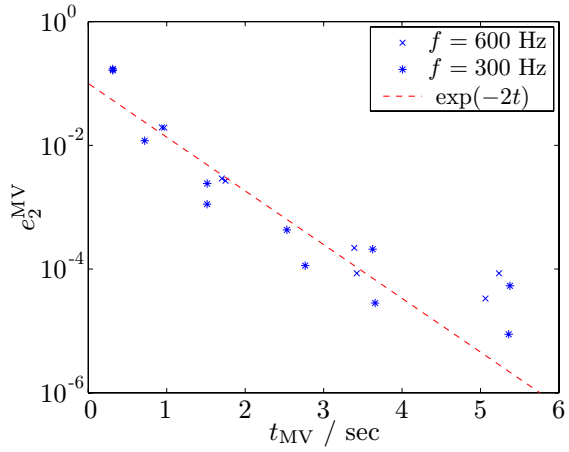

Figure 3.6: Error of multipole matrix-vector product plotted against computing time t_{MV} on L16 model.

The results of BEM simulations on refined meshes for the L-shape at a frequency of $f = 600$ Hz are documented in Tab. 3.1. The near-field size is set to $c = 4$, whereas the expansion length is varied. The computations are performed on the models L8, L16, L32, and L64 with a characteristic element size $h = 0.125, \ldots, 0.016$ m what corresponds to simulations with 5 to 36 elements per wavelength. Neumann boundary conditions are applied corresponding to a monopole source inside the L-shape and the Burton-Miller BEM system is solved with a residual of 10^{-5} using un-preconditioned GMRES. The total simulation error e_2^{Γ} (see (2.23)) consists of the discretization and integration errors of the BEM model, the multipole truncation error, and the true residual error of the solver. For BEM simulations of Neumann boundary value problems, one can expect an h^2 convergence of the Dirichlet bound-

ary datum in the L2 norm. The results in Tab. 3.1 match this convergence rate, and for the chosen example a minimal total error of below 10^{-3} confirms the correct implementation of the BEM package.

Table 3.1: Computing time for simulations on L-shape at $f = 600$ Hz.

	p	$t_{\text{near-field}}$	iterations	t_{MV}/iteration	error e_2^Γ
L8	1	38 sec	28	0.5 sec	$6.36 \cdot 10^{-2}$
	2	38 sec	28	0.8 sec	$6.20 \cdot 10^{-2}$
	3	38 sec	28	1.5 sec	$6.20 \cdot 10^{-2}$
L16	1	162 sec	35	1.0 sec	$2.27 \cdot 10^{-2}$
	2	162 sec	35	1.8 sec	$1.42 \cdot 10^{-2}$
	3	162 sec	35	3.4 sec	$1.42 \cdot 10^{-2}$
L32	2	620 sec	51	4.1 sec	$8.51 \cdot 10^{-3}$
	3	620 sec	51	7.8 sec	$3.76 \cdot 10^{-3}$
	4	620 sec	51	13.6 sec	$3.63 \cdot 10^{-3}$
L64	3	2470 sec	83	19.2 sec	$6.62 \cdot 10^{-3}$
	4	2470 sec	83	30.7 sec	$1.37 \cdot 10^{-3}$
	5	2470 sec	83	49.2 sec	$0.98 \cdot 10^{-3}$

The computing time on the refined meshes increases quasi-linearly as predicted. The number of unknowns increases by a factor of four between the meshes, as does the computing time $t_{\text{near-field}}$ for the calculation of the near-field matrix entries as well as the time t_{MV} required for the evaluation of one matrix-vector product. The number of required iterations for the solution of the system of equations increases with mesh refinement. Up to 83 iterations for the L64 model are required what represents a significant numerical cost and calls for efficient solvers and preconditioning that are discussed in Chapter 4.

For engineering acoustics simulations, usually the factor κh is kept constant to obtain an approximately consistent accuracy for increasing frequencies. Typically six to ten elements are chosen to yield an discretization error of a few per cent. In Tab. 3.2 the results of simulations on the models L8 to L96 are listed. The frequency increases from 300 Hz to 3600 Hz corresponding to nine elements per wavelength on each model. The multipole parameters are set $c = 3$ and $p = 2$ to account for the expected error of around 1%. The computing time for the near-field matrices $t_{\text{near-field}}$ increases quasi-linearly as before, the computing time for the setup of the translation operators increases sub-linearly since many operators can be reused in the regular

cluster tree. The residual for the solution with un-preconditioned GMRES is set to 10^{-5}. One notices that the number of required iterations for the solution does not increase with mesh refinement and increasing frequency which is due to the choice of the coupling parameter in the Burton-Miller approach. Thus, the total simulation time t_{total} does increase quasi-linearly with the number of unknowns as predicted for the multipole BEM.

Table 3.2: Computing time for simulations on L-shape at $\kappa h = \text{const}$.

	f	$t_{\text{near-field}}$	t_{setup}	iterations	t_{solve}	t_{total}	error e_2^{Γ}
L8	300 Hz	31 sec	0.3 sec	37	11 sec	0.7 min	$2.19 \cdot 10^{-2}$
L16	600 Hz	125 sec	1.6 sec	35	62 sec	3 min	$1.44 \cdot 10^{-2}$
L32	1200 Hz	444 sec	11 sec	34	325 sec	13 min	$1.22 \cdot 10^{-2}$
L64	2400 Hz	1743 sec	33 sec	36	1892 sec	61 min	$1.13 \cdot 10^{-2}$
L96	3600 Hz	5163 sec	95 sec	45	5152 sec	174 min	$1.24 \cdot 10^{-2}$

The computing time t_{total} as documented in Tab. 3.2 is plotted in Fig. 3.7 against the number of unknowns of the BEM models to underline the quasi-linear behavior. In the second graph, the memory requirement is plotted against the number of unknowns. The memory requirement increases even slower than linear which is due to the reuse of translation operators in the regular cluster tree. For comparison, the computing cost of the standard BEM simulations (see Tab. 2.2) is plotted, too. For models with more than a few thousand unknowns, one obtains a significant advantage using the fast multipole BEM. The simulations are performed faster and at a much reduced memory requirement.

The advantage of fast multipole BEM against standard BEM simulations is also pointed out in Tab. 3.3 on the example of the brake disk model. For the solution of the model with 4422 unknowns at a frequency of 3720 Hz, 108 GMRES iterations are required for a residual of 10^{-4}. The computation of the full BEM matrices takes 49 min. Using the multipole BEM with very coarse parameters, the solution is obtained in 16 min which is a significant speed-up for the rather small model. The error e_2^{BD} for the brake disk model is defined as

$$e_2^{\text{BD}} = \frac{\|\mathbf{p}_{\text{multipole}} - \mathbf{p}_{\text{BEM}}\|_2}{\|\mathbf{p}_{\text{BEM}}\|_2} \,. \tag{3.38}$$

For the coarse multipole parameters one obtains an error of the solution $e_2^{\text{BD}} = 3.0\%$ in reference to the standard BEM solution. For an increased expansion length, the multipole error is 0.2% at a computing time of just 19 min which is half of the computing time required for the standard BEM.

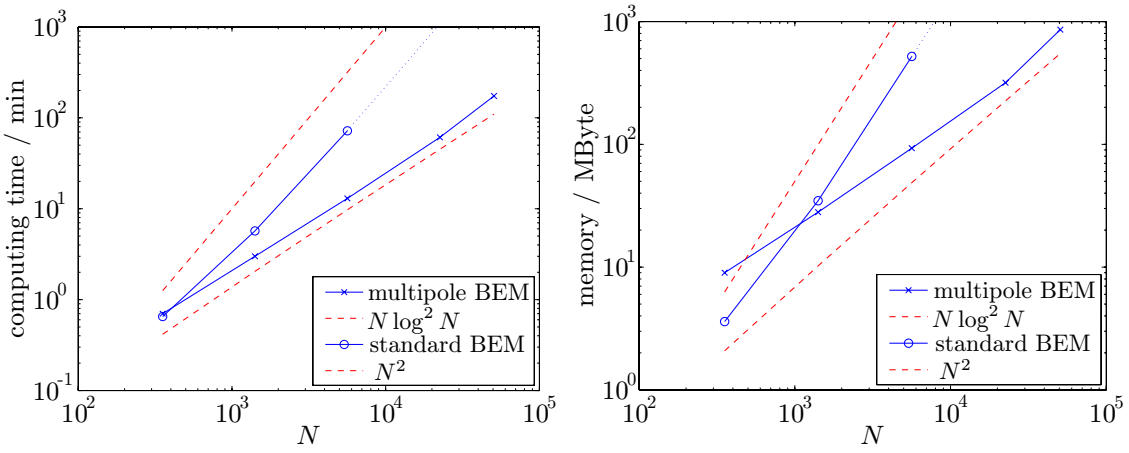

Figure 3.7: Computing time and memory requirement plotted against number of unknowns N for computations at $\kappa h = \text{const}$.

Table 3.3: Multipole BEM simulations on brake disk model.

c	p	$t_{\text{near-field}}$	t_{setup}	t_{solve}	t_{total}	error
BEM		49 min	–	29 sec	50 min	ref
3	1	13 min	12 sec	3 min	16 min	$3.04 \cdot 10^{-2}$
	2	13 min	18 sec	6 min	19 min	$2.33 \cdot 10^{-3}$
	3	13 min	37 sec	12 min	26 min	$7.59 \cdot 10^{-4}$
4	1	18 min	53 sec	3 min	22 min	$2.04 \cdot 10^{-2}$
	2	18 min	74 sec	7 min	26 min	$1.17 \cdot 10^{-3}$
	3	18 min	77 sec	13 min	32 min	$1.44 \cdot 10^{-4}$
5	1	24 min	94 sec	3 min	28 min	$1.79 \cdot 10^{-2}$
	2	24 min	115 sec	7 min	33 min	$1.17 \cdot 10^{-3}$
	3	24 min	164 sec	13 min	40 min	$1.36 \cdot 10^{-4}$

Chapter 4

Iterative solution of BEM systems

The solution of boundary element systems poses several difficulties: the matrices are typically fully populated, non-hermitian, and in acoustics mostly indefinite. The direct solution of the BEM system

$$\mathbf{A}\mathbf{x} = \mathbf{b} \tag{4.1}$$

is not feasible for large matrices $\mathbf{A}$, since it scales as $\mathcal{O}(N^3)$ in the number of unknowns. Furthermore, using the fast multipole BEM as discussed in the previous chapter, $\mathbf{A}$ is not set up explicitly and thus not available for an LU decomposition.

Instead of solving the BEM system (4.1) directly, it can be rewritten in residual form

$$\mathbf{x} = \mathbf{x}_k + \mathbf{A}^{-1}\mathbf{r}_k \ , \tag{4.2}$$

where $\mathbf{x}_k$ is an approximation of the exact solution $\mathbf{x}$ and $\mathbf{r}_k = \mathbf{b} - \mathbf{A}\mathbf{x}_k$ is the residual. Computing the inverse of the system matrix $\mathbf{A}^{-1}$ clearly is not feasible. If one replaces $\mathbf{A}^{-1}$ by the inverse of a preconditioning matrix $\mathbf{M}^{-1}$, one obtains an iterative scheme

$$\mathbf{x}_{k+1} = \mathbf{x}_k + \mathbf{M}^{-1}\mathbf{r}_k \, . \tag{4.3}$$

There are two aspects for a good choice of $\mathbf{M}^{-1}$: first, its application on a vector should be inexpensive and second, it should be a good approximation of $\mathbf{A}^{-1}$. The simplest choice $\mathbf{M}^{-1}_{\text{Jacobi}} = [\text{diag}(\mathbf{A})]^{-1}$ represents the Jacobi iteration. A better approximation of $\mathbf{A}^{-1}$ is found by the approximate inverse approach presented in Section 4.2. Unfortunately, simple iterations like (4.3) converge very poorly or not at all for typical BEM systems. However, they can be used as preconditioners for Krylov subspace methods or as smoothers for multigrid methods.

4.1 Krylov subspace methods

Krylov subspace methods are iterative techniques that extract the approximate solution from a subspace $\mathcal{K}_k(\mathbf{A}, \mathbf{r}_0)$

$$\mathcal{K}_k(\mathbf{A}, \mathbf{r}_0) = \text{span}\left\{\mathbf{r}_0, \mathbf{A}\mathbf{r}_0, \mathbf{A}^2\mathbf{r}_0, \ldots, \mathbf{A}^{k-1}\mathbf{r}_0\right\} . \tag{4.4}$$

The obvious choice of basis vectors as in (4.4) is not suitable for an efficient numerical scheme, since for increasing powers of the matrix $\mathbf{A}$, they get more and more collinear. The construction of an adequate Krylov basis and the way of extracting the approximate solution are two distinct aspects of the various Krylov subspace methods. For an extensive introduction, it is referred to the text books by Saad (2003) and van der Vorst (2003).

Krylov subspace methods are the most suitable black-box iterative solvers for BEM systems currently available. Their performance is systematically examined in the paper by Marburg and Schneider (2003b). The authors compare the restarted bi-conjugate gradient stabilized algorithm (BICGSTAB), the conjugate gradient method applied to the normal equations (CGNR), the generalized minimal residual method (GMRES), and the transpose free quasi minimal residual method (TFQMR) for interior acoustic problems as well as for exterior problems using the Burton-Miller approach. The efficiency of the solvers is found to depend on the wave number and the smoothness of the surface of the BEM model. GMRES works very efficiently for most of the examples presented by Marburg and Schneider (2003b) and—even more important—GMRES proves to be the most robust of the compared methods. Ochmann et al. (2003) as well propose a variant of GMRES for BEM simulations in acoustics. Thus, in the following, the discussion is concentrated on GMRES which is implemented according to the algorithm presented in the templates for the solution of linear systems (Barrett et al., 1994).

GMRES is based on Arnoldi's procedure for building an orthogonal basis for the Krylov subspace $\mathcal{K}_k(\mathbf{A}, \mathbf{r}_0)$. Each Arnoldi vector $\mathbf{v}_j$ $(j = 2, \ldots, k)$ is built by multiplying $\mathbf{v}_{j-1}$ with $\mathbf{A}$ and performing a standard Gram-Schmidt orthogonalization against all previous Arnoldi vectors $\mathbf{v}_1, \mathbf{v}_2, \ldots, \mathbf{v}_{j-1}$. The Arnoldi algorithm yields the $(k+1) \times k$ Hessenberg matrix $\mathbf{H}_k$ for which holds the relation

$$\mathbf{A}\mathbf{V}_k = \mathbf{V}_{k+1}\mathbf{H}_k , \tag{4.5}$$

with $\mathbf{V}_k = (\mathbf{v}_1, \mathbf{v}_2, \ldots, \mathbf{v}_k)$. The Arnoldi Krylov basis is used in the GMRES algorithm to compute the iterate $\mathbf{x}_k$ as

$$\mathbf{x}_k = \mathbf{x}_0 + \mathbf{V}_k\mathbf{y} , \tag{4.6}$$

where the coefficients $\mathbf{y}$ are determined to minimize the residual

$$\mathbf{b} - \mathbf{A}\mathbf{x}_k = \mathbf{b} - \mathbf{A}(\mathbf{x}_0 + \mathbf{V}_k\mathbf{y}) = \mathbf{V}_{k+1}\left(\beta\mathbf{e}_1 - \mathbf{H}_k\mathbf{y}\right) , \tag{4.7}$$

with $\beta = ||\mathbf{r}_0||_2$ and the starting vector for the Arnoldi algorithm $\mathbf{v}_1 = \mathbf{r}_0/\beta$. Since the column vectors of $\mathbf{V}_{k+1}$ are orthonormal, minimizing the residual (4.7) is equivalent to the least squares problem of finding the minimum of $||\beta\mathbf{e}_1 - \mathbf{H}_k\mathbf{y}||_2$ which is solved by subsequently applying plane rotations $\mathbf{Q}_k$ to transform the upper Hessenberg matrix $\mathbf{H}_k$ into the upper triangular form $\mathbf{R}_k$. Applying the rotation, the coefficients $\mathbf{y}$ can be computed as

$$\mathbf{y} = \mathbf{R}_k^{-1}\mathbf{Q}_k^{\mathrm{T}}(\beta\mathbf{e}_1) . \tag{4.8}$$

As a big advantage, this procedure allows to monitor the residual at each iteration step without actually computing the approximate solution $\mathbf{x}_k$. It can be shown that for exact arithmetic the last entry of the vector $\mathbf{Q}_k^{\mathrm{T}}(\beta\mathbf{e}_1) = (\gamma_1, \gamma_2, \ldots, \gamma_{k+1})^{\mathrm{T}}$ corresponds to the residual of the approximate solution $\mathbf{x}_k$

$$||\mathbf{b} - \mathbf{A}\mathbf{x}_k||_2 = |\gamma_{k+1}| . \tag{4.9}$$

When using the multipole BEM, the matix-vector product is evaluated commiting a truncation error e_2^{MV}. Equation (4.9) is only valid as long $e_2^{\mathrm{MV}} < |\gamma_{k+1}|$, otherwise there is a residual gap between the true residual $||\mathbf{b} - \mathbf{A}\mathbf{x}_k||_2$ and the residual $|\gamma_{k+1}|$ computed in the GMRES algorithm. A more detailed discusssion of the residual gap is given in Section 5.3 for the solution of saddle point formulations arising from structural-acoustic interaction problems.

The computing cost for generating the Krylov basis (4.4) in the GMRES algorithm increases significantly when a high number of iterations is required. Usually, restarts are employed to restrict the size of the Krylov basis: the solution after n steps is used as new initial guess for the next n-step GMRES. However, for acoustic BEM simulations, the convergence of GMRES can deteriorate quickly when restarts are used. Thus, throughout the thesis, GMRES is employed without restarts. It is noted that in contrast to very sparse systems of equations, arising for example from FEM, the evaluation of the matrix-vector products represents the dominating computing cost in BEM simulations, not so much storing and orthogonalizing the Krylov basis. Nevertheless, preconditioning of the BEM system to reduce the number of required iterations is essential for an efficient solution.

4.2 Approximate inverse preconditioner

A popular approach for the preconditioning of FEM systems is incomplete LU decomposition (ILU). ILU can be applied successfully to BEM systems for acoustics as shown by Schneider and Marburg (2003). However, ILU is also known to often show poor performance for indefinite and highly non-symmetric systems—typical properties of the BEM systems. An alternative is the direct approximation of the inverse of the system matrix (Saad, 2003). The application of the approximate inverse approach to BEM systems for acoustics is presented by Chen and Harris (2001). The basic idea of their approach is operator splitting. The integral operator A is divided into a bounded contribution A_0 and the remaining $\tilde{A}$

$$A = A_0 + \tilde{A}\,. \tag{4.10}$$

It can be shown that the eigenvalues of $A_0^{-1}A = I + A_0^{-1}\tilde{A}$ cluster around one which yields an improved convergence of the iterative solver.

The application of the operator splitting on the boundary integral operators is straight forward. For the double layer potential, the boundary integral is partitioned

$$(Kp)(x) = \int_{\Gamma_0} \frac{\partial P^*(x,y)}{\partial n_y}\, p(y)\,\mathrm{d}s_y + \int_{\tilde{\Gamma}} \frac{\partial P^*(x,y)}{\partial n_y}\, p(y)\,\mathrm{d}s_y\,, \tag{4.11}$$

where $\Gamma = \Gamma_0 \cup \tilde{\Gamma}$, defining K_0 and $\tilde{K}$, respectively. For the hyper-singular operator, the procedure is equivalent and the Burton-Miller operator is set up according to (2.19). Γ_0 is chosen locally as an element layer around the load point under consideration. As an example a two-element layer is depicted in Fig. 4.1. The operator A_0 is sparse, however, the exact application of A_0^{-1} would still be too expensive. Thus, an approximate inverse of A_0 is computed.

The computation of the preconditioner matrix $\mathbf{M}_{\mathrm{AI}}^{-1}$ is demonstrated on the $N \times N$ system matrix $\mathbf{A}$ which stems from the discretization of A using linear nodal basis functions $\boldsymbol{\varphi}^p$. The choice of Γ_0 defines the sparsity pattern s_j of the preconditioner. For every load point corresponding to the index j, $s_j = \{j_1, j_2, \ldots, j_n\}$ contains all nodes within the chosen element layer. By this definition, Γ_0 is extended to the support of the basis functions $\varphi^p_{s_j}$. For the ordering of s_j, it is assumed that $j_1 = j$. The preconditioner matrix is now looked for in the space of $N \times N$ matrices $\mathcal{G}_s$ with the same sparsity pattern as defined by $s_1, s_2, \ldots, s_N$. The right preconditioner matrix $\mathbf{M}_{\mathrm{AI}}^{-1} = (\mathbf{m}_1, \mathbf{m}_2, \ldots, \mathbf{m}_N)$ is found by the solution of the least squares problem

$$\min_{\mathbf{M}_{\mathrm{AI}}^{-1} \in \mathcal{G}_s} ||\mathbf{A}\mathbf{M}_{\mathrm{AI}}^{-1} - \mathbf{I}||^2 = \sum_{j=1}^{N} \min_{\mathbf{m}_j \in \mathcal{G}_{s_j}} ||\mathbf{A}\mathbf{m}_j - \mathbf{e}_j||_2^2\,, \tag{4.12}$$

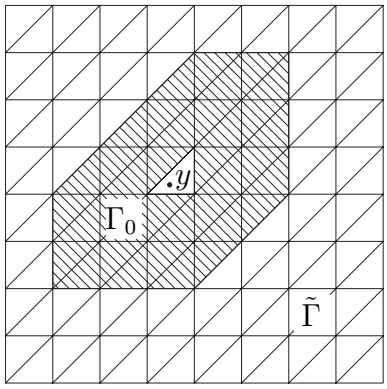

Figure 4.1: Two-element layer around load point.

where $\mathcal{G}_{s_j}$ contains all vectors that have entries specified by s_j. The computation of the approximate inverse involves the solution of N least squares problems. Chen (2001) proves that solving the least squares problem

$$\begin{pmatrix} a_{1j_1} & a_{1j_2} & \cdots & a_{1j_n} \\ \vdots & \vdots & \vdots & \vdots \\ a_{j_1j_1} & a_{j_1j_2} & \cdots & a_{j_1j_n} \\ a_{j_2j_1} & a_{j_2j_2} & \cdots & a_{j_2j_n} \\ \vdots & \vdots & \vdots & \vdots \\ a_{j_nj_1} & a_{j_nj_2} & \cdots & a_{j_nj_n} \\ \vdots & \vdots & \vdots & \vdots \\ a_{Nj_1} & a_{Nj_2} & \cdots & a_{Nj_n} \end{pmatrix} \begin{pmatrix} m_{jj_1} \\ m_{jj_2} \\ \vdots \\ m_{jj_n} \end{pmatrix} = \begin{pmatrix} 1 \\ 0 \\ \vdots \\ 0 \end{pmatrix} \tag{4.13}$$

is equivalent in a least squares sense to solving the system

$$\begin{pmatrix} a_{j_1j_1} & a_{j_1j_2} & \cdots & a_{j_1j_n} \\ a_{j_2j_1} & a_{j_2j_2} & \cdots & a_{j_2j_n} \\ \vdots & \vdots & \ddots & \vdots \\ a_{j_nj_1} & a_{j_nj_2} & \cdots & a_{j_nj_n} \end{pmatrix} \begin{pmatrix} m_{jj_1} \\ m_{jj_2} \\ \vdots \\ m_{jj_n} \end{pmatrix} = \begin{pmatrix} 1 \\ 0 \\ \vdots \\ 0 \end{pmatrix} . \tag{4.14}$$

The solution vectors $\mathbf{m}_j = (0, \cdots, m_{jj_1}, m_{jj_2}, \ldots, m_{jj_n}, \cdots, 0)^{\mathrm{T}}$ of the N systems of equations (4.14) set up the preconditioner matrix $\mathbf{M}_{\mathrm{AI}}^{-1}$. For approximate inverse preconditioning of GMRES, the system (4.1) is simply replaced by

$$\mathbf{A}\mathbf{M}_{\mathrm{AI}}^{-1}\tilde{\mathbf{x}} = \mathbf{b}\,, \qquad \mathbf{x} = \mathbf{M}_{\mathrm{AI}}^{-1}\tilde{\mathbf{x}}\,. \tag{4.15}$$

In the implementation of GMRES, the new variable $\tilde{\mathbf{x}}$ is never invoked explicitly. The corrections of the initial guess are approximated in the Krylov subspace $\mathcal{K}^k(\mathbf{A}\mathbf{M}_{\mathrm{AI}}^{-1}, \mathbf{r}^0)$ and simply multiplied by $\mathbf{M}_{\mathrm{AI}}^{-1}$ when composing the solution.

The choice of the size of Γ_0 is a trade-off between effect and numerical cost of the preconditioner. The convergence rates of the approximate inverse preconditioned GMRES for a one-element and a two-element layer around the element containing the load point are depicted in Fig. 4.2 for the simulation of the L16 model at 600 Hz. For comparison the convergence rate of un-preconditioned GMRES is plotted, too. One notices the improved convergence of the approximate inverse preconditioned

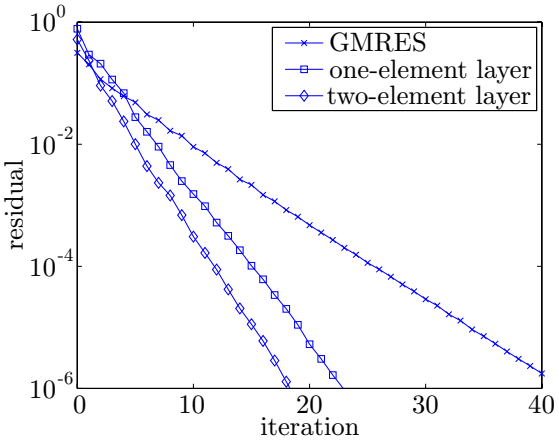

Figure 4.2: Convergence of GMRES with approximate inverse preconditioning.

GMRES. The one- and two-element layer approach show a similar performance with a small advantage of the two-element layer. The additional computing cost for the preconditioning is negligible for large BEM models. A larger choice of Γ_0 is not feasible in combination with the multipole BEM, since not enough matrix entries are available when choosing a small near-field size. A two-element layer is thus employed throughout the numerical examples in Section 4.4.

4.3 Multigrid solver

As an alternative to GMRES, multigrid solvers can be used for the solution of the BEM systems. Ochmann and Wellner (1991) and Tröndle (1995) discussed the application of multigrid solvers to BEM for acoustics very early. However, the number of unknowns is limited when using standard BEM and the advantages of the multigrid solvers do not pay off. The situation is different when using a fast BEM which allows some hundreds of thousands unknowns. However, one constraint remains: geometric multigrids require a hierarchy of discretizations—the coarse grids—which is typically difficult to construct in engineering applications. Algebraic multigrids as proposed by Langer et al. (2003) resolve this problem but are beyond the scope

of the thesis.

A detailed introduction to multigrid methods can be found in the books by Hackbusch (1985) and Briggs et al. (2000). Following their presentations, a short overview on the algorithm is given. Multigrid solvers are based on the property of classical iteration schemes (Jacobi, SOR, ...) to quickly reduce the high-frequency part of the residual ("smoothing"). For the low-frequency part, the classical schemes show a very poor convergence behavior. The idea of the multigrid solvers is to treat this share by a coarse grid correction. A multigrid cycle for the approximate solution $\mathbf{x}_k^{(l)}$ on level l at the iteration step k includes the following steps:

(i) $\nu_1^{(l)}$ presmoothing iterations

$$\mathbf{x}_{k,1}^{(l)} = \mathcal{S}^{\nu_1^{(l)}} \mathbf{x}_k^{(l)} \,, \tag{4.16}$$

(ii) computation of the residual

$$\mathbf{r}^{(l)} = \mathbf{b}^{(l)} - \mathbf{A}^{(l)} \mathbf{x}_{k,1}^{(l)} \,, \tag{4.17}$$

(iii) restriction of the residuum to the grid $l-1$

$$\mathbf{b}^{(l-1)} = \mathbf{R}_{(l)}^{(l-1)} \mathbf{r}^{(l)} \,, \tag{4.18}$$

(iv) computation of the coarse grid correction

$$\mathbf{A}^{(l-1)} \mathbf{y}^{(l-1)} = \mathbf{b}^{(l-1)} \,, \tag{4.19}$$

- (4.19) is solved directly on the lowest level $l-1=0$
- for higher levels, an approximation of $\mathbf{y}^{(l-1)}$ is computed by executing multigrid cycles

(v) prolongation of the coarse grid correction

$$\mathbf{x}_{k,2}^{(l)} = \mathbf{x}_{k,1}^{(l)} + \mathbf{P}_{(l-1)}^{(l)} \mathbf{y}^{(l-1)} \,, \tag{4.20}$$

(vi) $\nu_2^{(l)}$ postsmoothing iterations

$$\mathbf{x}_{k+1}^{(l)} = \mathcal{S}^{\nu_2^{(l)}} \mathbf{x}_{k,2}^{(l)} \,. \tag{4.21}$$

This cycle is repeated until convergence is attained. If in step (iv) the multigrid algorithm is recursively accessed once at each level, one obtains a V-cycle multigrid scheme as depicted in Fig. 4.3. The grids are traversed once from the finest grid to the coarsest grid and back in each multigrid iteration.

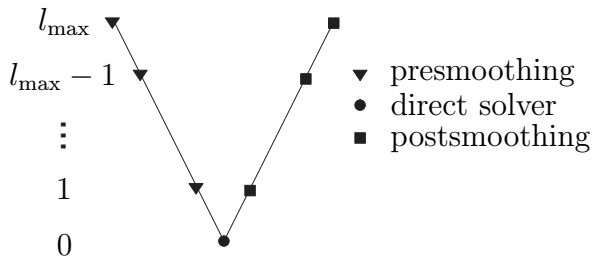

Figure 4.3: V-cycle multigrid scheme.

4.3.1 Restriction and prolongation operators

For setting up the restriction matrices $\mathbf{R}_{(l)}^{(l-1)}$ from grid l to $l-1$ and the prolongation matrices $\mathbf{P}_{(l-1)}^{(l)}$ from grid $l-1$ to l various definitions exist. In the presented algorithm, the standard choice for linear nodal basis functions on the boundary triangulation is employed as it is commonly used in 2-D FEM. The prolongation matrix corresponds to the discretized identity mapping. For mesh refinement as depicted in Fig. 4.4, the prolongation matrix can be given explicitly

$$\begin{pmatrix} x_1^{(l)} \\ x_2^{(l)} \\ x_3^{(l)} \\ x_4^{(l)} \\ x_5^{(l)} \\ x_6^{(l)} \\ x_7^{(l)} \\ x_8^{(l)} \\ x_9^{(l)} \end{pmatrix} = \underbrace{\begin{pmatrix} 1 & 0 & 0 & 0 \\ 0 & 1 & 0 & 0 \\ 0 & 0 & 1 & 0 \\ 0 & 0 & 0 & 1 \\ 0.5 & 0.5 & 0 & 0 \\ 0 & 0.5 & 0.5 & 0 \\ 0 & 0 & 0.5 & 0.5 \\ 0.5 & 0 & 0 & 0.5 \\ 0.5 & 0 & 0.5 & 0 \end{pmatrix}}_{\mathbf{P}_{l-1}^{l}} \begin{pmatrix} x_1^{(l-1)} \\ x_2^{(l-1)} \\ x_3^{(l-1)} \\ x_4^{(l-1)} \end{pmatrix} . \tag{4.22}$$

The restriction matrix is then chosen as the transpose of the prolongation matrix, $\mathbf{R}_{(l)}^{(l-1)} = \left(\mathbf{P}_{(l-1)}^{(l)}\right)^{\mathrm{T}}$. It is noted that this definition of the restriction and prolongation operators would allow Galerkin assembling of the system matrices on the lower levels

$$\mathbf{A}^{(l-1)} = \mathbf{R}_{(l)}^{(l-1)} \mathbf{A}^{(l)} \mathbf{P}_{(l-1)}^{(l)} . \tag{4.23}$$

However, in the current implementation, the BEM is set up on every level independently, since the system matrix is not available explicitly when using the multipole BEM.

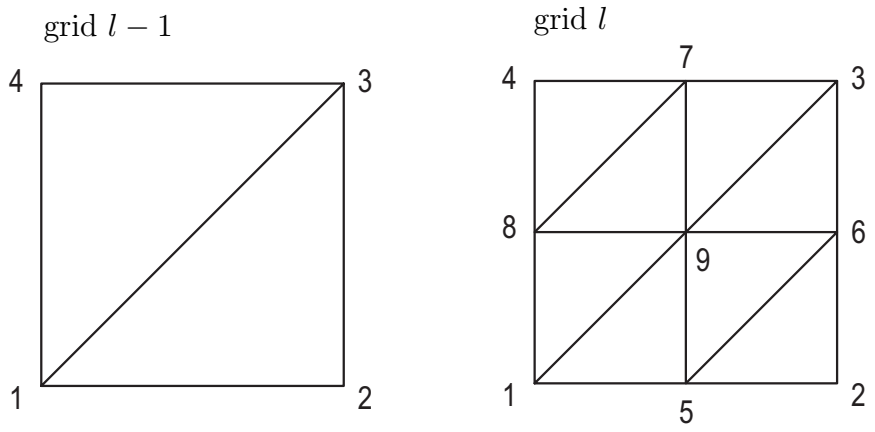

Figure 4.4: Mesh hierarchy of boundary triangulation.

4.3.2 Smoothing scheme

The design of suitable smoothers $\mathcal{S}$ is essential for an efficient multigrid solver. When applying the multigrid solver to acoustics, usually the oscillation of the solution cannot be resolved on the coarser grids. Brandt and Livshits (1997) propose a wave-ray scheme to eliminate this term and show that convergence results can be obtained that are similar to multigrids for elliptic problems. The implementation of the wave-ray method is very involved, a simpler approach that is used in the presented thesis is proposed by Elman et al. (2001). They employ standard smoothers on the fine grids and GMRES iterations as smoothers on the coarser grids.

A common choice for the smoothers in multigrid solvers are damped Jacobi relaxations, defined as

$$\mathcal{S}\mathbf{x}_k^{(l)} := \mathbf{x}_k^{(l)} + \eta \mathbf{M}_{\text{Jacobi}}^{-1} \left(\mathbf{b}^{(l)} - \mathbf{A}^{(l)} \mathbf{x}_k^{(l)} \right) , \tag{4.24}$$

where the damping factor $\eta < 1$ can be tuned for good convergence. The popular damped Gauss-Seidel relaxation cannot be applied to the multipole BEM, since the matrix-vector product $\mathbf{A}^{(l)}\mathbf{x}_k^{(l)}$ is evaluated in one step in the multipole algorithm.

The smoothing effect of damped Jacobi relaxations is demonstrated in Fig. 4.5. The relaxations are applied to the Burton-Miller BEM for the L16 model at 600 Hz. The start vector $\mathbf{x}_0$ is chosen to yield a random distribution of the initial residual. One notices clearly that the Jacobi iterations quickly smoothen the residual. On the other hand, the value of the residual increases, i.e. the Jacobi scheme diverges and cannot be used as a stand-alone solver without the coarse grid correction.

Standard relaxed Jacobi smoothers are found to work inefficiently for BEM in acous-

initial residual

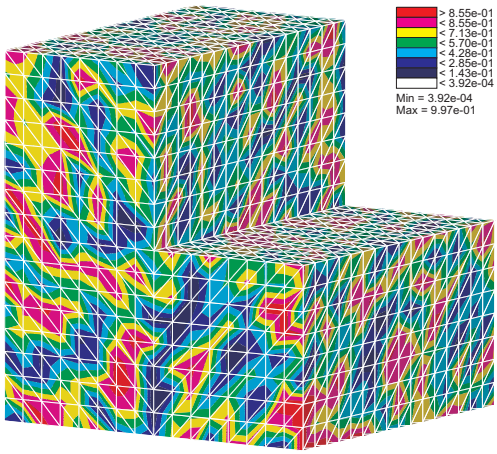

after 1st Jacobi step

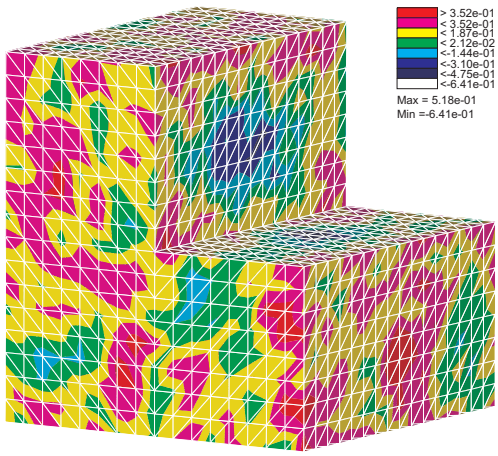

after 2nd Jacobi step

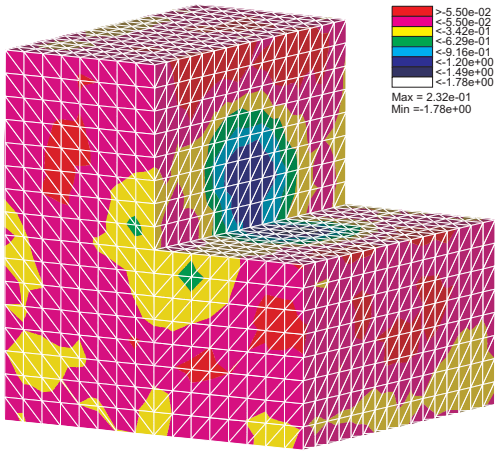

after 3rd Jacobi step

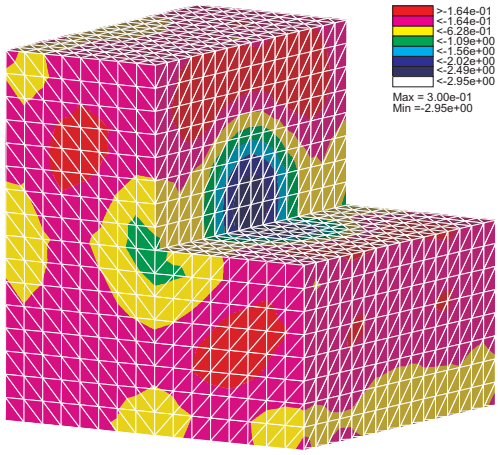

Figure 4.5: Smoothing by relaxed Jacobi iterations.

tics. The approximate inverse preconditioner presented in Section 4.2 proves to be a more efficient smoother. It is defined as

$$\mathcal{S}\mathbf{x}_k^{(l)} := \mathbf{x}_k^{(l)} + \mathbf{M}_{\mathrm{AI}}^{-1}\left(\mathbf{b}^{(l)} - \mathbf{A}^{(l)}\mathbf{x}_k^{(l)}\right) . \tag{4.25}$$

The approximate inverse smoother and—to some extent—the Jacobi smoother work reasonably well for the Helmholtz equation if the grid is fine enough. For coarse grids, the simple relaxation schemes amplify low-frequency modes inadmissibly. Elman et al. (2001) show that using GMRES iterations as smoother on coarse grids accelerates the solver even if the grids are so coarse that the oscillation of the solution cannot be reproduced. They propose to set the limit at $h^{(l)}\kappa = 0.5$. The engineering rule of thumb of simulations with six to ten elements per wavelength corresponds to a factor of $h^{(l_{\max})}\kappa = 1 \ldots 0.6$ on the finest grid. That means that for applica-

tions with "high" engineering accuracies, cheap standard smoothers can be used on the finest grid, whereas GMRES must be used on all coarser grids. The number of required GMRES iterations is rather high, typically up to 30 iterations on the finest GMRES grid. When using the standard BEM, this smoothing scheme proves efficient, since for each grid refinement the numerical cost per iteration increases by a factor of 16. However, when using the fast multipole BEM, the numerical cost per iteration increases only by a factor of four. Thus, the smoothing scheme must be designed to require only a moderate increase of iterations on the coarser grids.

The following choice of parameters for the multigrid algorithm yields good results for engineering application when used in combination with the multipole BEM: Jacobi or approximate inverse smoothing steps are performed on the two finest levels. On the finest grid, $\nu^{(l_{\max})} = 1$ smoothing step is applied. On the second grid $\nu^{(l_{\max}-1)} = 2 \dots 4$ smoothing steps are applied in agreement with the reduced numerical cost. For the coarser grids, $\nu_1^{(l)} = 1$ GMRES presmoothing and $\nu_2^{(l)} = 7$ postsmoothing steps are used.

4.4 Comparison of preconditioned GMRES and multigrid solver

The family of BEM meshes for the L-shape (Tab. 2.1) is used for the comparison of the preconditioned GMRES method and the multigrid solver. First, the convergence behavior of the solvers is studied on the BEM discretization L16 at a frequency $f = 600$ Hz. In Fig. 4.6, a 3-grid solver with Jacobi smoothing on the two finest levels is examined. On the finest grid $\nu^{(l_{\max})} = 1$ smoothing iteration is used, on the second grid the number of smoothing steps is varied $\nu^{(l_{\max}-1)} = 2 \dots 4$. As expected, the convergence improves with the increase of smoothing steps. The gain obtained by the fourth smoothing step is rather small, thus, $\nu^{(l_{\max}-1)} = 3$ is fixed for the following studies. The choice of the damping factor η turns out critical: e.g. a residual of 10^{-5} is obtained after 17 and 8 iterations for $\eta = 0.7$ and $\eta = 0.5$, respectively. This strong influence of parameters is a major limitation for the practical application of the multigrid solver with Jacobi smoother. The performance of the Jacobi multigrid is rather disappointing, even with well tuned parameters $\eta = 0.7$ and $\nu^{(l_{\max}-1)} = 3$. In Fig. 4.6 the convergence of the Jacobi multigrid (MG Jacobi) is compared to the approximate inverse multigrid (MG AI) and the solution with GMRES. Smoothing with the approximate inverse approach performs far superior to the Jacobi smoothers. GMRES is also accelerated significantly by the approximate inverse preconditioning. The preconditioned GMRES requires only

few iterations more than the Jacobi multigrid and is much cheaper per iteration.

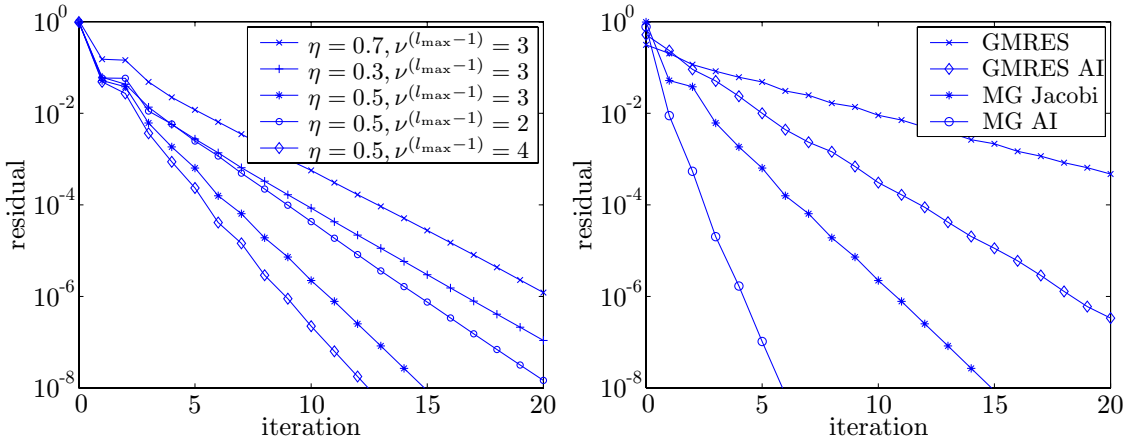

Figure 4.6: Convergence of multigrid and GMRES solvers.

Both, GMRES and multigrid solver in combination with approximate inverse preconditioning show little influence of the frequency for simulations on the same BEM discretization. The achieved residual after 20 and 5 iterations, respectively, is plotted in Fig. 4.7 for 300 Hz $< f <$ 600 Hz, the frequency range where the model L16 would be typically used in engineering applications. The residual stays in the range $10^{-5} - 10^{-6}$ and there is no sign of instabilities at critical frequencies.

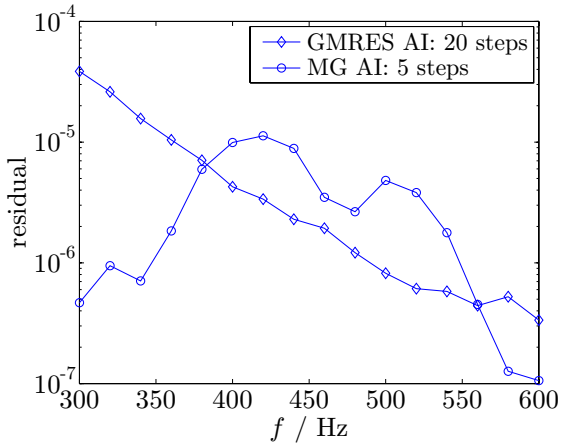

Figure 4.7: Frequency dependency of solvers.

As it is seen in the discussion of the multipole BEM, the required iterations increase with mesh refinement when the frequency is kept constant. In Fig. 4.8 the required iterations for the solution with a residual of 10^{-5} are plotted for the models L8 to L64 at $f = 600$ Hz. One notices that approximate inverse preconditioning of GMRES

decreases the number of iterations but still shows a significant increase with mesh refinement. The multigrid solver with approximate inverse smoother yields a drastic reduction of iterations and also restricts the increase with mesh refinement.

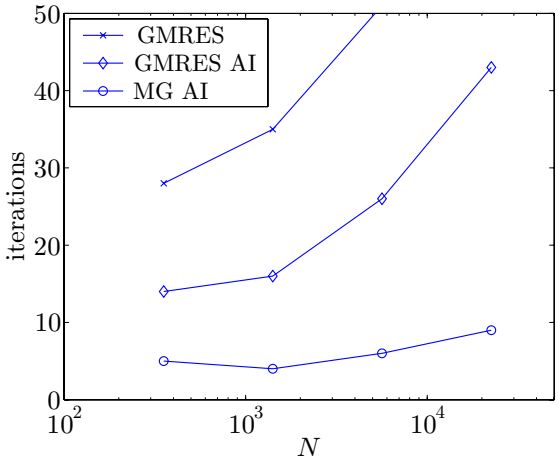

Figure 4.8: Required iterations for solution at $f = 600$ Hz.

For assessment of the numerical cost, the computing time is listed in Table 4.1 for simulations at $\kappa h = \text{const}$. The simulations are performed on the L16, L32 and L64 model (Table 2.1). The chosen frequencies correspond to the respective frequency $f_{\max}$, i.e. nine elements per wavelength. The multipole BEM is employed for the grids L32 and L64 with a nearfield size $c = 4$ and an expansion length $p = 4$, a parameter combination that yields multipole errors for the matrix-vector product of well below 10^{-4}. The high accuracy for the multipole algorithm is chosen to restrict the residual gap of GMRES as discussed in Section 5.3. The coarsest grid for all multigrid solvers is L4, i.e. a 3-grid, 4-grid, and 5-grid solver is used for the simulations on L16, L32 and L64, respectively.

For the simulations on L16 at 600 Hz using the conventional BEM, the computing time for setup of the BEM on the finest level t_{FL} is dominant. The time for setup of the lower levels t_{LL}, setup of the approximate inverse preconditioner t_{AI} and the solution t_{solve} is negligible. For the simulation on L32 at 1200 Hz, the multipole method is employed on the finest grid. One notices that t_{FL} per degree of freedom is greatly reduced, whereas t_{solve} becomes important now. The solution step is performed fastest by the multigrid solver. However, due to the setup on the lower levels, the simulation using the preconditioned GMRES requires the lowest total computing time t_{total}. For the simulation on L64 at 2400 Hz, preconditioned GMRES performs best for solution time and total time. The high solution time for the multigrid solver is due to the multipole iterations on the second finest grid.

Table 4.1: Computing time for simulations at $\kappa h = \text{const}$.

	f	solver	iters.	t_{LL}	t_{FL}	t_{AI}	t_{solve}	t_{total}
L16	600 Hz	GMRES	35	–	6 min	–	$<<$ 1 min	6 min
		GMRES AI	16	–	6 min	$<<$ 1 min	$<<$ 1 min	6 min
		MG 3 grids	4	1 min	6 min	$<<$ 1 min	$<<$ 1 min	7 min
L32	1200 Hz	GMRES	34	–	12 min	–	16 min	28 min
		GMRES AI	18	–	12 min	1 min	9 min	22 min
		MG 4 grids	4	7 min	12 min	1 min	6 min	25 min
L64	2400 Hz	GMRES	36	–	42 min	–	76 min	118 min
		GMRES AI	18	–	42 min	2 min	42 min	86 min
		MG 5 grids	5	17 min	42 min	2 min	77 min	138 min

The example shows that the multigrid solver with approximate inverse smoother requires a very low number of iterations. However, the computing cost is not reduced compared to preconditioned GMRES. For practical applications the preconditioned GMRES is the recommended solution strategy, since it does not rely on well-chosen parameters and does not require a hierarchy of boundary triangulations.

As a second example, the influence of approximate inverse preconditioning is demonstrated on the boundary element model of the brake disk. The achieved residual for solution with GMRES and preconditioned GMRES is plotted in Fig. 4.9. As for the L-shape, the preconditioning yields a much improved convergence rate. The multigrid is not applied to the solver, since a grid hierarchy is not available.

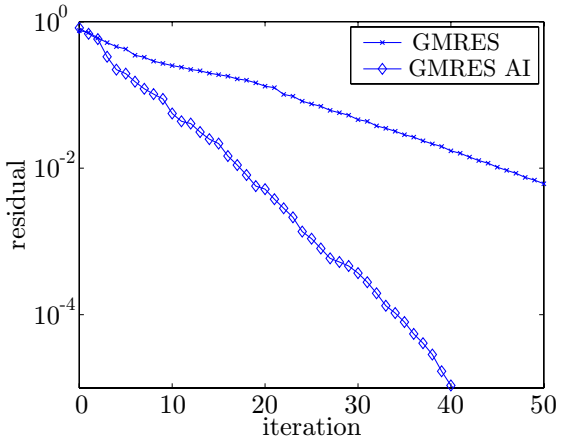

Figure 4.9: Convergence of GMRES for brake disk model.

Chapter 5

BEM-FEM coupling for structure-acoustic field interaction

In the preceding chapters, the efficient application of BEM for structural-acoustic computations is discussed. The effect of the acoustic field on the vibrating structure is neglected so far. For many applications this is not acceptable, for example, when flexible structures are excited by high sound pressure levels. In this situation, the simulation of the acoustic field must be fully coupled to the simulation of the structural vibrations.

Classical BEM-FEM coupling schemes imply a strong coupling between the nodal variables which requires conforming discretizations in the acoustic and structural subdomains. More flexibility is obtained by using a mortar coupling algorithm that allows the combination of non-conforming discretizations. A Lagrange multiplier is discretized on the coupling interface as mortar to glue together the subdomains. Using the mortar algorithm, different element sizes and shape functions can be used in the subdomains what can increase the efficiency of the simulation significantly. Furthermore, independent adaptive mesh refinement is possible in the subdomains.

The aim of this chapter is to derive a mortar algorithm for BEM-FEM coupling that allows the use of the fast multipole BEM. In particular the solution strategy must be adopted to the situation that only matrix-vector products of the BEM system can be evaluated. The fast multipole BEM is combined in the mortar scheme with a FEM formulation for plate vibrations to yield an efficient tool for the simulation of structure-acoustic field interaction problems.

5.1 Structure-acoustic field interaction

Before developing the mortar coupling scheme, the physical problem of acoustic-structure interaction is shortly reviewed. A structure is assumed to be fully submerged in an acoustic fluid as displayed in Fig. 5.1. The structure is modeled as a thin Kirchhoff plate on the interaction boundary Γ^{int}. The out-of-plane displacement is denoted by w and the loading $f = f^{\text{f}} + f^{\text{e}}$ consists of surface forces due to the acoustic field f^{f} and externally applied forces f^{e}. The time-harmonic pressure p in the acoustic field Ω^{f} is governed by the Helmholtz equation $\triangle p + \kappa^2 p = 0$ with the circular wavenumber $\kappa = \omega/c^{\text{f}}$. The acoustic flux on the boundary is defined as $q = \partial p/\partial n^{\text{f}}$. The boundary $\partial\Omega^{\text{f}} = \Gamma = \Gamma^{\text{int}} \cup \Gamma^{\text{D}} \cup \Gamma^{\text{N}}$ is composed of acoustic-structure interface, Dirichlet boundary, and Neumann boundary. The Sommerfeld radiation condition is inherently fulfilled by the BEM for computations on exterior domains. On the acoustic-structure interface Γ^{int} the coupling conditions enforce equilibrium $p = f^{\text{f}}$ and continuity $q = -\rho^{\text{f}}\omega^2 w$ where the different orientation of the normal vectors in the structure and fluid subdomains is considered.

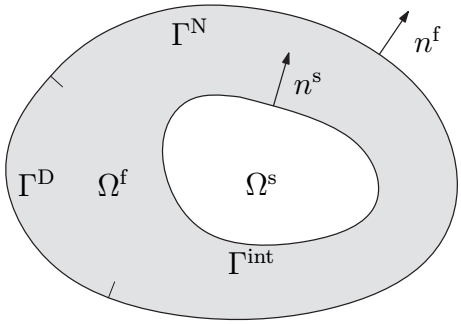

Figure 5.1: Acoustic-structure interaction model problem.

5.2 Mortar coupling algorithm

The choice of the Lagrange multiplier is the essential step for the formulation of the mortar coupling algorithm. In the presented approach, the pressure on the acoustic-structure interface is employed as Lagrange multiplier, i.e. $\lambda = p^{\text{int}} = f^{\text{f}}$.

For the simulation of the Kirchhoff plate, a finite element formulation is chosen. For

time-harmonic vibration, the bilinear form for a plate of thickness t is given by

$$a(w,v) = \int_{\Gamma^{\text{int}}} \Bigg[D(1-\nu) \left(\frac{\partial^2 v}{\partial x_1^2} \frac{\partial^2 w}{\partial x_1^2} + 2 \frac{\partial^2 v}{\partial x_1 \partial x_2} \frac{\partial^2 w}{\partial x_1 \partial x_2} + \frac{\partial^2 v}{\partial x_2^2} \frac{\partial^2 w}{\partial x_2^2} \right) + D\nu \triangle v \triangle w - \rho^{\text{s}} t \omega^2 w v \Bigg] \, \mathrm{d}s_x \,. \quad (5.1)$$

with the bending stiffness $D = Et^3/\left[12(1-\nu^2)\right]$, Young's modulus E, Poisson's ratio ν and density ρ^{s}. The displacement field of the fluid-loaded plate is obtained by the solution of

$$a(w, v^w) - \int_{\Gamma^{\text{int}}} v^w \lambda \, \mathrm{d}s_x = \int_{\Gamma^{\text{int}}} v^w f^{\text{e}} \, \mathrm{d}s_x \,. \quad (5.2)$$

For the acoustic domain a BEM is derived. Since in contrast to Chapter 2, an interior acoustics problem is considered, the representation formula is restated

$$p(x) = \int_\Gamma P^*(x,y)\, q(y) \; \mathrm{d}s_y - \int_\Gamma \frac{\partial P^*(x,y)}{\partial n_y} \, p(y) \, \mathrm{d}s_y \,, \quad x \in \Omega^{\text{f}} \,. \quad (5.3)$$

Taking the limit on the smooth boundary $\Omega^{\text{f}} \ni x \to \Gamma$, one obtains the boundary integral equation

$$p(x) = \frac{1}{2} p(x) + \underbrace{\int_\Gamma P^*(x,y)\, q(y) \; \mathrm{d}s_y}_{(Vq)(x)} - \underbrace{\int_\Gamma \frac{\partial P^*(x,y)}{\partial n_y} \, p(y) \; \mathrm{d}s_y}_{(Kp)(x)} \,, \quad x \in \Gamma \,, \quad (5.4)$$

where as before $(Vq)(x)$ and $(Kp)(x)$ are the single and double layer potential, respectively. The hyper-singular boundary integral equation is obtained by taking the normal derivative of (2.7)

$$q(x) = \frac{1}{2} q(x) + \underbrace{\int_\Gamma \frac{\partial P^*(x,y)}{\partial n_x} \, q(y) \; \mathrm{d}s_y}_{(K'q)(x)} - \underbrace{\int_\Gamma \frac{\partial^2 P^*(x,y)}{\partial n_x \partial n_y} \, p(y) \; \mathrm{d}s_y}_{-(Dp)(x)} \,, \quad x \in \Gamma \,, \quad (5.5)$$

where $(K'q)(x)$ and $(Dp)(x)$ are the adjoint double layer potential and the hyper-singular operator, respectively.

The pressure and flux fields on the boundary are decomposed to yield a symmetric formulation: $p = p^{\text{int}} + \tilde{p} + \bar{p}$ and $q = q^{\text{int}} + \tilde{q} + \bar{q}$, where $\bar{p}$ and $\bar{q}$ are the prescribed Dirichlet and Neumann boundary conditions, respectively. The extensions are $\tilde{p} = 0$ on $\Gamma^{\text{int}} \cup \Gamma^{\text{D}}$ and $\tilde{q} = 0$ on $\Gamma^{\text{int}} \cup \Gamma^{\text{N}}$.

On the structure-acoustic field interface Γ^{int}, the boundary integral equation (5.4) is weighted with test functions v^q and the term $p^{\text{int}} - \lambda$ is added to enforce the

equilibrium coupling condition

$$\begin{aligned}\int_{\Gamma^{\mathrm{int}}} v^q(Vq^{\mathrm{int}})(x)\,\mathrm{d}s_x + \int_{\Gamma^{\mathrm{int}}} v^q(V\tilde{q})(x)\,\mathrm{d}s_x + \int_{\Gamma^{\mathrm{int}}} v^q\left(-\frac{1}{2}I - K\right)p^{\mathrm{int}}(x)\,\mathrm{d}s_x \\ - \int_{\Gamma^{\mathrm{int}}} v^q(K\tilde{p})(x)\,\mathrm{d}s_x + \int_{\Gamma^{\mathrm{int}}} v^q(p^{\mathrm{int}} - \lambda)(x)\,\mathrm{d}s_x \\ = -\int_{\Gamma^{\mathrm{int}}} v^q(V\bar{q})(x)\,\mathrm{d}s_x + \int_{\Gamma^{\mathrm{int}}} v^q\left(\frac{1}{2}I + K\right)\bar{p}(x)\,\mathrm{d}s_x\,. \quad (5.6)\end{aligned}$$

Likewise, on the Dirichlet boundary

$$\begin{aligned}\int_{\Gamma^{\mathrm{D}}} v^q(Vq^{\mathrm{int}})(x)\,\mathrm{d}s_x + \int_{\Gamma^{\mathrm{D}}} v^q(V\tilde{q})(x)\,\mathrm{d}s_x - \int_{\Gamma^{\mathrm{D}}} v^q(Kp^{\mathrm{int}})(x)\,\mathrm{d}s_x \\ - \int_{\Gamma^{\mathrm{D}}} v^q(K\tilde{p})(x)\,\mathrm{d}s_x = -\int_{\Gamma^{\mathrm{D}}} v^q(V\bar{q})(x)\,\mathrm{d}s_x + \int_{\Gamma^{\mathrm{D}}} v^q\left(\frac{1}{2}I + K\right)\bar{p}(x)\,\mathrm{d}s_x\,.\end{aligned} \quad (5.7)$$

The hyper-singular boundary integral equation (5.5) is tested on the interface Γ^{int}

$$\begin{aligned}\int_{\Gamma^{\mathrm{int}}} v^p(Dp^{\mathrm{int}})(x)\,\mathrm{d}s_x + \int_{\Gamma^{\mathrm{int}}} v^p(D\tilde{p})(x)\,\mathrm{d}s_x + \int_{\Gamma^{\mathrm{int}}} v^p\left(-\frac{1}{2}I + K'\right)q^{\mathrm{int}}(x)\,\mathrm{d}s_x \\ + \int_{\Gamma^{\mathrm{int}}} v^p(K'\tilde{q})(x)\,\mathrm{d}s_x = -\int_{\Gamma^{\mathrm{int}}} v^p\left(D\bar{p}\right)(x)\,\mathrm{d}s_x + \int_{\Gamma^{\mathrm{int}}} v^p\left(\frac{1}{2}I - K'\right)\bar{q}(x)\,\mathrm{d}s_x\,,\end{aligned} \quad (5.8)$$

as well as on the Neumann boundary Γ^{N}

$$\begin{aligned}\int_{\Gamma^{\mathrm{N}}} v^p(Dp^{\mathrm{int}})(x)\,\mathrm{d}s_x + \int_{\Gamma^{\mathrm{N}}} v^p(D\tilde{p})(x)\,\mathrm{d}s_x + \int_{\Gamma^{\mathrm{N}}} v^p(K'q^{\mathrm{int}})(x)\,\mathrm{d}s_x \\ + \int_{\Gamma^{\mathrm{N}}} v^p(K'\tilde{q})(x)\,\mathrm{d}s_x = -\int_{\Gamma^{\mathrm{N}}} v^p\left(D\bar{p}\right)(x)\,\mathrm{d}s_x + \int_{\Gamma^{\mathrm{N}}} v^p\left(\frac{1}{2}I - K'\right)\bar{q}(x)\,\mathrm{d}s_x\,.\end{aligned} \quad (5.9)$$

The continuity condition is enforced by

$$\int_{\Gamma^{\mathrm{int}}} v^\lambda\left(\rho^{\mathrm{f}}\omega^2 w + q^{\mathrm{int}}\right)\,\mathrm{d}s_x = 0\,. \quad (5.10)$$

Special attention has to be paid to the discretization of the saddle point problem consisting of Eqs. (5.2) and (5.6)–(5.10). For a unique solution, a stability requirement—the discrete Babuška-Brezzi or inf-sup condition—has to be established (Brezzi and Fortin, 1991). A strict mathematical proof is beyond the scope of

the thesis, however, some aspects of the stability estimates and definition of the mortar spaces for three-dimensional problems that are derived by Braess and Dahmen (1998) are adopted to the current problem.

For the discretization of the Kirchhoff plate, the ansatz functions must provide C^1 continuity. A four-node finite plate element proposed by Zienkiewicz and Taylor (2000) is chosen. On each node, it possesses three degrees of freedom: the out-of-plane displacement and two rotations. Incomplete bi-cubic ansatz functions $\boldsymbol{\varphi}^w$ are used for interpolation. They do not guarantee continuity of the slope normal to the element edges, however, convergence is well established for rectangular elements.

$$w_h(x) = \boldsymbol{\varphi}^w(x)^{\mathrm{T}}\mathbf{w}\,. \tag{5.11}$$

A consistent discretization of distributed pressure loads on the plate would induce nodal forces on the rotational degrees of freedom. For the load vector in the coupling algorithm, thus, simplified shape functions $\tilde{\boldsymbol{\varphi}}^w(x)$ are used where the contribution of the rotational degrees of freedom is set to zero.

The acoustic pressure and flux are interpolated on the boundary element triangulation using linear ansatz functions $\boldsymbol{\varphi}^p$ and constant ansatz functions $\boldsymbol{\varphi}^q$, respectively.

$$p_h(x) = \boldsymbol{\varphi}^p(x)^{\mathrm{T}}\mathbf{p}\,, \qquad q_h(x) = \boldsymbol{\varphi}^q(x)^{\mathrm{T}}\mathbf{q}\,. \tag{5.12}$$

To fulfill the Babuška-Brezzi condition, the ansatz space for the Lagrange multiplier must be rich enough. This can be complied with by choosing the boundary element mesh as the slave or mortar triangulation and using linear ansatz functions for the Lagrange multiplier. At the edges of the coupling interface, the linear ansatz space must be restricted, since the Lagrange multiplier, i.e. the fluid load on the plate, is not unique where structural Dirichlet boundary conditions are applied. A one-dimensional illustration of the modified ansatz functions $\boldsymbol{\varphi}^\lambda$ is shown in Fig. 5.2.

$$\lambda_h(x) = \boldsymbol{\varphi}^\lambda(x)^{\mathrm{T}}\boldsymbol{\lambda}\,. \tag{5.13}$$

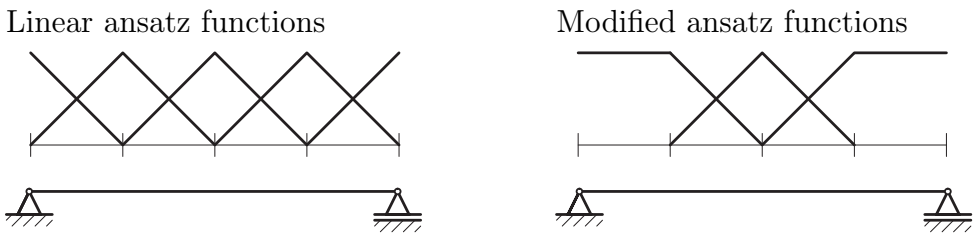

Figure 5.2: Modification of the ansatz space for the Lagrange multiplier

Using the shape functions Eqs. (5.11)–(5.13) and isoparametric test functions, one obtains the block skew-symmetric system of equations

$$\begin{pmatrix} \rho^{\mathrm{f}}\omega^2\mathbf{A} & \mathbf{0} & \mathbf{0} & \mathbf{0} & \mathbf{0} & -\mathbf{C}_{\mathrm{FEM}} \\ \mathbf{0} & \mathbf{V}_{\mathrm{i,i}} & \mathbf{V}_{\mathrm{i,D}} & \frac{1}{2}\mathbf{I} - \mathbf{K}_{\mathrm{i,i}} & -\mathbf{K}_{\mathrm{i,N}} & -\mathbf{C}_{\mathrm{BEM}} \\ \mathbf{0} & \mathbf{V}_{\mathrm{D,i}} & \mathbf{V}_{\mathrm{D,D}} & -\mathbf{K}_{\mathrm{D,i}} & -\mathbf{K}_{\mathrm{D,N}} & \mathbf{0} \\ \mathbf{0} & -\frac{1}{2}\mathbf{I}^{\mathrm{T}} + \mathbf{K}_{\mathrm{i,i}}^{\mathrm{T}} & \mathbf{K}_{\mathrm{i,D}}^{\mathrm{T}} & \mathbf{D}_{\mathrm{i,i}} & \mathbf{D}_{\mathrm{i,N}} & \mathbf{0} \\ \mathbf{0} & \mathbf{K}_{\mathrm{i,N}}^{\mathrm{T}} & \mathbf{K}_{\mathrm{D,N}}^{\mathrm{T}} & \mathbf{D}_{\mathrm{N,i}} & \mathbf{D}_{\mathrm{N,N}} & \mathbf{0} \\ \mathbf{C}_{\mathrm{FEM}}^{\mathrm{T}} & \mathbf{C}_{\mathrm{BEM}}^{\mathrm{T}} & \mathbf{0} & \mathbf{0} & \mathbf{0} & \mathbf{0} \end{pmatrix} \begin{pmatrix} \mathbf{w} \\ \mathbf{q}^{\mathrm{int}} \\ \tilde{\mathbf{q}} \\ \mathbf{p}^{\mathrm{int}} \\ \tilde{\mathbf{p}} \\ \boldsymbol{\lambda} \end{pmatrix}$$

$$= \begin{pmatrix} \rho^{\mathrm{f}}\omega^2 \int_{\Gamma^{\mathrm{int}}} \tilde{\boldsymbol{\varphi}}^w f^{\mathrm{e}} \,\mathrm{d}s_x \\ -\int_{\Gamma^{\mathrm{int}}} \boldsymbol{\varphi}^q (V\bar{q})(x) \,\mathrm{d}s_x + \int_{\Gamma^{\mathrm{int}}} \boldsymbol{\varphi}^q \left(\frac{1}{2}I + K\right) \bar{p}(x) \,\mathrm{d}s_x \\ -\int_{\Gamma^{\mathrm{D}}} \boldsymbol{\varphi}^q (V\bar{q})(x) \,\mathrm{d}s_x + \int_{\Gamma^{\mathrm{D}}} \boldsymbol{\varphi}^q \left(\frac{1}{2}I + K\right) \bar{p}(x) \,\mathrm{d}s_x \\ -\int_{\Gamma^{\mathrm{int}}} \boldsymbol{\varphi}^p \left(D\bar{p}\right)(x) \,\mathrm{d}s_x + \int_{\Gamma^{\mathrm{int}}} \boldsymbol{\varphi}^p \left(\frac{1}{2}I - K'\right) \bar{q}(x) \,\mathrm{d}s_x \\ -\int_{\Gamma^{\mathrm{N}}} \boldsymbol{\varphi}^p \left(D\bar{p}\right)(x) \,\mathrm{d}s_x + \int_{\Gamma^{\mathrm{N}}} \boldsymbol{\varphi}^p \left(\frac{1}{2}I - K'\right) \bar{q}(x) \,\mathrm{d}s_x \\ \mathbf{0} \end{pmatrix}, \quad (5.14)$$

where $\mathbf{A}$ is the dynamic FEM stiffness matrix and $\mathbf{V}$, $\mathbf{K}$, and $\mathbf{D}$ are the BEM system matrices evaluated on the boundary sections corresponding to their subscripts. The coupling matrices $\mathbf{C}_{\mathrm{FEM}}$ and $\mathbf{C}_{\mathrm{BEM}}$ are defined by integration of the respective shape functions over the coupling interface

$$\mathbf{C}_{\mathrm{FEM}} = \rho^{\mathrm{f}}\omega^2 \int_{\Gamma^{\mathrm{int}}} \tilde{\boldsymbol{\varphi}}^w(x) \boldsymbol{\varphi}^{\lambda}(x)^{\mathrm{T}} \,\mathrm{d}s_x \,, \qquad \mathbf{C}_{\mathrm{BEM}} = \int_{\Gamma^{\mathrm{int}}} \boldsymbol{\varphi}^q(x) \boldsymbol{\varphi}^{\lambda}(x)^{\mathrm{T}} \,\mathrm{d}s_x \,. \quad (5.15)$$

5.3 Iterative solution of the mortar saddle point problem

Direct iterations on the system (5.14) converge very poorly, thus, an Uzawa type algorithm is employed. For an introduction to iterative methods for saddle point problems, it is referred to Saad (2003).

In the Uzawa algorithm, the system (5.14) is solved for $\boldsymbol{\lambda}$ and iterations are applied on the reduced equation

$$\underbrace{\begin{pmatrix} \mathbf{C}_{\mathrm{FEM}}^{\mathrm{T}} & \mathbf{C}_{\mathrm{BEM}}^{\mathrm{T}} \end{pmatrix} \begin{pmatrix} (\rho^{\mathrm{f}}\omega^2\mathbf{A})^{-1} & \mathbf{0} \\ \mathbf{0} & \mathbf{B}^{-1} \end{pmatrix} \begin{pmatrix} \mathbf{C}_{\mathrm{FEM}} \\ \mathbf{C}_{\mathrm{BEM}} \end{pmatrix}}_{\mathbf{S}} \boldsymbol{\lambda} = \underbrace{\begin{pmatrix} \rho^{\mathrm{f}}\omega^2\mathbf{f}_{\mathrm{FEM}} \\ \mathbf{f}_{\mathrm{BEM}} \end{pmatrix}}_{\mathbf{f}}, \quad (5.16)$$

where the BEM matrix $\mathbf{B}$ was introduced to simplify the notation of (5.14). The matrix inverses in (5.16) are not evaluated explicitly, but conjugate gradient and GMRES iterations are applied on the FEM and BEM subsystems, respectively.

Instead of evaluating the exact matrix-vector product $\mathbf{S}\boldsymbol{\lambda}_k$ at each outer iteration step k, an approximation with a relative precision η_k is computed as

$$\tilde{\mathbf{S}}_k\boldsymbol{\lambda}_k = \mathbf{S}\boldsymbol{\lambda}_k + \mathbf{g}_k \tag{5.17}$$

with $||\mathbf{g}_k||_2 \leq \eta_k||\mathbf{S}\boldsymbol{\lambda}_k||_2$. For most applications of inexact Uzawa algorithms, i.e. nested inner-outer iterations, Newton type schemes are employed for the outer iterations. They offer the advantage that for the inner iterations a coarse approximation is sufficient in the beginning. Only with shrinking outer residual, the approximation of the inner systems must be improved. For the analysis of Newton type inexact Uzawa algorithms, it is referred to Elman and Golub (1994) and Bramble et al. (1997).

For the structure-acoustic field interaction system (5.16), standard Newton methods show a very poor convergence behavior and GMRES is thus employed for the outer iterations. GMRES offers quick convergence, however, the intuitive scheme—improving the precision of the inner approximation when the outer residual becomes small—breaks down. On the contrary, the precision of the inner approximation must be high in the beginning and can be relaxed subsequently.

An empirical relaxation strategy for a wide range of application is developed by Bouras and Frayssé (2000). Their procedure is supported by the analyses of Simoncini and Szyld (2003) and van den Eshof and Sleijpen (2004). For the inexact evaluation of the matrix-vector product (5.17), the Arnoldi algorithm on (5.16) creates an orthogonal basis that does not correspond to the Krylov space $\mathcal{K}_k(\mathbf{S}, \mathbf{r}_0)$, and the value $|\gamma_{k+1}|$ which is used to check the convergence of GMRES according to (4.9) does not correspond to the true residual $\mathbf{r}_k = \mathbf{f} - \mathbf{S}\boldsymbol{\lambda}_k$. This residual gap can be controlled by the proposed relaxation scheme.

For the solution of (5.16) with a target residual $||\mathbf{f} - \mathbf{S}\boldsymbol{\lambda}_k||_2 \leq \epsilon^{\text{outer}}$, a relative precision of

$$\eta_k = \frac{\epsilon^{\text{outer}}}{|\gamma_k|} \tag{5.18}$$

is required for the evaluation of the approximate matrix-vector product $\tilde{\mathbf{S}}_k\boldsymbol{\lambda}_k$ according to the analysis of van den Eshof and Sleijpen (2004). Thus, the inner systems $(\rho^{\text{f}}\omega^2\mathbf{A})^{-1}\mathbf{C}_{\text{FEM}}\boldsymbol{\lambda}_{\boldsymbol{k}}$ and $\mathbf{B}^{-1}\mathbf{C}_{\text{BEM}}\boldsymbol{\lambda}_{\boldsymbol{k}}$ must be solved with a relative residual of

$$\epsilon_k^{\text{inner}} = \underbrace{\frac{\left|\left|\tilde{\mathbf{S}}_k\boldsymbol{\lambda}_{\boldsymbol{k}}\right|\right|_2}{\left|\left|\begin{pmatrix}\mathbf{C}_{\text{FEM}}\\ \mathbf{C}_{\text{BEM}}\end{pmatrix}\boldsymbol{\lambda}_{\boldsymbol{k}}\right|\right|_2}}_{c_k} \frac{\epsilon^{\text{outer}}}{|\gamma_k|}\,. \tag{5.19}$$

The value of the first ratio c_k in (5.19) is not known prior to actually computing the approximations of the inner systems. Numerical experiments show that the value of the ratio usually does not change significantly from one outer iteration to the next. Thus, the ratio of the previous step can be used as a first guess to determine the required precision of the current approximation. Using the computed result, the true ratio is calculated and compared to the previous one. Only if there is a significant deviation, i.e. if the true ratio is significantly smaller than the guess, the approximation must be computed again up to the correct precision.

Preconditioning of the subsystems is essential for the efficiency of the solver. As an advantage of the presented approach, standard preconditioners for the FEM and BEM parts can be used. In the numerical examples, diagonal scaling and the approximate inverse approach presented in Chapter 4 are used which prove to work reasonably well for the BEM system. For the FEM part, i.e. for the solution of the plate system, specialized solution schemes—e.g. advanced direct methods or multigrid solvers—should be used due to the poor conditioning of the biharmonic equation. However, since the focus of this work is on the BEM, the issue is not further addressed.

It should be noticed that the Uzawa algorithm provides a good scaling of the exterior iterations. In contrast to the coupling formulation of Wagner (2000) where the conditioning of the system strongly depends on the choice of the field variable, this influence is canceled out in (5.16) by the multiplication with the coupling matrices.

5.4 Numerical examples

The proposed coupling algorithm is demonstrated on two examples. First, the response of an elastic plate backed by a closed acoustic cavity is examined. For this simple model problem, an analytic series solution is developed by Pretlove (1966) that is outlined in Appendix C and used as a reference solution. The second example is the simulation of the sound field emitted from a submerged plate in a water basin. The numerical results are compared to experiments conducted in the hydro-acoustic lab at the Institut A für Mechanik.

5.4.1 Plate backed by a closed acoustic cavity

The elastic plate considered in the first example has the dimensions $1\,\mathrm{m} \times 1\,\mathrm{m}$ and a thickness of $t = 0.01\,\mathrm{m}$. It is made from steel ($E = 2.1 \times 10^{11}\,\mathrm{N/m^2}$, $\nu = 0.3$,

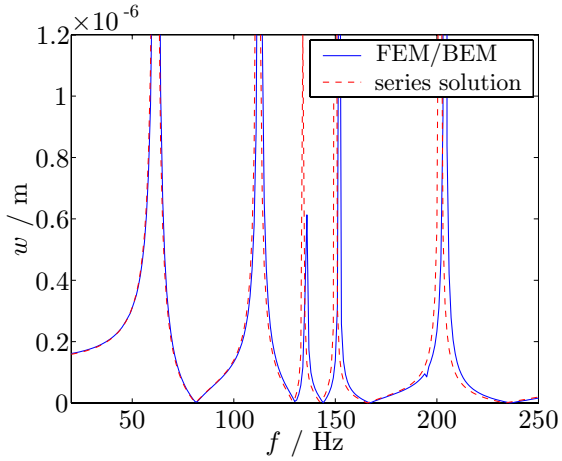

Figure 5.3: Frequency response of cavity backed panel. Plate displacement w at position $(0.2,\ 0.3)\,\mathrm{m}$.

$\rho^{\mathrm{s}} = 7900\,\mathrm{kg/m^3}$) and is simply supported on all edges. The panel is coupled to a closed acoustic cavity with dimensions $1\,\mathrm{m} \times 1\,\mathrm{m} \times 1\,\mathrm{m}$. The remaining surfaces of the cavity are reverberant walls, i.e. homogeneous Neumann boundary conditions ($\bar{q} = 0$) are applied. The acoustic fluid is water ($c^{\mathrm{f}} = 1481\,\mathrm{m/s}$, $\rho^{\mathrm{f}} = 1000\,\mathrm{kg/m^3}$).

For the simulation of the frequency response of the cavity backed panel, a boundary element mesh with 316 elements on the interface and a 20×20 finite plate element mesh is used. The computed frequency response function at the point $(0.2,\ 0.3)\,\mathrm{m}$ on the plate due to a force of $F = 1\,\mathrm{N}$ at the same position is plotted in Fig. 5.3. For comparison, the analytical series solution is plotted as dashed line. The BEM-FEM results agree completely with the analytic series solution in the lower frequency regime and one notices increasing deviation for higher frequencies.

The vibration modes of the plate close to the resonance frequencies are shown in Fig. 5.4. Comparing the vibration modes to the eigenmodes of an uncoupled plate, the effect of the acoustic cavity is particularly noticeable for mode shapes that have a non-zero average flux over the interface. Then, the stiffness effect of the cavity plays a dominant role. For example, the first uncoupled eigenfrequency of the plate is at 49 Hz whereas its mode shape can be identified at a frequency of 132 Hz for the coupled system. Mode shapes with zero average flux are found at frequencies slightly below their uncoupled counterparts due to the added mass effect of the acoustic fluid.

The convergence of the mortar coupling algorithm is studied at a frequency of 180 Hz. The acoustic pressure on the surface of the cavity and the plate displacement ob-

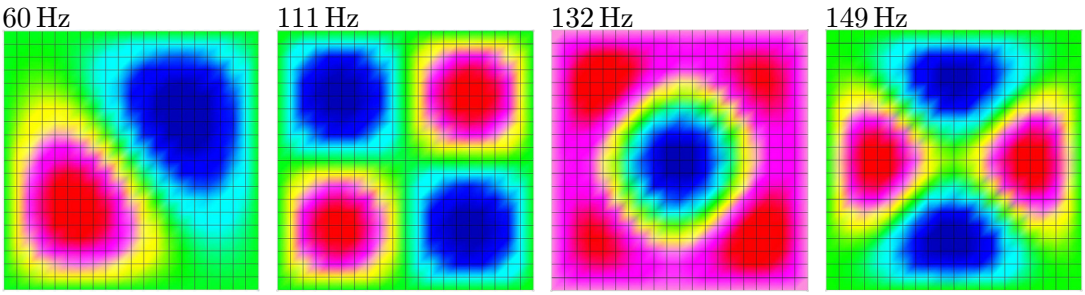

Figure 5.4: Vibration modes of cavity backed plate.

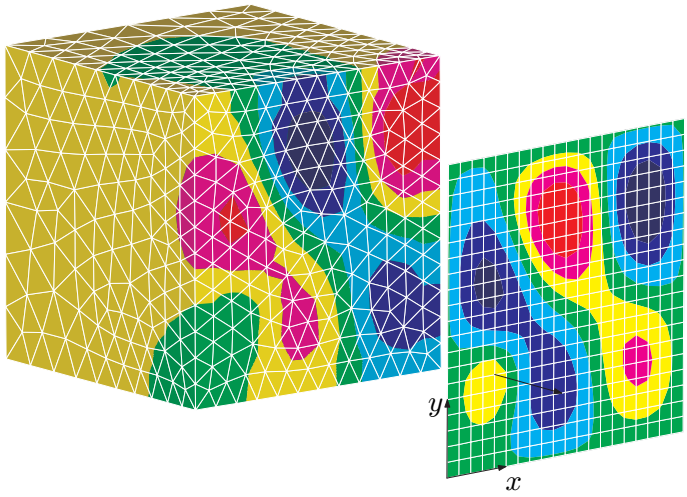

Figure 5.5: Surface pressure distribution and plate displacement at 180 Hz.

tained for a simulation using the boundary element mesh with 316 elements on the interface and 20×20 finite plate elements are displayed in Fig. 5.5. By inspection, one finds the discretization to resolve the fields sufficiently and a typical engineering error of a few per cent is expected.

The flexibility of the mortar coupling algorithm allows an independent refinement of the FEM and BEM meshes. The convergence behavior of the structure error e_2^{s} and the fluid error e_2^{f} is documented in Tab. 5.1 and Fig. 5.6. The errors are defined as

$$e_2^{\mathrm{s}} = \frac{||\mathbf{w}_{\mathrm{FEM}} - \mathbf{w}_{\mathrm{series}}||_2}{||\mathbf{w}_{\mathrm{series}}||_2} \qquad \text{and} \qquad e_2^{\mathrm{f}} = \frac{||\mathbf{p}_{\mathrm{BEM}}^{\mathrm{int}} - \mathbf{p}_{\mathrm{series}}^{\mathrm{int}}||_2}{||\mathbf{p}_{\mathrm{series}}^{\mathrm{int}}||_2}\,. \tag{5.20}$$

The simulation on the finest BEM grid, i.e. with 2936 boundary elements on the interface and a total of 11,680 boundary elements, is computed using the fast multipole BEM to take advantage of the largely reduced memory requirements. A

coupled simulation of this large model using the standard BEM is not possible on the available hardware. For the multipole algorithm, a nearfield parameter of $c = 4$ and an expansion parameter of $p = 5$ are employed according to Chapter 3. This parameter combination is chosen to yield a very accurate multipole evaluation of the inner BEM matrix-vector products to satisfy the requirements of the inexact Uzawa algorithm for a true residual of the Lagrange multiplier of 10^{-4}.

The fluid error, that corresponds to the error of the Lagrange multiplier which is discretized on the BEM mesh, decreases with refinement of the FEM mesh until it approaches a value that corresponds to the discretization error of the chosen BEM mesh. The behavior of the structure error also depends on the accuracy of the acoustic model. For the finest BEM mesh, one observes the quadratic convergence rate that is expected for the FEM plate formulation. The acoustic field is approximated well enough for plate discretizations up to 80×80 elements. For the coarser BEM meshes, the convergence of the structure error is affected by the fluid errors.

Table 5.1: Error of displacement and pressure field on the interface at 180 Hz.

		outer iterations	BEM matrix-vector products	e_2^{s}	e_2^{f}
box 12	plate 20×20	28	1678	$6.28 \cdot 10^{-2}$	$8.19 \cdot 10^{-2}$
(316 interface	plate 30×30	28	1689	$5.54 \cdot 10^{-2}$	$7.48 \cdot 10^{-2}$
elements)	plate 40×40	28	1629	$4.05 \cdot 10^{-2}$	$6.71 \cdot 10^{-2}$
	plate 60×60	28	1628	$3.54 \cdot 10^{-2}$	$6.54 \cdot 10^{-2}$
	plate 80×80	28	1638	$3.40 \cdot 10^{-2}$	$6.50 \cdot 10^{-2}$
box 16	plate 20×20	36	2440	$4.79 \cdot 10^{-2}$	$5.79 \cdot 10^{-2}$
(572 interface	plate 30×30	36	2448	$2.72 \cdot 10^{-2}$	$4.17 \cdot 10^{-2}$
elements)	plate 40×40	36	2367	$2.85 \cdot 10^{-3}$	$4.16 \cdot 10^{-2}$
	plate 60×60	36	2371	$1.82 \cdot 10^{-2}$	$3.76 \cdot 10^{-2}$
	plate 80×80	36	2370	$1.66 \cdot 10^{-2}$	$3.72 \cdot 10^{-2}$
box 24	plate 20×20	42	3732	$3.93 \cdot 10^{-2}$	$4.54 \cdot 10^{-2}$
(1274 interface	plate 30×30	43	3683	$1.87 \cdot 10^{-2}$	$2.35 \cdot 10^{-2}$
elements)	plate 40×40	43	3687	$1.24 \cdot 10^{-2}$	$1.83 \cdot 10^{-2}$
	plate 60×60	43	3686	$8.57 \cdot 10^{-3}$	$1.62 \cdot 10^{-2}$
	plate 80×80	43	3688	$6.54 \cdot 10^{-3}$	$1.56 \cdot 10^{-2}$
box 36	plate 20×20	49	5860	$3.65 \cdot 10^{-2}$	$4.22 \cdot 10^{-2}$
(2936 interface	plate 30×30	50	5919	$1.71 \cdot 10^{-2}$	$1.94 \cdot 10^{-2}$
elements)	plate 40×40	50	5922	$9.74 \cdot 10^{-3}$	$1.12 \cdot 10^{-2}$
	plate 60×60	50	5921	$5.14 \cdot 10^{-3}$	$7.00 \cdot 10^{-3}$
	plate 80×80	50	5921	$1.95 \cdot 10^{-3}$	$6.25 \cdot 10^{-3}$

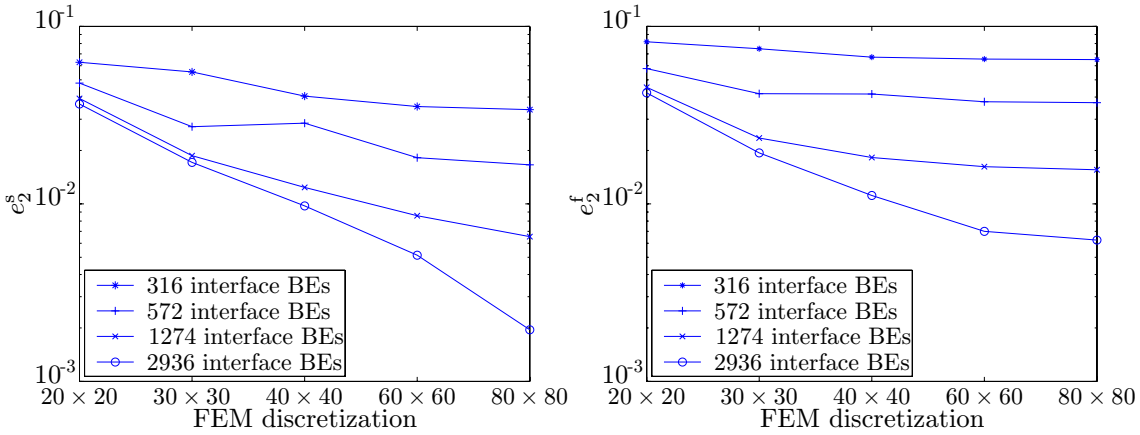

Figure 5.6: Convergence of fluid e_2^{f} and structure e_2^{s} error.

In the simulations presented in Tab. 5.1, a threshold residual of 10^{-4} is chosen for the outer GMRES iterations. For the approximation of the inner FEM system, the residual of the conjugate gradient solver is set to 10^{-7}. At this precision, the effect of inexact evaluation of the FEM part can be neglected. For the inner BEM system, GMRES is applied with a relaxation strategy according to (5.19) and diagonal preconditioning. The required number of outer iterations does not depend on the discretization of the finite element model, but only on the discretization of the boundary element model, i.e. the discretization of the Lagrange multiplier. With mesh refinement, a moderate increase of outer iterations can be observed. The total number of required BEM matrix-vector products increases significantly, since the conditioning of the inner systems deteriorates with boundary element mesh refinement. The influence of the relaxation strategy and preconditioning of the inner system on the efficiency of the solver is discussed in the following.

In Tab. 5.2 the numerical cost and the true residual are documented for the solution of the system arising from the simulation at 180 Hz using the boundary element mesh with 316 elements on the interface and 20×20 finite plate elements. The target residual of the outer GMRES is set to 10^{-4}. Using the relaxation scheme, the numerical cost is reduced from 2018 BEM matrix-vector products to 1678 BEM matrix-vector products, i.e. the computing time is reduced by more than 15%.

The relation (5.19) is found to be a sharp limit for restricting the residual gap of GMRES. As shown in Tab. 5.2, reducing the required precision for the inner BEM systems by a factor of two and four, respectively, the true residual increases to $1.29 \cdot 10^{-4}$ and $3.22 \cdot 10^{-4}$. The number of required BEM matrix-vector products is reduced accordingly, when allowing a residual gap. However, this scheme is not recommended, since it is usually more efficient to set a higher outer residual and to

Table 5.2: Choice of residual $\epsilon_k^{\text{inner}}$ for solution of BEM system. Target residual for inexact Uzawa algorithm $\epsilon^{\text{outer}} = 10^{-4}$.

$\epsilon_k^{\text{inner}}$	outer iterations	BEM matrix-vector products	GMRES residual	true residual
fixed strategy				
$c_k \epsilon^{\text{outer}}$	28	2018	$9.06 \cdot 10^{-5}$	$1.03 \cdot 10^{-4}$
relaxation strategy				
$c_k \epsilon^{\text{outer}} / \lvert\gamma_k\rvert$	28	1678	$9.06 \cdot 10^{-5}$	$1.01 \cdot 10^{-4}$
$2c_k \epsilon^{\text{outer}} / \lvert\gamma_k\rvert$	28	1604	$9.09 \cdot 10^{-5}$	$1.29 \cdot 10^{-4}$
$4c_k \epsilon^{\text{outer}} / \lvert\gamma_k\rvert$	28	1520	$9.09 \cdot 10^{-5}$	$3.22 \cdot 10^{-4}$
$\epsilon^{\text{outer}} = 3 \cdot 10^{-4}$				
$c_k \epsilon^{\text{outer}} / \lvert\gamma_k\rvert$	26	1487	$2.09 \cdot 10^{-4}$	$2.92 \cdot 10^{-4}$

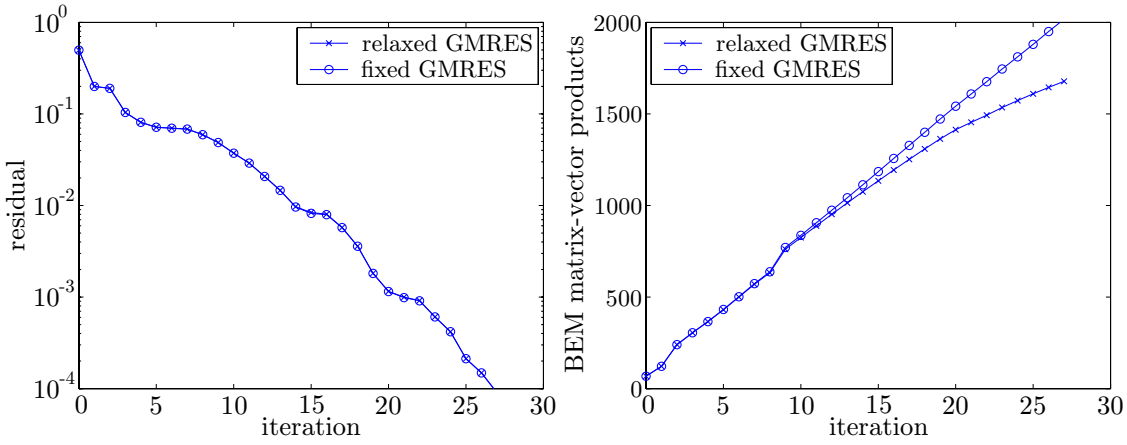

Figure 5.7: Convergence and BEM matrix-vector products of inexact Uzawa solver.

restrict the residual gap.

The convergence of the outer GMRES iterations for the fixed and the relaxation strategy are compared in Fig. 5.7. The achieved residuals are identical for the two strategies approving the relaxation according to (5.19). The reduction of required matrix-vector products for the relaxation strategy takes place as the outer residual decreases. The overall saving is moderate, since GMRES shows the typical superlinear convergence behavior, i.e. the majority of outer GMRES iterations is required while the residual is not yet reduced significantly.

The acceleration of the solution of the inner BEM systems by preconditioning is

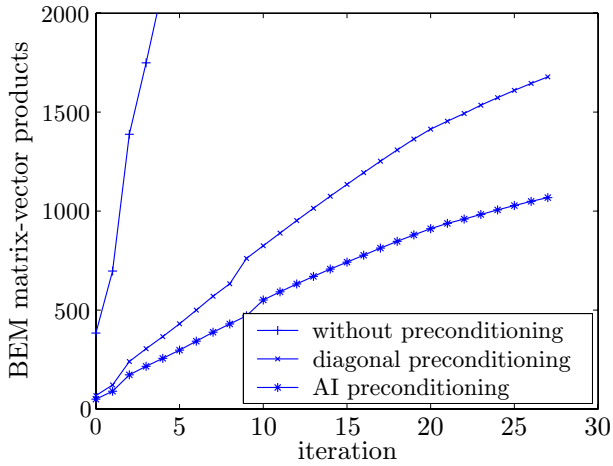

Figure 5.8: Preconditioning of inner BEM system for inexact Uzawa algorithm with relaxed GMRES iterations.

essential for the efficiency of the proposed solver. The required number of matrix-vector products for approximating the inner BEM system with GMRES without, with diagonal, and with approximate inverse preconditioning is plotted in Fig. 5.8. Without preconditioning, a very high number of matrix-vector products is observed, which is prohibitive for a practical applications. Diagonal preconditioning and approximate inverse preconditioning, both yield a significant improvement. The approximate inverse approach performs superior and is recommended for the solution of coupled BEM systems.

The importance of the modification of the Lagrange multiplier ansatz space as illustrated in Fig. 5.2 can be demonstrated very clearly for simulations on a regular grid. In Fig. 5.9, the pressure on the interface at 180 Hz is plotted for computations using a linear ansatz space for the Lagrange multiplier on the left and using the modified ansatz space on the right. The original Lagrange multipliers yield a rotated checkerboard pattern that is typical for a violated inf-sup condition.

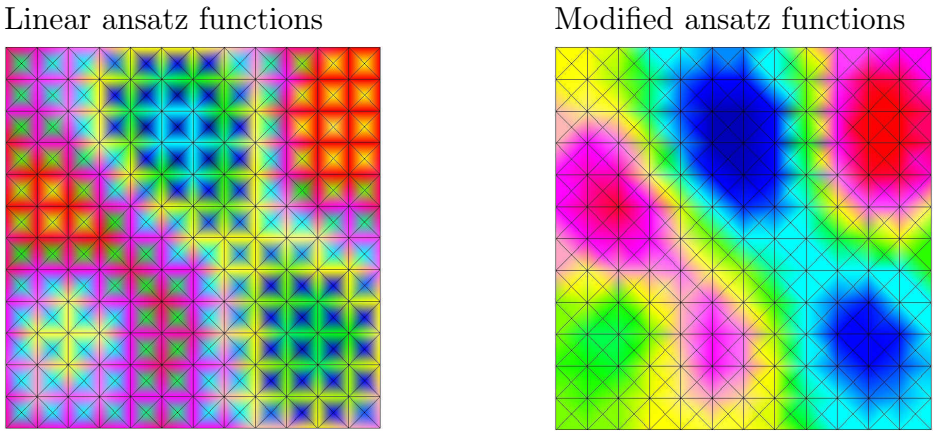

Figure 5.9: Lagrange multiplier on coupling interface.

5.4.2 Sound radiation by a submerged plate

A practical application of the mortar FEM-BEM coupling algorithm is the simulation of experiments on active structural-acoustic control in the hydro-acoustic lab at the Institut A für Mechanik (Fein and Gaul, 2002). For the chosen example, a rectangular plate ($0.475\,\mathrm{m} \times 0.48\,\mathrm{m}$, $t = 1.5\,\mathrm{mm}$) is mounted on the box depicted in Fig. 5.10 and submerged in the water pool. Plate vibrations are excited by a shaker inside the box, and the acceleration on the plate as well as the acoustic pressure in the pool are recorded.

For the simulations, a BEM mesh of the pool and the box is set up that consists of 4726 triangular elements and that is shown without the top-surface elements in Fig. 5.11. The lower right hand corner of the plate is chosen as origin for the displayed coordinate system. Homogeneous Dirichlet boundary conditions are applied on the pressure-free surface of the pool, whereas the pool walls are modeled as rigid, i.e. homogeneous Neumann boundary conditions are applied. The plate is discretized using 16×16 finite elements and is assumed to be clamped onto the rigid box.

Figure 5.10: Hydro-acoustic lab and submergeable box.

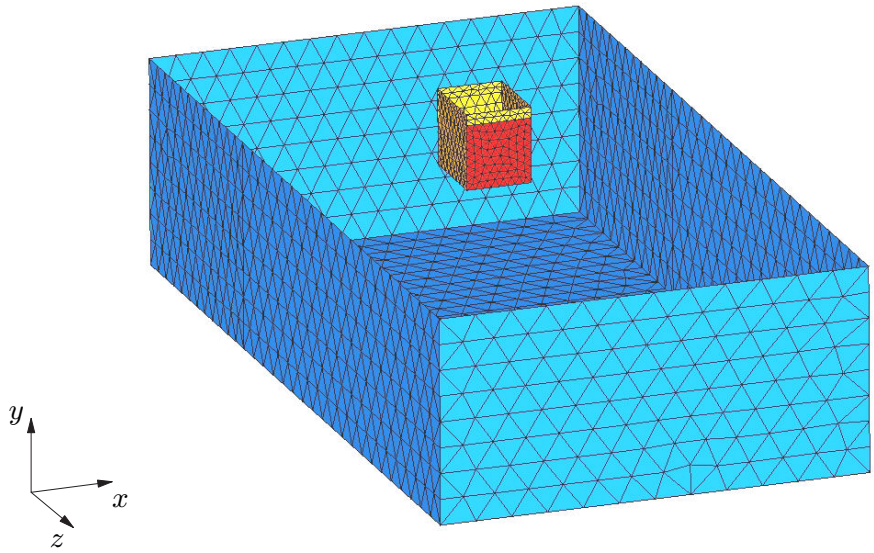

Figure 5.11: BEM model of pool and hydro-acoustic box.

In Fig. 5.12 the simulated and experimental frequency response functions for the plate displacement at position (0.42, 0.32) m and the acoustic pressure in the pool at position (0.15, −0.50, 0.51) m are plotted. The shaker is mounted at the position (0.20, 0.11) m on the plate and the forcing amplitude is used to normalize the plotted values. One notices that the principal behavior of simulation and experiment correlates. The differences can be traced back to various sources. The peaks in the experimental frequency response functions at 55 Hz, 71 Hz, and 113 Hz

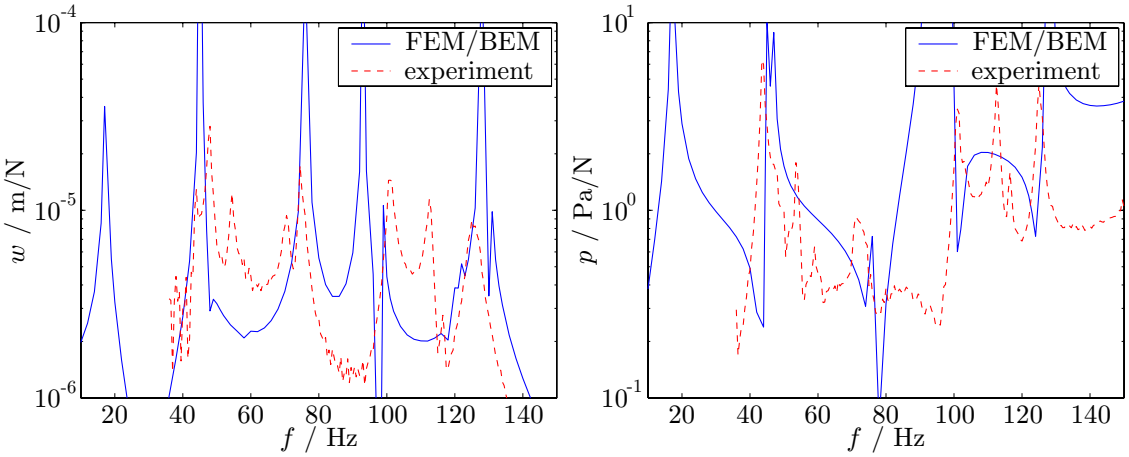

Figure 5.12: Experimental and computed frequency response of submerged plate.

are due to resonance frequencies of the pool's front wall that is modeled as rigid in the FEM-BEM simulation. The influence of mounting the plate onto the box plays a dominant role as well: sealing material and fixing screws introduce a vast amount of model uncertainties. Finally, the acoustic boundary conditions of the pool walls must be determined in more detail. In this context, the simulation results are satisfying, however, more effort should be placed on the modeling of the system pool-box-plate.

Chapter 6

Conclusions

The goal of the thesis is to provide an efficient simulation tool for the prediction of sound radiation from technical structures. The boundary element method is used as the basic numerical technique since it allows the simulation in unbounded domains. Only the surface of the sound radiating structure must be discretized which implies a very low cost for mesh generation and preprocessing. For the chosen Galerkin formulation, a numerical quadrature scheme is developed that allows the efficient numerical evaluation of the singular integrals. To avoid critical frequencies when computing exterior Neumann problems, the Burton-Miller approach is employed. The hyper-singular operator that is required in the formulation is regularized and reduced to the evaluation of the single layer potential.

The numerical cost of the BEM is significantly reduced by the fast multipole algorithm. Instead of setting up the fully populated BEM matrices, the matrix-vector product is evaluated by a multilevel series expansion scheme. The numerical complexity—computing time and memory requirement—is thus reduced from $\mathcal{O}(N^2)$ to $\mathcal{O}(N \log^2 N)$ in the number of unknowns which allows the application of the BEM for large-scale simulations. Essential for the multipole algorithm is the use of diagonal translation operators derived from the multipole expansion of the fundamental solution. Asymptotic estimates of the truncation error give guidelines for the proper choice of the expansion length. An academic example as well as the engineering application of sound radiation from a brake disk demonstrate the efficiency of the developed multipole BEM.

For the solution of large BEM systems, iterative methods must be employed. Two different techniques are developed in the thesis: GMRES with preconditioning by an approximate inverse approach and a multigrid solver. The comparison of the two methods shows that the multigrid solver provides a superior convergence. However,

the cost per iteration is higher for the multigrid, so that no major reduction of computing time is achieved. Since the multigrid solver requires a grid hierarchy and is thus difficult to implement in practical applications, the preconditioned GMRES is recommended as solution technique.

For the simulation of structure-acoustic field interaction, a mortar BEM-FEM coupling algorithm is derived. The mortar scheme is based on Lagrange multipliers and allows the coupling of non-conforming discretizations. This can improve the efficiency of the coupled simulation, since specialized ansatz functions and adapted element sizes can be used in the subdomains. For the solution of the mortar saddle point problem, a modified Uzawa algorithm is implemented. A relaxed GMRES method is employed for the outer iterations on the reduced system for the Lagrange multiplier whereas the inner FEM and BEM systems are approximated by conjugate gradient and preconditioned GMRES iterations, respectively. The solution technique allows the use of the multipole BEM for coupled problems which reduces the memory requirements significantly. However, due to the nested iteration scheme, the iteration time can be rather long. Further work should thus be devoted to the development of suitable solvers for the coupled system that reduce the number of required matrix-vector products.

The presented work is seen as a contribution to promote fast BEM for industrial applications. It is shown that the use of advanced numerical algorithms can significantly improve the efficiency of structural-acoustic simulations. However, besides the crucial point of computing cost, reliability and simplicity of use must also be kept in mind for a successful application. It is reminded that even the standard BEM is not a black-box simulation tool which yields results on a simple click, but a fair amount of insight into the method is required to apply it to engineering problems. So the additional complexity when employing the fast multipole BEM is assessed small compared to the savings offered by the method and its practical application can be encouraged.

Appendix A

Quadrature of singular integrals

In the Galerkin BEM integrals of the type

$$\int_\nu \varphi_\nu(x) \int_\mu k(x-y)\varphi_\mu(y)\,\mathrm{d}s_y\,\mathrm{d}s_x \tag{A.1}$$

must be evaluated, where ν and μ are elements of the boundary triangulation and the kernel functions $k(x-y)$ are the fundamental solution

$$P^*(x,y) = \frac{\mathrm{e}^{\mathrm{i}\kappa|x-y|}}{4\pi|x-y|} \tag{A.2}$$

or its normal derivative

$$\frac{\partial P^*(x,y)}{\partial n_y} = (\mathrm{i}\kappa|x-y|-1)\,\frac{(x-y)\cdot n_y}{|x-y|^3}\,\frac{\mathrm{e}^{\mathrm{i}\kappa|x-y|}}{4\pi}\,. \tag{A.3}$$

The shape functions $\varphi_\nu(x)$ and $\varphi_\mu(y)$ on elements ν and μ are polynomial in x and y, respectively. For elements at some distance, the integral (A.1) can be approximated by standard Gauss quadrature, for identical or adjacent elements the singular integrals have to be treated with special care. The integration schemes described below follow the transformations proposed by Sauter (1992).

A.1 Identical panels

For the case of identical panels $\nu = \mu$, only the fundamental solution (A.2) must be considered as integration kernel, since the term $(x-y)\cdot n_y$ in (A.3) vanishes identically. The parameterization of the triangle is chosen as shown in Fig. A.1.

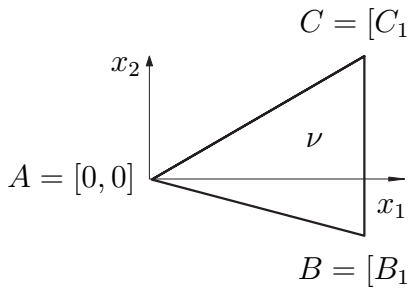

$$\begin{aligned} 0 \le & x_1 \le B_1 \\ m_1 x_1 \le & x_2 \le m_2 x_1 \\ 0 \le & y_1 \le B_1 \\ m_1 y_1 \le & y_2 \le m_2 y_1 \end{aligned} \qquad m_1 = \frac{B_2}{B_1} \qquad m_2 = \frac{C_2}{B_1}$$

Figure A.1: Parameterization of triangle.

Applying the transformation

$$u_1 = x_1 - y_1\,, \qquad u_2 = x_2 - y_2\,, \tag{A.4}$$

defines the integration kernel

$$H(u, y) = \varphi_\nu(u - y)\varphi_\mu(y)\frac{\mathrm{e}^{\mathrm{i}\kappa|u|}}{4\pi|u|}\,. \tag{A.5}$$

The integration domain is split into six subdomains and a second transformation reverts the outer integration to the original triangle ν. One obtains

$$\begin{aligned} \int_\nu \Bigg\{ & \int_0^{B_1-\hat{u}_1} \int_{m_1\hat{y}_1}^{m_2\hat{y}_1} \left(H(\hat{u}, \hat{y}) + H(-\hat{u}, \hat{y} + \hat{u})\right) \mathrm{d}\hat{y}_2\, \mathrm{d}\hat{y}_1 \\ & + \int_{\frac{m_1\hat{u}_1 - \hat{u}_2}{m1 - m2}}^{\hat{u}_1} \int_{m_1(\hat{y}_1 - \hat{u}_1) + \hat{u}_2}^{m_2\hat{y}_1} \left(H(B - \hat{u}, \hat{y}) + H(\hat{u} - B, \hat{y} + B - \hat{u})\right) \mathrm{d}\hat{y}_2\, \mathrm{d}\hat{y}_1 \\ & + \int_{\frac{m_2\hat{u}_1 - \hat{u}_2}{m_2 - m_1}}^{\hat{u}_1} \int_{m_1\hat{y}_1}^{m_2(\hat{y}_1 - \hat{u}_1) + \hat{u}_2} \left(H(C - \hat{u}, \hat{y}) + H(\hat{u} - C, \hat{y} + C - \hat{u})\right) \mathrm{d}\hat{y}_2\, \mathrm{d}\hat{y}_1 \Bigg\} \mathrm{d}\hat{u}\,, \end{aligned} \tag{A.6}$$

where the integration kernels are polynomial in $\hat{u}$. Thus, the inner integrations can be performed analytically, leaving the integral

$$\int_\nu \left\{H_A(\hat{u}) + H_B(\hat{u}) + H_C(\hat{u})\right\} \mathrm{d}\hat{u} \tag{A.7}$$

for numerical quadrature. The kernels in (A.7) possess weak singularities in the respective corners of the panel. This singularity is removed by standard Duffy coordinates. For example, the transformation $\hat{u} = \chi_B(\breve{u})$ maps the element ν onto the reference triangle $\nu_0 := \Delta\left[\begin{pmatrix}0\\0\end{pmatrix}, \begin{pmatrix}1\\0\end{pmatrix}, \begin{pmatrix}1\\1\end{pmatrix}\right]$ with $\chi_B \begin{pmatrix}0\\0\end{pmatrix} = B$ and one can use the transformation $\breve{u}_1 = \xi$, $\breve{u}_2 = \xi\eta$ to yield the regular integral

$$2\Delta_\nu \int_{\xi=0}^1 \int_{\eta=0}^1 H_B(\chi_B \begin{pmatrix}\xi\\ \xi\eta\end{pmatrix})\, \xi\, \mathrm{d}\eta\, \mathrm{d}\xi\,, \tag{A.8}$$

that can be evaluated using standard Gauss quadrature rules.

A.2 Panels with common edge

For the case that the two panels ν and μ share a common edge as depicted in Fig. A.2, the transformations

$$\begin{aligned}\chi_\mu(u) &= A_1^\nu + [A_2^\nu - A_1^\nu,\, A_2^\mu - A_2^\nu]\, u\,,\\ \chi_\nu(w) &= A_1^\nu + [A_2^\nu - A_1^\nu,\, A_3^\nu - A_2^\nu]\, w\,,\end{aligned} \tag{A.9}$$

map the elements ν and μ to the reference triangle. The integral (A.1) becomes

$$\begin{aligned}&\underbrace{4\Delta_\nu\Delta_\mu}_{\Delta_{\nu\mu}} \int_0^1 \int_0^{u_1} \int_0^1 \int_0^{w_1} \underbrace{\varphi_\nu(\chi_\nu(u))\varphi_\mu(\chi_\mu(w))}_{q(u,w)}\, k(\chi_\nu(w) - \chi_\mu(u))\,\mathrm{d}w\,\mathrm{d}u\\ &= \Delta_{\nu\mu} \int_0^1 \int_0^{u_1} \int_0^{u_1} \int_0^{w_1} q(u,w)\, k(\chi_\nu(w) - \chi_\mu(u))\,\mathrm{d}w\,\mathrm{d}u\\ &\qquad + \Delta_{\nu\mu} \int_0^1 \int_0^{w_1} \int_0^{w_1} \int_0^{u_1} q(u,w)\, k(\chi_\nu(w) - \chi_\mu(u))\,\mathrm{d}u\,\mathrm{d}w\,,\end{aligned} \tag{A.10}$$

where the two terms of the sum are of the same type and can be treated equivalently.

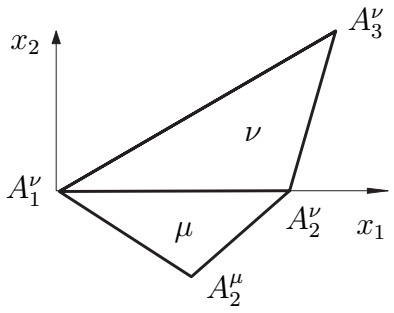

Figure A.2: Panels with common edge.

Applying the transformation $\tilde{w}_1 = u_1 - w_1$ defines the kernel

$$\tilde{k}(u_2, \tilde{w}_1, w_2) := k\left(-A_2^\nu \tilde{w}_1 + [A_2^\nu - A_2^\mu]\, u_2 + [A_3^\nu - A_2^\nu]\, w_2\right)\,. \tag{A.11}$$

Rewriting the first term of (A.10) and splitting the integration domain, one obtains

the integral

$$\begin{aligned}
&\Delta_{\nu\mu}\int_0^1\int_0^{u_2}\int_0^{u_2-\tilde{w}_1}\int_{u_2}^1 q(u,u_1-\tilde{w}_1,w_2)\tilde{k}(u_2,\tilde{w}_1,w_2)\,\mathrm{d}u_1\,\mathrm{d}w_2\,\mathrm{d}\tilde{w}_1\,\mathrm{d}u_2\\
&+\Delta_{\nu\mu}\int_0^1\int_0^{u_2}\int_{u_2-\tilde{w}_1}^{1-\tilde{w}_1}\int_{\tilde{w}_1+w_2}^1 q(u,u_1-\tilde{w}_1,w_2)\tilde{k}(u_2,\tilde{w}_1,w_2)\,\mathrm{d}u_1\,\mathrm{d}w_2\,\mathrm{d}\tilde{w}_1\,\mathrm{d}u_2\\
&+\Delta_{\nu\mu}\int_0^1\int_{u_2}^1\int_0^{1-\tilde{w}_1}\int_{\tilde{w}_1+w_2}^1 q(u,u_1-\tilde{w}_1,w_2)\tilde{k}(u_2,\tilde{w}_1,w_2)\,\mathrm{d}u_1\,\mathrm{d}w_2\,\mathrm{d}\tilde{w}_1\,\mathrm{d}u_2\,.
\end{aligned} \tag{A.12}$$

Here again, the inner integration is polynomial in u_1 and thus can be evaluated analytically, yielding the kernels $\tilde{K}_1(u_2,\tilde{w}_1,w_2)$ and $\tilde{K}_2(u_2,\tilde{w}_1,w_2)$. Before applying numerical quadrature to the outer integrals, the second and third term are combined using appropriate transformations. One obtains the integral

$$\begin{aligned}
&\Delta_{\nu\mu}\int_0^1\int_0^{\hat{u}_2}\int_0^{\hat{w}_1}\tilde{K}_1(\hat{u}_2,\hat{w}_1-\hat{w}_2,\hat{w}_2)\,\mathrm{d}\hat{w}_2\,\mathrm{d}\hat{w}_1\,\mathrm{d}\hat{u}_2\\
&\qquad+\Delta_{\nu\mu}\int_0^1\int_0^{\hat{u}_2}\int_0^{\hat{u}_2}\tilde{K}_2(\hat{u}_2-\hat{w}_2,\hat{u}_2-\hat{w}_1,\hat{w}_1)\,\mathrm{d}\hat{w}_1\,\mathrm{d}\hat{w}_2\,\mathrm{d}\hat{u}_2\,,
\end{aligned} \tag{A.13}$$

on which three-dimensional Duffy coordinates

$$\hat{u}_2=\xi\,,\qquad \hat{w}_1=\xi\eta\,,\qquad \hat{w}_2=\xi\eta\theta\,, \tag{A.14}$$

for the first term and

$$\hat{u}_2=\xi\,,\qquad \hat{w}_1=\xi\eta\,,\qquad \hat{w}_2=\xi\theta\,, \tag{A.15}$$

for the second term yield regular integrals on the unit-cube that can be approximated by tensorial Gauss quadrature.

A.3 Panels with common vertex

The first steps for the case that the two elements ν and μ share a common vertex as depicted in Fig. A.3 are equivalent as for the case with a common edge. The transformations

$$\begin{aligned}
\chi_\mu(u)&=A_1^\nu+[A_3^\mu-A_1^\nu,\,A_2^\mu-A_3^\mu]\,u\,,\\
\chi_\nu(w)&=A_1^\nu+[A_2^\nu-A_1^\nu,\,A_3^\nu-A_2^\nu]\,w\,,
\end{aligned} \tag{A.16}$$

map the elements ν and μ to the reference triangle and the integral (A.1) becomes

$$\begin{aligned}
&\underbrace{4\Delta_\nu\Delta_\mu}_{\Delta_{\nu\mu}} \int_0^1 \int_0^{u_1} \int_0^1 \int_0^{w_1} \underbrace{\varphi_\nu(\chi_\nu(u))\varphi_\mu(\chi_\mu(w))}_{q(u,w)}\, k(\chi_\nu(w) - \chi_\mu(u))\,\mathrm{d}w\,\mathrm{d}u \\
&= \Delta_{\nu\mu} \int_0^1 \int_0^{u_1} \int_0^{u_1} \int_0^{w_1} q(u,w)\, k(\chi_\nu(w) - \chi_\mu(u))\,\mathrm{d}w\,\mathrm{d}u \\
&\qquad + \Delta_{\nu\mu} \int_0^1 \int_0^{w_1} \int_0^{w_1} \int_0^{u_1} q(u,w)\, k(\chi_\nu(w) - \chi_\mu(u))\,\mathrm{d}u\,\mathrm{d}w\,, \quad \text{(A.17)}
\end{aligned}$$

where the two terms are of the same type and can be treated equivalently.

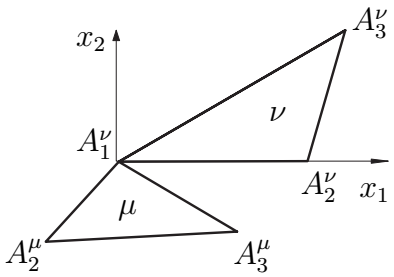

Figure A.3: Panels with common vertex.

For the first term in (A.17), Duffy coordinates

$$w_1 = \xi\,, \qquad w_2 = \xi\phi_1\,, \qquad u_1 = \xi\phi_2\,, \qquad u_2 = \xi\phi_2\phi_3\,, \tag{A.18}$$

remove the singularity and yield the integral

$$\Delta_{\nu\mu} \int_0^1 \int_0^1 \int_0^1 \int_0^1 q(\xi,\phi)\,\xi^3\, k(\xi,\phi)\,\mathrm{d}\xi\,\mathrm{d}\phi_3\,\mathrm{d}\phi_2\,\mathrm{d}\phi_1\,, \tag{A.19}$$

with the kernel

$$k(\xi,\phi) = k\left(\xi\left\{A_2^\nu - A_3^\mu\phi_2 + \left[A_3^\nu - A_2^\nu\right]\phi_1 - \left[A_2^\nu - A_3^\mu\right]\phi_2\phi_3\right\}\right)\,. \tag{A.20}$$

The most inner integral is not polynomial for this case, however for the kernels (A.2) and (A.3) of the Helmholtz equation, it can be evaluated analytically.

Appendix B

Regularization of the hyper-singular operator

The regularization of the hyper-singular operator according to (2.18) goes back to Maue (1949) and is proposed for the Helmholtz equation by Nédélec (1982). However, in this simple form, it is only valid for closed boundaries or a prescribed zero pressure jump on the edges of the boundary. This requirement is not fulfilled for the multipole BEM where the hyper-singular operator is regularized in the near-field only. Instead of integrals over the entire boundary Γ, one has to evaluate integrals over the elements ν in the current Cluster (Cl) and the elements μ in its near-field (NF) of the type

$$\mathbf{D}_{\mathrm{Cl}} = \sum_{\nu\in\mathrm{Cl}} \int_\nu \sum_{\mu\in\mathrm{NF}} \int_\mu \varphi_\tau^p|_\nu(x)\; \varphi_\sigma^p|_\mu(y)\; \frac{\partial^2 P^*(x,y)}{\partial n_x \partial n_y}\; \mathrm{d}s_y\, \mathrm{d}s_x\,, \tag{B.1}$$

where τ and σ correspond to node numbers and specify the position of the computed matrix entry. Applying basic relations of vector algebra, one obtains

$$\begin{aligned}\mathbf{D}_{\mathrm{Cl}} = \mathbf{D}_1 - \mathbf{D}_2 = &\sum_{\nu\in\mathrm{Cl}} \int_\nu \sum_{\mu\in\mathrm{NF}} \int_\mu \kappa^2 n_x \cdot n_y\; \varphi_\tau^p|_\nu(x)\; \varphi_\sigma^p|_\mu(y)\; P^*(x,y)\; \mathrm{d}s_y\, \mathrm{d}s_x \\ &- \sum_{\nu\in\mathrm{Cl}} \int_\nu \varphi_\tau^p|_\nu(x) \sum_{\mu\in\mathrm{NF}} \int_\mu \varphi_\sigma^p|_\mu(y)\, n_y \cdot [\nabla_y \times (n_x \times \nabla_x P^*(x,y))]\; \mathrm{d}s_y\, \mathrm{d}s_x\,.\end{aligned} \tag{B.2}$$

Stokes' theorem is applied on the second term twice to yield

$$\begin{aligned}\mathbf{D}_2 = &\sum_{\partial\mu\in\partial\mathrm{NF}} \int_{\partial\mu} \varphi_\sigma^p|_\mu(y) \sum_{\partial\nu\in\partial\mathrm{Cl}} \int_{\partial\nu} \varphi_\tau^p|_\nu(x) P^*(x,y)\,\mathrm{d}x\,\mathrm{d}y \\ &- \sum_{\partial\mu\in\partial\mathrm{NF}} \int_{\partial\mu} \varphi_\sigma^p|_\mu(y) \sum_{\nu\in\mathrm{Cl}} \int_{\nu} \left(n_x \times \nabla_x \varphi_\tau^p|_\nu(x)\right) P^*(x,y)\,\mathrm{d}s_x\,\mathrm{d}y \\ &- \sum_{\mu\in\mathrm{NF}} \int_{\mu} \left(n_y \times \nabla_y \varphi_\sigma^p|_\mu(y)\right) \sum_{\partial\nu\in\partial\mathrm{Cl}} \int_{\partial\nu} \varphi_\tau^p|_\nu(x) P^*(x,y)\,\mathrm{d}x\,\mathrm{d}s_y \\ &+ \sum_{\mu\in\mathrm{NF}} \int_{\mu} \left(n_y \times \nabla_y \varphi_\sigma^p|_\mu(y)\right) \sum_{\nu\in\mathrm{Cl}} \int_{\nu} \left(n_x \times \nabla_x \varphi_\tau^p|_\nu(x)\right) P^*(x,y)\,\mathrm{d}s_x\,\mathrm{d}s_y\ ,\end{aligned} \tag{B.3}$$

where $\partial\mu \in \partial\mathrm{NF}$ denotes the element edges that build the boundary of the nearfield, whereas $\partial\nu \in \partial\mathrm{Cl}$ denotes the element edges on the boundary of the cluster. The numerical cost for the additional evaluation of the edge integrals is small compared to the cost for the standard boundary integrals. Special care must be paid to the third term in (B.3) since it becomes weakly singular for the near-field elements that touch the cluster edge: a simple increase of Gauss points for these few elements has proven to be sufficiently accurate and efficient.

Appendix C

Plate backed by acoustic cavity

A Kirchhoff plate backed by an acoustic cavity is used as model problem to study the FEM-BEM mortar coupling algorithm in Chapter 5. Pretlove (1966) develops an analytic series solution for this problem which is shortly reviewed here. The harmonic time dependency $\mathrm{e}^{-\mathrm{i}\omega t}$ is omitted from the plate displacement w and the acoustic pressure p throughout the presentation.

The cavity has the dimension $a \times b \times c$ as depicted in Fig. C.1 and the walls are rigid except for the surface $z = c$ which is coupled to a thin Kirchhoff plate. The continuity condition is written as

$$\left.\frac{\partial p}{\partial z}\right|_{z=c} = \rho^{\mathrm{f}}\omega^2 w\,. \tag{C.1}$$

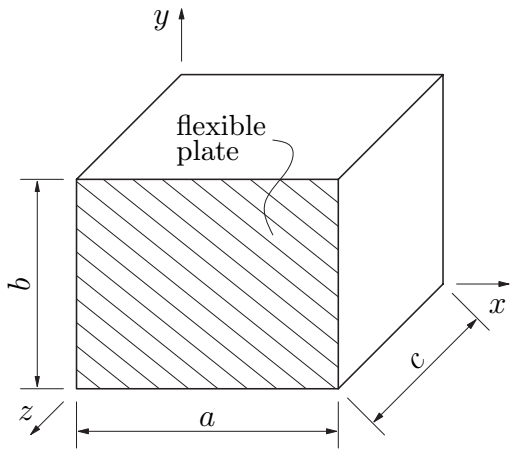

Figure C.1: Rectangular acoustic cavity with one flexible wall.

The plate is simply supported on its edges which yields the expansion

$$w = \sum_{r=1}^{\infty}\sum_{s=1}^{\infty} w_{rs} \sin\left(\frac{r\pi x}{a}\right) \sin\left(\frac{s\pi y}{b}\right) , \tag{C.2}$$

and the equation of motion

$$\left(K_{rs} - \omega^2 M_{rs}\right) w_{rs} = F_{rs} , \tag{C.3}$$

where K_{rs} and M_{rs} are the known stiffness and mass coefficients of the plate, respectively. The forcing coefficients $F_{rs} = F_{rs}^{\text{extern}} + F_{rs}^{\text{f}}$ consist of external forcing and the unknown back pressure of the acoustic field.

The pressure field in the acoustic cavity is expanded as

$$p = \sum_{n=0}^{\infty}\sum_{m=0}^{\infty} \cos\left(\frac{n\pi x}{a}\right) \cos\left(\frac{m\pi y}{b}\right) L_{nm} \cosh\left(\mu_{nm} z\right) , \tag{C.4}$$

with the coefficients L_{nm} and

$$\mu_{nm}^2 = \pi^2 \left[\left(\frac{n}{a}\right)^2 + \left(\frac{m}{b}\right)^2\right] - \left(\frac{\omega}{c^{\text{f}}}\right)^2 . \tag{C.5}$$

To fulfill the continuity condition (C.1), the plate displacement must be represented in the form

$$w = \frac{1}{\rho^{\text{f}}\omega^2} \sum_{n=0}^{\infty}\sum_{m=0}^{\infty} \cos\left(\frac{n\pi x}{a}\right) \cos\left(\frac{m\pi y}{b}\right) L_{nm}\, \mu_{nm} \sinh\left(\mu_{nm} c\right) . \tag{C.6}$$

A double cosine Fourier analysis is applied to the $(r's')$ mode of plate vibration and one obtains the coefficients $\alpha_{nm}^{(r's')}$ so that

$$w_{(r's')} \sin\left(\frac{r\pi x}{a}\right) \sin\left(\frac{s\pi y}{b}\right) = w_{(r's')} \sum_{n=0}^{\infty}\sum_{m=0}^{\infty} \alpha_{nm}^{(r's')} \cos\left(\frac{n\pi x}{a}\right) \cos\left(\frac{m\pi y}{b}\right) . \tag{C.7}$$

Comparing the coefficients in (C.6) and (C.7) allows to compute the acoustic back pressure $p_{\text{back}}^{(r's')}$ from the $(r's')$ plate mode as

$$p_{\text{back}}^{(r's')} = \rho^{\text{f}}\omega^2 w_{(r's')} \sum_{n=0}^{\infty}\sum_{m=0}^{\infty} \frac{\alpha_{nm}^{(r's')}}{\mu_{nm}} \coth(\mu_{nm} c) \cos\left(\frac{n\pi x}{a}\right) \cos\left(\frac{m\pi y}{b}\right) . \tag{C.8}$$

The coefficients $F_{rs}^{\text{f}(r's')}$ are obtained by integrating over the coupling interface

$$F_{rs}^{\text{f}(r's')} = \int_{x=0}^{a}\int_{y=0}^{b} p_{\text{back}}^{(r's')} \sin\left(\frac{r\pi x}{a}\right) \sin\left(\frac{s\pi y}{b}\right) \mathrm{d}y\, \mathrm{d}x . \tag{C.9}$$

Substituting (C.7) and (C.8) into (C.9), one obtains the acoustic stiffness coefficients for the plate

$$K_{rs}^{(r's')} = \rho^{\mathrm{f}}\omega^2 \sum_{n=0}^{\infty}\sum_{m=0}^{\infty} \frac{\alpha_{nm}^{(r's')}\alpha_{nm}^{(rs)}}{\mu_{nm}} \coth(\mu_{nm}c) \int_{x=0}^{a} \cos^2\left(\frac{n\pi x}{a}\right) \mathrm{d}x \int_{y=0}^{b} \cos^2\left(\frac{m\pi y}{b}\right) \mathrm{d}y\,, \quad \text{(C.10)}$$

and the equation of motion (C.3) is written as

$$\left(K_{rs} - \omega^2 M_{rs}\right) w_{rs} - \sum_{(r's')} K_{rs}^{(r's')} w_{(r's')} = F_{rs}^{\mathrm{extern}}\,. \quad \text{(C.11)}$$

The coefficients for the coupled plate vibration can now simply be computed by solving (C.11).

Bibliography

M. Abramowitz and I.A. Stegun, editors. *Handbook of Mathematical Functions*. Dover Publications, New York, 1974.

R. Barrett, M. Berry, T. F. Chan, J. Demmel, J. Donato, J. Dongarra, V. Eijkhout, R. Pozo, C. Romine, and H. Van der Vorst. *Templates for the Solution of Linear Systems: Building Blocks for Iterative Methods*. SIAM, Philadelphia, PA, 1994.

M. Bebendorf and S. Rjasanow. Adaptive low-rank approximation of collocation matrices. *Computing*, 70(1):1–24, 2003.

F. Ben Belgacem. The mortar finite element method with Lagrange multipliers. *Numerische Mathematik*, 84:173–197, 1999.

C. Bernardi, Y. Maday, and A.T. Patera. A new nonconforming approach to domain decomposition: the mortar element method. In H. Brezis et al., editor, *Nonlinear Partial Differential Equations and their Applications*, pages 13–51. Pitman, 1994.

J. Board and K. Schulten. The fast multipole algorithm. *IEEE Computing in Science & Engineering*, 2(1):76–79, 2000.

M. Bonnet, G. Maier, and C. Polizzotto. Symmetric Galerkin boundary element methods. *Applied Mechanics Reviews*, 51(11):669–704, 1998.

A. Bouras and V. Frayssé. A relaxation strategy for inexact matrix-vector products for Krylov methods. CERFACS Technical Report TR/PA/00/15, 2000.

D. Braess and W. Dahmen. Stability estimates of the mortar finite element method for 3-dimensional problems. *East-West Journal of Numerical Mathematics*, 6(4): 249–263, 1998.

H. Brakhage and P. Werner. Über das Dirichlet'sche Außenraumproblem für die Helmholtz'sche Schwingungsgleichung. *Archiv der Mathematik*, 16:325–329, 1965.

J.H. Bramble, J.E. Pasciak, and A.T. Vassilev. Analysis of the inexact Uzawa algorithm for saddle point problems. *SIAM Journal of Numerical Analysis*, 34(3): 1072–1092, 1997.

A. Brandt and I. Livshits. Wave-ray multigrid method for standing wave equations. *Electronic Transactions on Numerical Analysis*, 6:162–181, 1997.

F. Brezzi and M. Fortin. *Mixed and Hybrid Finite Element Methods*. Springer-Verlag, New York, 1991.

W.L. Briggs, V.E. Henson, and S.F. McCormick. *A Multigrid Tutorial*. SIAM, Philadelphia, PA, second edition, 2000.

A.J. Burton and G.F. Miller. The application of integral equation methods to the numerical solution of some exterior boundary-value problems. *Proceedings of the Royal Society of London, Series A*, 323:201–210, 1971.

K. Chen. An analysis of sparse approximate inverse preconditioners for boundary integral equations. *SIAM Journal on Matrix Analysis and Applications*, 22(4): 1058–1078, 2001.

K. Chen and P. Harris. Efficient preconditioners for iterative solution of the boundary element equations for the three-dimensional Helmholtz equation. *Applied Numerical Mathematics*, 36:475–489, 2001.

L.H. Chen and D.G. Schweikert. Sound radiation from an arbitrary body. *Journal of the Acoustical Society of America*, 35:1626–1632, 1963.

Z.S. Chen, G. Hofstetter, and H.A. Mang. A symmetric Galerkin formulation of the boundary element method for acoustic radiation and scattering. *Journal of Computational Acoustics*, 5(2):219–241, 1997.

Z.S. Chen, G. Hofstetter, and H.A. Mang. A Galerkin-type BE–FE formulation for elasto–acoustic coupling. *Computer Methods in Applied Mechanics and Engineering*, 152:147–155, 1998.

W.C. Chew, H.Y. Chao, T.J. Cui, C. C. Lu, S. Ohnuki, Y.C. Pan, J.M. Song, S. Velamparambil, and J.S. Zhao. Fast integral equation solvers in computational electromagnetics of complex structures. *Engineering Analysis with Boundary Elements*, 27(8):803–823, 2003.

R. Coifman, V. Rokhlin, and S. Wandzura. The fast multipole method for the wave equation: A pedestrian prescription. *IEEE Antennas and Propagation Magazine*, 35:7–12, 1993.

L. Cremer and M. Möser. *Technische Akustik*. Springer-Verlag, Berlin, fifth edition, 2003.

O. Czygan and O. von Estorff. Fluid-structure interaction by coupling BEM and nonlinear FEM. *Engineering Analysis with Boundary Elements*, 26(9):773–779, 2002.

E. Darve. The fast multipole method I: error analysis and asymptotic complexity. *SIAM Journal of Numerical Analysis*, 38(1):98–128, 2000.

H.C. Elman, O.G. Ernst, and D.P. O'Leary. A multigrid method enhanced by Krylov subspace iteration for discrete Helmholtz equations. *SIAM Journal of Scientific Computing*, 23(4):1291–1315, 2001.

H.C. Elman and G.H. Golub. Inexact and preconditioned Uzawa algorithms for saddle point problems. *SIAM Journal of Numerical Analysis*, 31(6):1645–1661, 1994.

M.A. Epton and B. Dembart. Multipole translation theory for the three-dimensional Laplace and Helmholtz equations. *SIAM Journal of Scientific Computing*, 16:865–897, 1995.

G.C. Everstine and F.M. Henderson. Coupled finite element/boundary element approach for fluid structure interaction. *Journal of the Acoustical Society of America*, 87(5):1938–1947, 1990.

F. Fahy. *Foundations of Engineering Acoustics*. Academic Press, London, UK, 2001.

O. Fein and L. Gaul. Reduction of sound emission from submerged structures using piezoelectric sensors and actuators. In *Proceedings of the 9th International Congress on Sound and Vibration*, pages 316–323, Orlando, Fl, 2002.

M. Fischer, U. Gauger, and L. Gaul. A multipole Galerkin boundary element method for acoustics. *Engineering Analysis with Boundary Elements*, 28(2):155–162, 2004.

U. Gauger. Die Anwendung der Multipolmethode auf Randintegralgleichungen in der Akustik. Diplomarbeit, Institut A für Mechanik, Universität Stuttgart, 2002.

L. Gaul, M. Kögl, and M. Wagner. *Boundary Element Methods for Engineers and Scientists*. Springer-Verlag, Berlin, 2003.

L. Gaul and W. Wenzel. A coupled symmetric BE-FE method for acoustic fluid-structure interaction. *Engineering Analysis with Boundary Elements*, 26(7):629–636, 2002.

K. Giebermann. Schnelle Summationsverfahren zur numerischen Lösung von Integralgleichungen für Streuprobleme im R^3. PhD thesis, Universität Karlsruhe, 1997.

L. Greengard and V. Rokhlin. A fast algorithm for particle simulations. *Journal of Computational Physics*, 73:325–348, 1987.

M.F. Gyure and M.A. Stalzer. A prescription for the multilevel Helmholtz FMM. *IEEE Computational Science & Engineering*, 5(3):39–47, 1998.

W. Hackbusch. *Multi-Grid Methods and Applications*. Springer-Verlag, Berlin, 1985.

W. Hackbusch. A sparse matrix arithmetic based on $\mathcal{H}$-matrices. I. Introduction to $\mathcal{H}$-matrices. *Computing*, 62(2):89–108, 1999.

F. Ihlenburg. *Finite Element Analysis of Acoustic Scattering*. Springer-Verlag, New York, 1998.

M.C. Junger. Acoustic fluid–elastic structure interactions: basic concepts. *Computers & Structures*, 65(3):287–293, 1997.

S. Koc, J.M. Song, and W.C. Chew. Error analysis for the numerical evaluation of the diagonal forms of the scalar spherical additon theorem. *SIAM Journal of Numerical Anlysis*, 36(3):906–921, 1999.

R. Kress. Minimizing the condition number of boundary integral operators in acoustic and electromagnetic scattering. *Quarterly Journal of Mechanics and Applied Mathematics*, 38:323–341, 1985.

A. Kropp and D. Heiserer. Efficient broadband vibro-acoustic analysis of passenger car bodies using an FE-based component mode sythesis approach. *Journal of Computational Acoustics*, 11(2):139–157, 2003.

S. Langer and H. Antes. Analyses of sound transmission through windows by coupled finite and boundary element methods. *Acta Acustica*, 89:78–85, 2003.

U. Langer, D. Pusch, and S. Reitzinger. Efficient preconditioners for boundary element matrices based on grey-box algebraic multigrid methods. *International Journal for Numerical Methods in Engineering*, 58(13):1937–1953, 2003.

R.H. Lyon and R.D. DeJong. *Theory and Application of Statistical Energy Analysis*. Butterworth-Heinemann, Boston, MA, 1995.

S. Marburg and S. Schneider. Influence of element types on numeric error for acoustic boundary elements. *Journal of Computational Acoustics*, 11(3):363–386, 2003a.

S. Marburg and S. Schneider. Performance of iterative solvers for acoustic problems. Part I. Solvers and effect of diagonal preconditioning. *Engineering Analysis with Boundary Elements*, 27(7):727–750, 2003b.

A.W. Maue. Zur Formulierung eines allgemeinen Beugungsproblems durch eine Integralgleichung. *Zeitschrift für Physik*, 126:601–618, 1949.

M. Moosrainer. Fluid-Struktur-Kopplung: Vibroakustische Lösungsmethoden und Anwendungen. PhD thesis, Universität der Bundeswehr München, 2000.

J.-C. Nédélec. Integral equations with nonintegrable kernels. *Integral Equations Operator Theory*, 5(4):562–572, 1982.

J.-C. Nédélec. *Acoustic and Electromagnetic Equations: Integral Representations for Harmonic Problems.* Springer-Verlag, New York, 2001.

N. Nishimura. Fast multipole accelerated boundary integral equation methods. *Applied Mechanics Reviews*, 55(4):299–324, 2002.

M. Ochmann, A. Homm, S. Makarov, and S. Semenov. An iterative GMRES-based boundary element solver for acoustic scattering. *Engineering Analysis with Boundary Elements*, 27(7):717–725, 2003.

M. Ochmann and F. Wellner. Berechnung der Schallabstrahlung dreidimensionaler schwingender Körper mit Hilfe eines Randelemente-Mehrgitterverfahrens. *Acustica*, 73:177–190, 1991.

G. Of, O. Steinbach, and W.L. Wendland. The fast multipole method for the symmetric boundary integral equation. In *Proceedings of the IABEM 2002 Symposium*, Austin, TX, 2002.

S. Ohnuki and W.C. Chew. Truncation error analysis of multipole expansion. *SIAM Journal of Scientific Computing*, 25(4):1293–1306, 2003.

H. Perfahl. Approximate-Inverse-Vorkonditionierer für die Multipol-BEM in der Akustik. Studienarbeit, Institut A für Mechanik, Universität Stuttgart, 2003.

H. Perfahl. Entwicklung eines Mehrgitterlösers für die Multipol-Randelementmethode in der Akustik. Diplomarbeit, Institut A für Mechanik, Universität Stuttgart, 2004.

A.J. Pretlove. Forced vibrations of a rectangular panel backed by a closed rectangular cavity. *Journal of Sound and Vibration*, 3(3):252–261, 1966.

J. Rahola. Diagonal forms of the translation operators in the fast multipole algorithm for scattering problems. *BIT*, 36:333–358, 1996.

V. Rokhlin. Rapid solution of integral equations of scattering theory in two dimensions. *Journal of Computational Physics*, 86:414–439, 1990.

V. Rokhlin. Diagonal forms of translation operators for the Helmholtz equation in three dimensions. *Applied and Computational Harmonic Analysis*, 1:82–93, 1993.

Y. Saad. *Iterative Methods for Sparse Linear Systems*. SIAM, Philadelphia, PA, second edition, 2003.

S.A. Sauter. Über die effiziente Verwendung des Galerkinverfahrens zur Lösung Fredholmscher Integralgleichungen. PhD thesis, Christian-Albrechts-Universität zu Kiel, 1992.

S.A. Sauter and A. Krapp. On the effect of numerical integration in the Galerkin boundary element method. *Numerische Mathematik*, 74:337–359, 1996.

H.A. Schenck. Improved integral formulation for acoustic radiation problems. *Journal of the Acoustical Society of America*, 44:41–58, 1968.

R. Schneider. *Multiskalen- und Wavelet-Matrixkompression: Analysisbasierte Methoden zur Lösung großer vollbesetzter Gleichungssysteme*. B.G. Teubner, Stuttgart, 1998.

S. Schneider. Application of fast methods for acoustic scattering and radiation problems. *Journal of Computational Acoustics*, 11(3):387–401, 2003a.

S. Schneider. Efficient usage of the boundary-element-method for solving the time harmonic Helmholtz equation in three dimensions. PhD thesis, Technische Universität Dresden, 2003b.

S. Schneider and S. Marburg. Performance of iterative solvers for acoustic problems. Part II. Acceleration by ILU-type preconditioner. *Engineering Analysis with Boundary Elements*, 27(7):751–757, 2003.

K.B. Sidhu. Comparison of Experiments and FE Analysis of Acoustic-Structure Interaction. Master thesis, Institut A für Mechanik, Universität Stuttgart, 2002.

V. Simoncini and D.B. Szyld. Theory of inexact Krylov subspace methods and applications to scientific computing. *SIAM Journal of Scientific Computing*, 25 (2):454–477, 2003.

S. Sirtori. General stress anlaysis method by means of integral equations and boundary elements. *Meccanica*, 14:210–218, 1979.

O. Steinbach. *Numerische Näherungsverfahren für elliptische Randwertprobleme*. B.G. Teubner, Stuttgart, 2003a.

O. Steinbach. *Stability estimates for hybrid coupled domain decomposition methods*. Springer-Verlag, Berlin, 2003b.

G. Tröndle. Effiziente Schallberechnung mit einem adaptiven Mehrgitterverfahren für die 3-D Randelementmethode. PhD thesis, Technische Universität Carolo-Wilhelmina zu Braunschweig, 1995.

J. van den Eshof and G.L.G. Sleijpen. Inexact Krylov subspace methods for linear systems. *SIAM Journal on Matrix Analysis and Applications*, 26(1):125–153, 2004.

H.A. van der Vorst. *Iterative Krylov Methods for Large Linear Systems*. Cambridge University Press, Cambridge, UK, 2003.

O. von Estorff, editor. *Boundary Elements in Acoustics: Advances and Applications*. WIT Press, Southampton, UK, 2000.

O. von Estorff and O. Zaleski. Efficient acoustic calculations by the BEM and frequency interpolated transfer functions. *Engineering Analysis with Boundary Elements*, 27(7):683–694, 2003.

M. Wagner. Die hybride Randelementmethode in der Akustik und zur Struktur-Fluid-Interaktion. PhD thesis, Institut A für Mechanik, Universität Stuttgart, 2000.

B.I. Wohlmuth. A mortar finite element method using dual spaces for the Lagrange multiplier. *SIAM Journal of Numerical Analysis*, 38:989–1012, 2000.

T.W. Wu, editor. *Boundary Element Acoustics: Fundamentals and Computer Codes*. WIT Press, Southampton, UK, 2000.

O.C. Zienkiewicz and R.L. Taylor. *The Finite Element Method*. Butterworth-Heinemann, Oxford, UK, fifth edition, 2000.

Bisher erschienene Berichte aus dem Institut A für Mechanik

1/1994 **Martin Schanz:** Eine Randelementformulierung im Zeitbereich mit verallgemeinerten viskoelastischen Stoffgesetzen.

2/1994 Bericht über die Tätigkeit des Instituts. - Wintersemester 1993/94 und Sommersemester 1994.

1/1995 **Peter Kohmann:** Ein Beitrag zur Lärmminderung bei flüssigkeitsgefüllten Rohrleitungen auf Schiffen.

2/1995 **Klaus-Peter Kuhn:** Fehlererkennung mittels nichtlinearer Mehrfilterverfahren am Beispiel eines Bioprozesses.

3/1995 **Manfred Estler:** Neue Ansätze zur adaptiven nichtlinearen Regelung von Fed-Batch-Bioprozessen.

4/1995 **Jörg Wagner:** Zur Simulation und Identifikation der Segelflug-Längsbewegung.

5/1995 Bericht über die Tätigkeit des Instituts. - Wintersemester 1994/95 und Sommersemester 1995.

1/1996 **Delf Sachau:** Berücksichtigung von flexiblen Körpern und Fügestellen in Mehrkörpersystemen zur Simulation aktiver Raumfahrtstrukturen.

2/1996 **Jörg Leyser:** Kraftberechnung an der nichtplanaren tragenden Fläche.

3/1996 Bericht über die Tätigkeit des Instituts. - Wintersemester 1995/96 und Sommersemester 1996.

1/1997 **Johann Lenz:** Strukturdynamik unter dem Einfluß von Mikro- und Makroschlupf in Fügestellen.

2/1997 **Udo Rein:** Effiziente objektorientierte Simulation von Mehrkörpersystemen mit dem rekursiven Formalismus.

3/1997 Bericht über die Tätigkeit des Instituts. - Wintersemester 1996/97 und Sommersemester 1997.

1/1998 **Bernhard Daniel Höfig:** Physiologische Modellierung des menschlichen Glukose-Metabolismus für die simulationsgestütze Therapie des insulin-abhängigen Diabetes mellitus.

2/1998 **Bodo Nolte:** Randelementberechnungen und Nahfeldmessungen zur akustischen Fluid-Struktur-Interaktion.

3/1998 **Thomas Spägele:** Modellierung, Simulation und Optimierung menschlicher Bewegungen.

4/1998 Bericht über die Tätigkeit des Instituts. - Wintersemester 1997/98 und Sommersemester 1998.

5/1998 **Ulrich Mangold:** Anwendungsorientierte Genauigkeitsanalysen von satellitengestützten Trägheitsnavigationssystemen.

6/1998 **Michael Hanss:** Identifikation von Fuzzy-Modellen und ihre Anwendung zur Regelung nichtlinearer Prozesse.

7/1998 **Albrecht Irion:** Einsatz von Fuzzy-Methoden in strukturvariablen Reglern.

1/1999 **Peter Waszkewitz:** Detektierung von Beschriftungen auf metallischen Oberflächen mit Hilfe von Texturmethoden und Neuronalen Netzen.

2/1999 **Hans-Thomas Fritzsche:** Entwicklung und Anwendung eines mikroskopischen Modells zur Verkehrssimulation auf mehrspurigen Richtungsfahrbahnen.

3/1999 **Jong-Zen Huang:** Adaptive Verfahren auf der Basis von Fuzzy-Logik zur Regelung und Identifikation bei Bioprozessen.

4/1999 Bericht über die Tätigkeit des Instituts. - Wintersemester 1998/99 und Sommersemester 1999.

1/2000 **Jingsheng Ye:** Modellgestützte adaptive Regelverfahren für Industrieroboter.

2/2000 **Dieter Eppinger:** Ein Beitrag zur akustischen Güteprüfung unter Berücksichtigung der Anforderungen in der Serienfertigung.

3/2000 **Thomas Maier:** Techniken und Werkzeuge für die Gewährleistung funktionaler Sicherheit von Software in technischen Systemen.

4/2000 **Marcus Wagner:** Hybride Randelementmethode in der Akustik und zur Fluid-Struktur-Interaktion.

5/2000 Bericht über die Tätigkeit des Instituts. - Wintersemester 1999/2000 und Sommersemester 2000.

6/2000 **Martin Kögl:** A Boundary Element Method for Dynamic Analysis of Anisotropic, Piezoelectric, and Thermoelastic Solids.

1/2001 **Wolfgang Wenzel:** Hybride Randelementmethode für transiente Probleme in der Akustik.

2/2001 **Friedrich Moser:** Nicht-singuläre räumliche Randelementformulierung der Elastodynamik.

3/2001 Bericht über die Tätigkeit des Instituts. - Wintersemester 2000/2001 und Sommersemester 2001.

2001 **Eike Brechlin:** Methoden und Grenzen der Substrukturkopplung auf der Basis experimenteller Daten. ISBN 3-936231-02-8

1/2002 **Ralf Gutmann:** Auf Statistikdaten basierende Testsequenz-Optimierung zur Minimierung der Prüfkosten für integrierte Schaltkreise.

2/2002 **Zoltán Á. Zomotor:** Online-Identifikation der Fahrdynamik zur Bewertung des Fahrverhaltens von Pkw.

3/2002 **Stefan Hurlebaus:** A Contribution to Structural Health Monitoring Using Elastic Waves.

4/2002 Bericht über die Tätigkeit des Instituts. - Wintersemester 2001/2002 und Sommersemester 2002.

2002 **Werner Moll:** Strukturkopplung mit Modalmodellen aus Messungen. ISBN 3-936231-34-6

2003/1 **Andre Schmidt:** Finite-Elemente-Formulierungen viskoelastischer Werkstoffe mit fraktionalen Zeitableitungen. ISBN 3-89959-071-6

2003/2 **Stefan Oexl:** Untersuchungen zum dynamischen Verhalten normalbelasteter Schraubverbindungen. ISBN 3-89959-072-4

2003/3 Bericht über die Tätigkeit des Instituts. - Wintersemester 2002/2003 und Sommersemester 2003.

2003/4 **Darko Meljnikov:** Entwicklung von Modellen zur Bewertung des Fahrverhaltens von Kraftfahrzeugen.

2004/1 **Jan Wirnitzer:** Schwingungsreduktion flexibler Raumfahrtstrukturen durch semi-aktive Reibverbindungen.

2004/2 **Matthias Fischer:** The Fast Multipole Boundary Element Method and its Application to Structure-Acoustic Field Interaction.